Spring 1-1-2019

The Effect of Ocean Waves on Airborne Lidar Bathymetry

Bryce Howell Garby
University of Colorado at Boulder, bryce.garby@colorado.edu

The Effect of Ocean Waves on Airborne Lidar Bathymetry

by

Bryce Garby

A thesis submitted to the

Faculty of the Graduate School of the

University of Colorado in partial fulfillment

of the requirements for the degree of

M.S. Aerospace Engineering

Ann and H.J. Smead Department of Aerospace Engineering Sciences

2019

This thesis entitled:
The Effect of Ocean Waves on Airborne Lidar Bathymetry
written by Bryce Garby
has been approved for the Ann and H.J. Smead Department of Aerospace Engineering Sciences

Prof. Jeffrey P. Thayer

Prof. R. Steven Nerem

Prof. Nisar Ahmed

Date

The final copy of this thesis has been examined by the signatories, and we find that both the content and the form meet acceptable presentation standards of scholarly work in the above mentioned discipline.

Garby, Bryce (M.S. Aerospace Engineering)

The Effect of Ocean Waves on Airborne Lidar Bathymetry

Thesis directed by Prof. Jeffrey P. Thayer

Airborne lidar bathymetry, or ALB, is an active remote sensing technique capable of filling the need for topographical maps of coastal regions and other regions of shallow water. Modern ALB systems can quickly generate expansive, accurate, and high-resolution bathymetric point clouds. One of the main remaining factors limiting these systems is the effect of waves on the water surface.

This thesis focuses on the development of a comprehensive model to describe interaction between the ocean surface and a bathymetric lidar. The model is able to simulate received lidar signals for varying surface conditions and angles of incidence. From this, uncertainties and errors in the desired lidar measurements of depth, surface height, and horizontal position can be better understood. It is shown that surface waves are a significant source of error for ALB measurements and can be the dominating source of uncertainty in the case of large waves or a large angle of incidence. Furthermore, the ability of an ALB system to extract wave information such as significant wave height is investigated and shown to be possible.

Dedication

To all my friends, family, and colleagues. Your support and encouragement has meant so much to me.

Acknowledgements

Many people have helped and contributed to my journey towards completing this Master's thesis. First and foremost I would like to acknowledge my advisor Dr. Jeffrey Thayer. Over the past year, Dr. Thayer has helped immensely as a mentor by allowing me freedom to pursue my research interests and guidance to ensure my first foray into academia was an interesting and useful contribution. Additionally Dr. Thayer has been a huge help to me throughout my undergraduate career in Aerospace Engineering at CU Boulder. He was the one who first introduced me to the field of lidar and then continued giving me opportunities with lidar as I grew. My other two committee members have also helped by being excellent professors for me in undergrad and by being cooperative and helpful as I went through the process of writing this thesis.

I would also like to recognize all who have worked with me in the Active Remote Sensing Lab here at CU. Particularly, I would like to acknowledge Rory Barton-Grimley. Rory has been a mentor and a great colleague to me for nearly 4 years. Without him as a friend in the lab I would not be where I am today. His help has been instrumental in the development of this thesis. Additionally, Active Remote Sensing Lab members Dawson Beatty and Ben Wise have helped me with this accomplishment.

I would also like to thank my friends and family. I have some of the best friends anyone could ask for and their support has helped me many times outside of the classroom. My parents deserve recognition for their unwavering encouragement and support. None of this would have been possible without their help.

Contents

Chapter

Figures

Figure

Chapter 1

Introduction

Lidar is an active remote-sensing technique that involves range determination by transmission and detection of light. The process of making a measurement with a lidar system includes transmission of a pulse of laser light, scattering of the light off of some object, and then timing the reception of the back-scattered light with a detector. The range to the back-scattering object can then be determined according to the speed of light, c, and the index of refraction in the local media. Besides range, additional information about the scattering object can be obtained by analyzing other traits of the detected light, such as, power, polarization, or signal shape. These capabilities, along with lidar's ability to detect a diverse range of different types of objects, make lidar a powerful remote sensing tool for a variety of different situations.

In recent years, development and research in the field of lidar has been quickly accelerating. This has led to an expansion of lidars use as a sensing tool in many different disciplines. One example is lidars use for remote sensing in the presence of liquid water. Among the different water related science products which can be extracted using lidar are, water column properties like temperature or turbidity, water surface information, and subsurface topography [1]. Currently, most of the interest in lidars use for water sensing lies in subsurface mapping, also known as bathymetry. The motivation for lidar bathymetry is driven by it's ability to fill important gaps in the coastal/shallow water regions of Earth elevation maps. Commercial industries and the scientific community have both expressed a need for bathymetry data in these missing regions. On the commercial side, underwater depth measurements/mapping are necessary to industries such

as mining, oil/gas, fishing, shipping, and construction[2][3][1]. Within the scientific community, high quality subsurface data is useful for studying local ecosystems, erosion effects, and geology. The ability to determine water depth changes in coastal waters, glacial melt pools, and riverine environments, is additionally useful for climate change studies[4][5].

The gaps in these topographic/bathymetric datasets exist due to limitations in the techniques used to measure land and sea-surface topography (radar), and sea-floor topography (sonar). In shallow water regions where these systems struggle, lidar excels due to it's superior resolution and ability to penetrate the water surface[6]. Furthermore, airborne lidar bathymetry (ALB) is a more cost-effective solution for many of these situations[7]. Sonar based bathymetry typically involves transmitting and receiving sound pulses from a ship through water at a high angular resolution. By controlling the direction of the beam and measuring the time taken for the sound pulses to be received, the underwater topography can be determined. This is advantageous in a deep water environment where high power sound pulses can penetrate deeper into water than visible light which experiences significant scattering and attenuation. The limitations of sonar in shallow water are due to a multitude of factors. For one, sonar bathymetry is typically conducted using a multibeam sonar which has poor swath coverage in shallow areas. Generally, the resolution of these instruments is also too low to be able to resolve features in shallow water. Lastly, regions of shallow water are often extremely difficult or dangerous to access with a sonar system. Glacial melt pools are well known for their unpredictable and hazardous nature whereas coastal areas are difficult due to a combination of water depth and breaking waves. The advantages of lidar bathymetry are an excellent complement to the deficiencies of sonar. The depth resolution for lidar can be on the order of centimeters allowing for detection of features even in extremely shallow water. Furthermore, lidar bathymetry is conducted from an airborne platform allowing for bathymetry maps to be constructed in environments completely inaccessible to sonar and since the lidar is located a ways above the water surface, scanning with a bathymetric lidar yields large swaths regardless of the water depth [6].

Although still a developing field, airborne lidar bathymetry, or ALB, is a demonstrated

technique with several notable instruments capable of producing high quality bathymetry data. Typically, an airborne bathymetric lidar uses a pulsed green laser (usually 532 nm) to achieve transmission through water. Many bathymetric lidar systems are multispectral and will also transmit in the IR (usually at 1064) in order to differentiate between the signal scattering off the water surface and off the ocean floor[8][9]. Notable examples are CZMIL (Coastal Zone Mapping and Imaging Lidar) or SHOALS (Scanning Hydrographic Operational Airborne Lidar Survey) which have already been used to produce seamless topographic/bathymetric datasets for coastal regions of the United States[1][10][11]. ALB examples are shown in figure 1.1.

Figure 1.1: Lidar bathymetry in action with the SHOALS system over Hawaii (left)[1]. Bathymetric lidar point cloud obtained over Lake Ontario, courtesy of NOAA (right)[12].

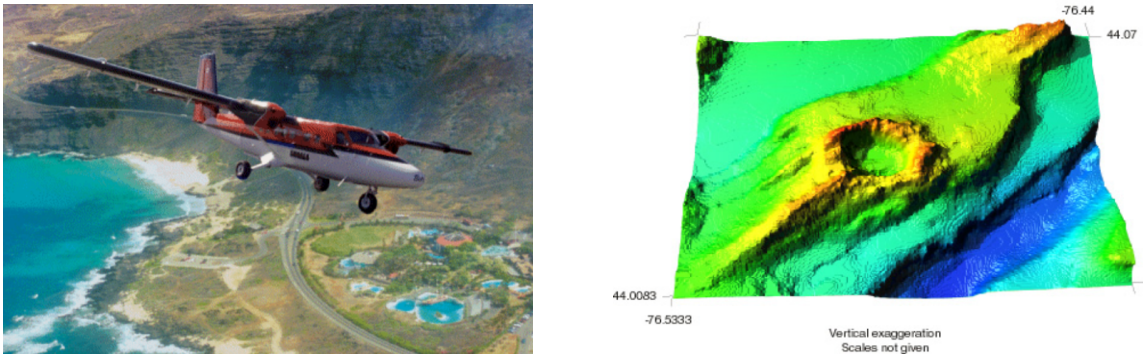

In the active remote sensing laboratory at CU (ARSENL) a fixed beam bathymetric lidar was developed several years ago which records water depth using a different, novel technique. This lidar (known as INPHAMIS 1 for INtrapulse PHAse Modification Induced by Scattering) uses the polarization properties of water to differentiate between the surface and floor signals using a single 532 nm laser. By transmitting linearly polarized light, the polarization maintaining, specularly scattered surface signal can be optically filtered from the depolarized, diffusely scattered floor signal so that the two signals can be independently detected[13][14]. This eliminates much of the uncertainty associated with identifying the two surfaces that often motivates the design of bathymetric lidars since the two surface responses are inherently separate and do not need to be deconvolved. This gives the system the capability to resolve features in exceptionally shallow

waters. Another important design feature of the INPHAMIS 1 lidar is it's photon counting mode of signal detection. As opposed to detecting and recording the full waveform of the return signal, INPHAMIS 1 records the return times of single photons. This allows the system to operate with lower laser power. Additional benefits exist with shortening the impulse response of the receiver and reducing overall cost.

Airborne lidar bathymetry requires harmonious interaction between many complex subsystems and as such, the accuracy of ALB measurements is heavily dependent on many different factors. Uncertainties related to aircraft position, lidar mounting, the laser light propagation, the subsurface scatterer, signal detection timing, and noise all contribute to the final uncertainty in the bathymetry data[6]. One of the main contributors to this total uncertainty, and one of the most poorly understood, is the effect of the ocean surface on ALB[9][15]. In the most simple case, that of a perfectly flat ocean surface, the ocean surface can still alter the lidar measurements by refraction for off nadir pointing. Typically for this situation, these effects can be mostly corrected resulting in only a slight effect on the total uncertainty. Unfortunately, the water surface for ALB is rarely this simple and can exhibit a large range of complex behavior. For large bodies of water, such as the coastal regions most commonly surveyed by ALB, the dominant behavior is waves. The effect of waves on ALB varies and is dependent on the scale of the lidar beam relative to the scale of the surface waves. The size of the footprint for bathymetric lidar varies greatly depending on the instrument with older instruments having larger footprints sometimes on the order of tens of meters. It has been proposed that with a large footprint, wave effects can be reduced since multiple wave cycles will be averaged into each measurement[9][16]. However, this comes at the cost of severely reduced spatial resolution. Additionally, wave effects on a scale smaller than the lidar footprint will cause significant broadening in the impulse scattering response of the water surface. Modern ALB systems typically utilize a much smaller beam divergence resulting in footprints on the order of meters or tens of centimeters in some cases. On this scale, the significant types of ocean waves are wind-driven gravity waves and capillary waves. Capillary waves are typically a couple centimeters in length at most. These waves affect lidar measurements in that they can cause spread in the

surface signal and beam spread upon refraction[9]. Additionally, these waves are responsible for surface glint which our system counts on in order to detect specular surface reflections in the case of angled incidence. However, due to the small scale of these waves in relation to the lidar footprint, wind-driven waves are typically responsible for primary, macroscopic effects[17][3].

This thesis will focus on the development of a combined lidar/ocean wave model to better understand the effect water surface conditions have on lidar bathymetry. Although research has already been conducted to develop lidar-ocean surface models, these models either are not designed to capture gravity wave effects, do not describe a modern ALB system, or are designed to focus on a single ALB effect such as the surface reflection or water column scattering as opposed to how the ocean, as a whole, affects the ALB product[18][16][19][20][21]. ALB technology has progressed such that current systems are narrow-beam, capable of scanning, and much faster[3]. This model is unique in it's ability to portray how a wavy ocean surface affects the signal received by the lidar and how this received signal translates into errors in the lidar measurements.

The lidar/ocean wave model functions by simulating a wavy ocean surface using a superposition of sinusoids and then propagating a collection of rays through the surface to simulate a lidar measurement. Refraction is considered for each ray causing changes in the ray path, power, and polarization. The lidar return signal can then be determined for each ray according to the polarization dependent form of the lidar equation. The time of flight for each ray can be determined from this simulation by calculating the distribution of the received detection times. This allows for representation of the return signal received by the lidar. Both the signal reflected off the ocean surface and the signal reflected off the ocean floor are modeled to simulate the signal received by the two detector channels of the INPHAMIS 1 system. Depending on the ocean conditions in the region of the lidar beam, a variety of different effects can occur.

By comparing the simulated lidar returns from the ocean floor and from the ocean surface, the depth measured by the lidar, along with the height of the ocean surface, can be modeled. From here, important ALB errors can be investigated such as depth uncertainty, surface height uncertainty, and transverse coordinate uncertainty (uncertainty in the x-y location of the measured

point). These wave-related uncertainties can impose limits on the application of ALB for different sea state conditions. The depth and surface distributions experienced on a single ALB measurement provide insight into the uncertainty introduced by a wavy water surface. The horizontal coordinate errors govern the spatial resolution of the ALB measurements and are caused by deflection of the beam and spreading of the beam. At last the expected distribution of lidar measurements over many measurements is simulated to better understand how the ocean surface affects ALB measurements taken over a longer period of time. Although single measurement uncertainties do appear in these distributions, the main effect comes from the distribution of ocean surface height. As a result, these distributions contain information about the ocean environment.

This leads to an important question which we seek to answer: can lidar be used for ocean surface sensing, and if so, how? With ICESat-2, a spaced based lidar, now operational, this question is beginning to garner more interest[22][18]. Typically ocean surface information such as significant wave height is obtained from a radar satellite. An airborne lidar operates on a completely different scale and extraction of ocean wave information would therefore need to be done using different techniques. Using the simulated lidar distributions over many measurements, the ability to extract information such as significant wave height, mean sea level, and average depth will be investigated. The presence of ocean waves can be seen in experimental INPHAMIS 1 data from a recent flight campaign over the Pacific Ocean. These waves are analyzed in order to relate real airborne lidar ocean wave measurements to the models presented in this thesis. By looking at the distribution of these measurements, the ability to extract ocean surface information is tested. Additionally, the INPHAMIS 1 wave data can be compared to the lidar-ocean model results to help validate the model. This is done by analyzing the spectral content of the data. To do this, the expected spectral distribution of the lidar signal is derived for given ocean conditions. This derivation is based off converting the theoretical directional spectral density of the ocean waves into that seen by a fixed beam lidar aboard a moving aircraft.

1.1 Basic Principles

Creating a realistic model of waves on the ocean surface is the first step in developing the lidar/ocean model described in this thesis. The software modeling of realistic ocean surfaces is an extensively researched field with a great deal of effort coming from the computer graphics industry. Three popular methods for simulating oceanscapes are Computational Fluid Dynamics (CFD), Smoothed Particle Hydrodynamics (SPH), and Fourier transform analysis. All three of these methods are based off the Navier-Stokes equations, the governing equations for fluid dynamics. CFD functions by numerically approximating the Navier-Stokes equations using a 3D mesh[23]. This method is advantageous for simulating volumetric effects. SPH imagines the fluid as a volume of overlapping particles. The Navier-Stokes equations are then applied to these particles to model their motion. This model is excellent when modelling conditions such as splashing and spray[24]. For large scale surface simulations, both these models are limited due to computational expense.

Figure 1.2: Examples of the three different techniques used to model water behavior. These are (from left to right): CFD[23], SPH[25], and Fourier analysis[26]. The strengths of each method can be seen from they behavior they are able to capture.

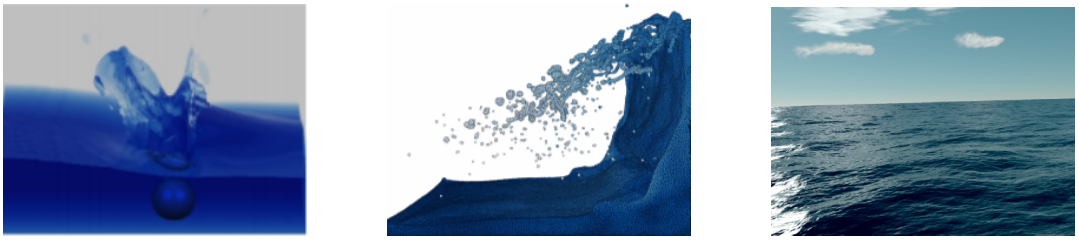

Computational expense along with the necessity to capture many sizes of waves makes the final method, the Fourier model, the best choice for ALB modeling. At a high level, the Fourier transform model works by summing sinusoids with different spatial frequencies over a bound area. The amplitudes of each sinusoidal component are based off a realistic frequency power spectrum. The ocean surface height field can then be expressed mathematically as a truncated 2-D complex

Fourier series as shown below[26].

$$h(\vec{x},t) = \sum_{\vec{k}} \widetilde{c}(\vec{k},t) e^{i(\vec{k}\cdot\vec{x})} \tag{1.1}$$

Here, $h(\vec{x},t)$ is the ocean height at a time t and x-y location $\vec{x} = \langle x, y \rangle$, $\widetilde{c}$ is the complex Fourier coefficient, and $\vec{k}$ is the wavenumber vector. Conveniently, this equation closely parallels that of an ifft (inverse fast Fourier transform) allowing for the ocean height field to be quickly calculated over a grid using readily available software. This model is restricted in that only the surface is modelled and effects such as viscosity and surface tension are ignored. Conveniently for ALB modeling, these limitations are mostly irrelevant.

For lidar bathymetry to be added to this simulation, a lidar location and pointing direction must be defined with respect to the simulated surface. To best represent ALB, an aircraft frame is simulated with a lidar frame rigidly attached. Polarization is defined in the lidar frame by way of a Stoke's vector

$$\vec{S} = \begin{bmatrix} S_0 \\ S_1 \\ S_2 \\ S_3 \end{bmatrix}$$

the components of which are the total intensity (S_0), the difference between horizontally and vertically polarized light (S_1), the difference between +45deg and -45deg polarized light (S_2), and the difference between right hand circularly polarized and left hand circularly polarized light (S_3). The lidar beam is approximated using a collection of rays of discrete width. Each ray represents a portion of the lidar beam solid angle and power as determined from the beam intensity distribution. The timing for each ray is found by projecting and tracing the rays through the simulated surface and back according to Snell's law.

$$n_1 sin(\theta_1) = n_2 sin(\theta_2) \tag{1.2}$$

The power and polarization of the received rays is modeled according to the Stoke's vector

lidar equation adjusted for bathymetry[27]. This equation accounts for all interactions along the optical path for a lidar measurement, including, attenuation, depolarization, and scattering.

In software, re-creating the lidar/aircraft/ocean measurement environment is clean and simple whereas in a real world scenario, relating these three references can be complicated and laden in uncertainty. This process is denoted as georeferencing and involves comparing the lidar point cloud to a representation of the Earth's surface in global coordinates[28]. For real INPHAMIS 1 flight data, this is done by combining IMU, GPS, and lidar range data along with a Mean Sea Surface (MSS) geoid. In this form, the ocean waves can be identified in the lidar data and compared to the model. Information regarding the surface conditions can be extracted using the variance of the data or by looking at the spectral content. Although for our data no floor detections exist, the georeferencing process would also allow for a subsurface map to be constructed and referenced to a geoid.

Chapter 2

Lidar-Ocean Model

As with all fluids problems, the mathematical basis for the Fourier solution to ocean waves can be traced back to the Navier-Stokes equations. The full Navier-Stokes equations are notoriously complicated and cannot be solved analytically therefore solutions are obtained either through numerical approximation or significant simplifications to the governing equations. For many problems, the full Navier-Stokes equations are not required as is the case with ocean modelling for ALB applications. From the simplified Navier Stokes equations, a partial differential equation can be derived which can be solved using Fourier series methods. A variety of different parameters can influence this solution such as amplitude of each sinusoid, angular frequency, wavenumber, and initial phase. The solution of the governing PDE gives an expression for wave speed based off a fixed relationship between wavenumber and angular frequency known as the water wave dispersion relation.

Although this provides a general form in agreeance with physical theory, the realistic nature of the resultant surface is heavily dependent on the power spectrum used to find the magnitudes of the superimposed waves. For this analysis, a commonly used ocean power spectral density model known as the JONSWAP spectrum will be employed. Variations in the JONSWAP parameters and their effect on producing a realistic spectrum are investigated. The JONSWAP spectrum, along with many other spectra, are continuous and given in terms of angular frequency. For our purposes, these spectra must be converted to a discretized form, described in terms of wavenumber. Care must be given to this conversion in order to ensure conservation of energy and variance.

2.1 Theoretical Basis

2.1.1 Derivation of PDE

We start with the Navier-Stokes equations for incompressible flow (an excellent approximation for water) and neglect heat transfer and viscosity. The omission of heat transfer is an acceptable approximation for ocean surface modeling since the surface is mostly constant in temperature on a local scale. Neglecting viscosity is impactful for small scale effects and for volumetric effects. For the scale of ocean behavior that this model is designed for, neglecting viscosity is acceptable. Furthermore, effects on this scale can still be captured by adding a correction condition after a solution has been found. With these assumptions, the incompressible Navier Stokes equations reduce to the Euler equations for flow

$$\begin{aligned} \frac{\partial \vec{u}}{\partial t} + \vec{u} \cdot \nabla \vec{u} &= -\nabla p + \vec{F} && (2.1) \\ \nabla \cdot \vec{u} &= 0 && (2.2) \end{aligned}$$

where p($\vec{r}$,t) is the pressure, $\vec{F}$ is the force the fluid is subjected to, and $\vec{u}$($\vec{r}$,t) is the flow velocity vector, and $\vec{r}$ is a 3D position $\langle x, y, z \rangle$[29]. For our purposes, the height of the surface, not the flow velocity vector is desired. Fortunately, since the force applied to the fluid, $\vec{F}$, is due to gravity and is therefore conservative, we can assume potential flow and relate the vector field $\vec{u}$($\vec{r}$,t) to a scalar field as shown below in Eq. (2.3). Additionally, the force vector $\vec{F}$ can be related to a scalar potential field based off gravitational potential. This latter relationship implies that the main force acting on the fluid is gravity.

$$\begin{aligned} \vec{u}(\vec{r}, t) &= \nabla \phi(\vec{r}, t) \\ \vec{F} &= -\nabla g h && (2.3) \\ g &\approx 9.8 \ \frac{m}{s^2} \end{aligned}$$

Under these conditions, equation 2.1 can be transformed into the form shown below.

$$\frac{\partial \phi}{\partial t} + \frac{1}{2}(\nabla \phi)^2 = -p - gh \tag{2.4}$$

$$\nabla^2 \phi(\vec{r}, t) = 0 \tag{2.5}$$

Although quite the reduction in comparison to the full Navier-Stokes equations, Eq. (2.4) and (2.5) are still quite challenging. Further assumptions can be made for the problem specific to this model. Firstly, Eq. (2.4) is nonlinear. Linearizing this equation will make it much easier to solve however the nonlinear effects will be lost. It is important to consider how much this will affect the validity of the solution. To linearize this equation, the $\frac{1}{2}(\nabla \phi)^2$ term will be removed. This term involves second order spatial derivatives and would only be significant if the potential velocity ϕ was changing rapidly with respect to time. By neglecting this, the ability to accurately model breaking/extremely choppy waves is lost. This should be considered when this model is applied to the physical world. The next assumption made to simplify the problem is to neglect all points not on the water surface. The water surface itself can now be described as a height field, h, dependent on x, y, and t. By doing this, fluid motion in the horizontal plane is prohibited. This assumption should be taken into consideration if this model is to be used in the presence of significant ocean current or a riverine environment. Since this height field is dependent only on x and y spatial coordinates, a new position vector which describes points in the horizontal plane is defined as $\vec{x}$ as is consistent with Eq. (1.1).

By only looking at points on the water surface, ϕ becomes dependent only on $\vec{x}$. Eq. (2.5) then becomes:

$$\left(\nabla_{x,y}^2 + \frac{\partial^2}{\partial z^2}\right) \phi(\vec{x}, t) = 0 \tag{2.6}$$

To proceed, some partial differential trickery must be applied. Eq. (2.6) is generally true if $\frac{\partial}{\partial z}$ is chosen to equal $\pm\sqrt{-\nabla_{x,y}^2}$. With this condition in place, the relationship between $\vec{u}$ and ϕ can now

be written as [26]:

$$\vec{u} = (\nabla_{x,y}\phi)\vec{x} \pm (\sqrt{-\nabla^2_{x,y}}\phi)\hat{z} \tag{2.7}$$

Since fluid motion is restricted to the vertical direction, the component of the flow velocity in the horizontal direction drops out. The component of $\vec{u}$ in the vertical direction is identical to the rate of change of the height field in time so Eq. (2.7) can further be simplified to:

$$\frac{\partial h(\vec{x},t)}{\partial t} = \pm\sqrt{-\nabla^2_{x,y}}\phi(\vec{x},t) \tag{2.8}$$

The final simplification made in this analysis is to remove the pressure p from Eq. (2.4). Since the flow is now only being considered on the surface, the pressure field is relatively invariant (equal to the pressure at sea level). If p is a constant in Eq. (2.4), it's value is unimportant to the general solution and as such, can be chosen to be 0. Along with the linearization made earlier, these assumptions change Eq. (2.4) to the form shown below in Eq. (2.9). It can now be seen that the omission of p is acceptable since it would simply manifest as a constant of integration when integrating the left side of this equation.

$$\frac{\partial \phi(\vec{x},t)}{\partial t} = -gh(\vec{x},t) \tag{2.9}$$

With Eqns. (2.8) and (2.9), we can now proceed to defining the PDE that will be used going forward. By taking the derivative of Eq. (2.8) with respect to time, the following is obtained:

$$\frac{\partial^2 h(\vec{x},t)}{\partial t^2} = \pm\sqrt{-\nabla^2_{x,y}}\frac{\partial \phi(\vec{x},t)}{\partial t} \tag{2.10}$$

By substituting Eq. 2.9 into the above, an expression can be obtained in terms of $h(\vec{x},t)$ alone.

$$\frac{\partial^2 h(\vec{x},t)}{\partial t^2} = \pm g\sqrt{-\nabla^2_{x,y}}h(\vec{x},t) \tag{2.11}$$

This equation would be satisfactory if not for $\sqrt{-\nabla^2_{x,y}}$ operator. By applying two more time derivatives to Eq. (2.11), this problematic operator can be removed by substituting Eq. (2.11) into

it's original form to produce Eq. (2.12).

$$\frac{\partial^4 h(\vec{x},t)}{\partial t^4} = -g^2 \nabla^2_{x,y} h(\vec{x},t) \tag{2.12}$$

This is the governing PDE for solving the surface wave equation that will be used in this paper[26]. It is homogeneous and therefore solutions form a vector space making Fourier series a clear solution choice.

2.1.2 General Solution to PDE

The first step in solving Eq. (2.12) is to define boundary conditions. For the purpose of this model, boundary conditions were selected so that simulated ocean grid could be tiled and extended. Therefore, the slope and the height at every boundary must be equal. Temporally, there are also restrictions. Namely, as time increases towards infinity, the wave height must be bound. Additionally, as time goes to negative infinity, the wave weight must be bound. These waves do not originate at time t=0 which is why the negative time constraint must be imposed. At last, the bound space on which this equation will be solved must be defined. Any sized grid will work so an arbitrary grid bound by [-L_x/2,L_x/2] and [-L_y/2,L_y/2] is selected.

The next step is to guess that the solution is composed of an independent function of t multiplied by a function of $\vec{x}$.

$$h(\vec{x},t) = F(\vec{x})G(t) \tag{2.13}$$

By plugging this guess into the original PDE, we obtain:

$$\frac{1}{-g^2 G(t)} \frac{\partial^4 G(t)}{\partial t^4} = \frac{1}{F(\vec{x})} \nabla^2 F(\vec{x}) \tag{2.14}$$

Since each side of this equation is independent, the entire equation can be set to equal a constant, λ. We now have two different, more simple differential equations two solve. Starting with the

equation for F, we consider the case of λ greater than 0. We must now expand the ∇ operator.

$$\lambda F(x,y) = \frac{\partial^2 F}{\partial x^2} + \frac{\partial^2 F}{\partial y^2} \tag{2.15}$$

By doing this, we have effectively created a new PDE which must be solved. Once again, we guess that the solution is composed of the product of solutions independent in x and y.

$$F(\mathbf{x}) = X(x)Y(y) \tag{2.16}$$

By plugging Eq. (2.16) into Eq. (2.15), the following equation is obtained.

$$\lambda = \frac{1}{X}\frac{\partial^2 X}{\partial x^2} + \frac{1}{Y}\frac{\partial^2 Y}{\partial y^2} \tag{2.17}$$

Once again, we know each term on the right side of this equation is independent of each other, and therefore, constant relative to each other. The following equivalence is thereby valid.

$$-\frac{1}{Y}\frac{\partial^2 Y}{\partial y^2} + \lambda = \frac{1}{X}\frac{\partial^2 X}{\partial x^2} = \lambda_x \tag{2.18}$$

In this form, X(x) can be solved for. To do this, we start by considering every form of λ_x. Starting with lambda = 0, we get the well defined solution X(x) = A(x) + B. When the boundary conditions are invoked, we find A = 0 since the value X($L_x/2$) doesn't equal X(-$L_x/2$). B however can be nonzero. It is later shown these nonzero constant terms simply define the base height of the ocean surface.

Next, a positive λ is considered. These solutions are of the form:

$$X(x) = Ae^{\sqrt{\lambda_x}x} + Be^{-\sqrt{\lambda_x}x} \tag{2.19}$$

This time, after invoking the boundary conditions we find that A and B are zero. This is because A must equal B from the X($L_x/2$) and X(-$L_x/2$) condition. However, under this condition, X(x) reduces to a form of cosh which is unequal in slope at X($L_x/2$) and X(-$L_x/2$).

The final condition for λ_x to consider is a negative λ_x. The general such solution is shown below.

$$X(x) = Acos(\sqrt{\lambda_x}x) + Bsin(\sqrt{\lambda_x}x) \tag{2.20}$$

By applying the boundary conditions to this instance, we find that there are acceptable values for A and B. Both boundary conditions are satisfied so long as λ_x equals $(\frac{2\pi n}{L_x})^2$. From here on out, the constant $\sqrt{\lambda_x}$ is defined as k_x. With the solution for X complete, we now move to solving for Y. When the same operation done to isolate X is performed on Y, we get:

$$\lambda + k_x^2 = \frac{1}{Y}\frac{\partial^2 Y}{\partial y^2} = \lambda_y \tag{2.21}$$

The solution to this equation is identical to that just obtained for X. Therefore, we can skip the derivation and conclude that $-(\frac{2\pi m}{L_y})^2 = \lambda_y$. From here, λ can be written in terms of k_x and k_y.

$$\lambda = -(k_x^2 + k_y^2) \tag{2.22}$$

Since the term on the right is a strictly negative, it can be concluded that λ is negative. This is necessary information for solving G(t). The differential equation which governs G(t) can be obtained from Eq. (2.14).

$$\frac{\partial^4 G(t)}{\partial t^4} = -\lambda g^2 G(t) \tag{2.23}$$

When solving for G(t), it is useful to replace λ with a different constant squared. From eq. 2.22, it can be seen that a convenient constant would be k^2 where k is the magnitude of a vector, $\vec{k}$ comprised of k_x and k_y . The general solution for the equation for G(t) with a negative λ is shown below.

$$G(t) = Acos(\sqrt{gk}t) + Bsin(\sqrt{gk}t) + Ce^{\sqrt{gk}t} + De^{-\sqrt{gk}t} \tag{2.24}$$

There are a lot of terms and possible solutions to this equation. Fortunately, some terms drop out when the constrictions placed on this model are applied. The two constrictions placed on the time dependent solutions to PDE are that the solution must be bound as t goes to both negative and positive infinity. Under these constraints, it is clear that C and D must be zero. The terms related to C and D cause exponential growth which, if included in the solution, will eventually create infinitely large waves. The solutions related to A and B however are valid. The only constraint is that the angular frequency, ω, of these waves must be $\sqrt{gk}$. This is a well documented phenomenon known as the deep wave dispersion relation.

$$\omega^2 = gk \tag{2.25}$$

Now that analytical solution sets have been developed for X, Y, and G, it is time to reassemble the solution for h. All three solutions are a combination of cosines and sines with undefined magnitudes. Therefore, it is convenient to convert to a complex Fourier series. The solution sets for X, Y, G, and h are shown in this form below.

$$\begin{aligned} X(x) &= C_1 + \sum_{k_x} \widetilde{A} e^{ik_x x} \\ Y(y) &= C_2 + \sum_{k_y} \widetilde{B} e^{ik_y y} \\ G(t) &= C_3 + \sum_{w} \widetilde{C} e^{i\omega t} \end{aligned} \tag{2.26}$$

$$h(\vec{x}, t) = C + \sum_{\vec{k}} \widetilde{c_o}(\vec{k}) e^{i(\vec{k}\cdot\vec{x} \pm \omega t)} \tag{2.27}$$

$$k_x = \frac{2\pi n}{L_x}, \qquad k_y = \frac{2\pi m}{L_y}, \qquad \vec{k} = \langle k_x, k_y \rangle, \qquad k = \sqrt{k_x^2 + k_y^2}, \qquad \omega(k) = \pm\sqrt{gk} \tag{2.28}$$

There are several key takeaways from this solution. Most obviously, it can be seen from eq. 2.27 that the general solutions to the problem posed in this project are waves propagating in

various directions. This is as expected and is a good indication that the mathematics governing the model are sensible

Secondly, the constant value solutions to X, Y, and G can be seen once again as a constant offset in the final solution. This constant defines the base ocean level or "sea" level as one might say. In general, this constant is set to zero, however, for comparison with real lidar surface data, it can be used to account for systematic offsets.

Additionally, the fact that the final solution is a single summation is deceiving. Since the summation is over all $\vec{k}$ and since $\vec{k}$ is a vector, this is really two summations. One summation ranges over k_x and the other over k_y. It should also be noted that both summations range from negative to positive infinity, a trait of complex Fourier series. Additionally, for every k vector, there are two possible solutions for w. Therefore, for every $\vec{k}$, a forward and backward propagating wave must be considered.

One of the more interesting revelations from this analysis is the direct dependency of w on k. Another way to say this is that the speed of all waves in this model is directly related either to their spatial size or to their angular frequency. The speed of a wave is given by ω/k or $\sqrt{g/k}$. Therefore, waves with a large wavelength (small k) travel faster than waves with a small wavelength.

2.2 Numerical Implementation

Some adjustments must be made to Eq. (2.27) before it can be used in a numerical model. Firstly, the summation in Eq. (2.27) goes to infinity and must be truncated in order to be used. This will result in unaccounted energy at higher frequencies. Fortunately, this incurs minimal error since the vast majority of the energy for the JONSWAP spectrum is concentrated at lower frequencies. If the summation is limited to N k_x values and M k_y values, the discrete k_x and k_y series can be determined. Since negative frequencies must be included, the bounds are $[-\frac{\pi N}{L_x}, \frac{\pi N}{L_x}]$, and $[-\frac{\pi M}{L_y}, \frac{\pi M}{L_y}]$. If the summation is limited to N k_x values and M k_y values, the discrete k_x and k_y series can be determined. Since negative frequencies must be included, the bounds are $[-\frac{\pi N}{L_x}, \frac{\pi N}{L_x}]$, and $[-\frac{\pi M}{L_y}, \frac{\pi M}{L_y}]$. Another slight change going from the theoretical model to the software implementation is how

the positive and negative e^{iwt} terms are handled. Since both must be considered, it is convenient to move the time dependency into the $\widetilde{h}_o(k)$ term. This term then becomes $\widetilde{h}(k,t)$. Since the series being summed can be complex, $h(\vec{x},t)$ must be completely real in order for the model to make physical sense. For this to be true, the value of $\widetilde{h}(k,t)$ must be the complex conjugate of $\widetilde{h}(-k,t)$ and therefore takes the following form[26][17].

$$\widetilde{c}(\vec{k},t) = \widetilde{c_o}(\vec{k})e^{i\omega(k)t} + \widetilde{c_o}^*(-\vec{k})e^{-i\omega(k)t} \tag{2.29}$$

This allows us to form Eq. (1.1) from Eq. (2.27). This equation will be restated as it is important going forward and the variables in it warrant further discussion.

$$h(\vec{x},t) = \sum_{\vec{k}} \widetilde{c}(\vec{k},t)e^{i(\vec{k}\cdot\vec{x})}$$

The height field is h($\vec{X},t$), the x-y position vector is $\mathbf{x}$, the time is t, the Fourier coefficient is $\widetilde{c}$, and the wavenumber vector is $\mathbf{k}$. The summation is a double summation over both the x and y components of the wavenumber vector. The wavenumber vector is given by $\mathbf{k} = (2\pi n/L_x, 2\pi m/L_y)$. The bounds on the integers n and m are $-N/2 \leq n < N/2$ and $-M/2 \leq m < M/2$. N and M are the number of discrete frequencies used in the x and y directions. This also determines the number of points in the x and y directions for the spatial grid that corresponds to the output of the inverse fft algorithm when applied to Eq. (1.1). L_x and L_y are the length of the ocean rectangle to be simulated in the x and y directions respectively. The x and y points at which the inverse fft algorithm calculates heights are given by $\mathbf{x} = (nL_x/N, mL_y/M)$ with n and m ranging from 0 to N and 0 to M. To use Eq. (1.1) with an inverse fft algorithm, a complex spectral amplitude matrix can be assembled at any time t with elements in correspondence to each item in the two dimensional k vector. Although the inverse fft algorithm has the advantage of speed, it is disadvantaged in that it can only determine the surface height at the gridded points. For this reason, it should only be used for aesthetics. The height of the surface at any arbitrary x-y location can be determined simply by evaluating Eq. (1.1) manually. For lidar modelling, it is also important to be able to calculate the

slope of the surface. This can be done analytically by taking the gradient of $h(\vec{x},t)$ with respect to $\vec{x}$[26].

$$\nabla h(\vec{x},t) = \sum_{\vec{k}} i\vec{k}\widetilde{c}(\vec{k},t)e^{i(\vec{k}\cdot\vec{x})} \tag{2.30}$$

Using this equation, the slope of the surface in the x and y directions can be found at any point. For tracing the lidar beam through the water, the normal to the surface is required. The normal to the surface is calculated by converting $\frac{\partial h}{\partial x}$ and $\frac{\partial h}{\partial y}$ into a vector form and then taking their cross product. The $\frac{\partial h}{\partial x}$ and $\frac{\partial h}{\partial y}$ vectors are each tangential to the surface at the chosen x-y location so their cross product produces a vector that is perpendicular to both of them, and to the surface. In order to make this normal vector consistent across the surface, the result of the cross product is scaled so that it is a unit vector with a positive z component.

2.2.1 Determining the Spectral Amplitudes

The final step in the development of this model is the generation of the complex coefficient, $\widetilde{c}(\vec{k},t)$, based off a power spectral density model. The method by which the continuous power spectral density will be converted to Fourier component amplitudes relies on analyzing and equating the power in the two representations. To start, we will look at the power in the Fourier series approximation of the ocean surface. The formula that will be used gives the time averaged power of some temporal signal x(t). The time averaged power is necessary since the ocean surface height field is nonzero over all space and time. This formulation is shown below, in terms of the ocean height field h, in Eq. (2.31).

$$P = \frac{1}{T}\int_0^T |h(\vec{x},t)|^2 dt \tag{2.31}$$

The term for the ocean height field in Eq. (2.31) can be replaced with Eq. (1.1).

$$P = \frac{1}{T}\int_0^T |\sum_{\vec{k}} \widetilde{c}(\vec{k},t)e^{i(\vec{k}\cdot\vec{x})}|^2 dt \tag{2.32}$$

In order for the power in the Fourier model to be useful, Eq. (2.31) must be manipulated to give the Fourier amplitudes. To start, Eq. (1.1) should be rearranged into a simpler form. To start, $\widetilde{c}(\vec{k},t)$ will be decomposed.

$$\widetilde{c}(\vec{k},t) = \widetilde{c}_o(\vec{k})e^{i\omega t} + \widetilde{c}_o^*(-\vec{k})e^{-i\omega t} \tag{2.33}$$

$$\widetilde{c}(-\vec{k},t) = \widetilde{c}_o(-\vec{k})e^{i\omega t} + \widetilde{c}_o^*(\vec{k})e^{-i\omega t} \tag{2.34}$$

$$\widetilde{c}_o(\vec{k}) = C_o(\vec{k})e^{i\phi} \tag{2.35}$$

With the above equations substituted into Eq. (1.1), the summation can be rearranged and simplified. This is done by taking the first term on the right side of Eq. (2.33) and combining it with the second term on the right side of Eq. (2.34) so that the $\widetilde{c}_o^*(-\vec{k})$ term in the summation is reassigned to a negative $\vec{k}$. The $\widetilde{c}_o(\vec{k})$ term is a combination of a completely real magnitude ($C_o(\vec{k})$), and a phase (ϕ). The magnitude of each $\widetilde{c}_o(\vec{k})$ term is determined based off the chosen energy spectrum. The phase is a random number between 0 and 2π. Eq. (2.27) reorganized is shown below.

$$h(\vec{x},t) = \sum_{\vec{k}} C_o(\vec{k})(e^{i(\omega t+\vec{k}\cdot\vec{x}+\phi)} + e^{-i(\omega t+\vec{k}\cdot\vec{x}+\phi)}) \tag{2.36}$$

In this form, the complex exponentials can be simplified. The imaginary components in Eq. (2.36) cancel and all that's left is cosine.

$$h(\vec{x},t) = \sum_{\vec{k}} 2C_o(\vec{k})cos(\omega t + \vec{k}\cdot\vec{x} + \phi) \tag{2.37}$$

With $h(\vec{x},t)$ described in this form, Eq. (2.31) can be evaluated.

$$P = \frac{1}{T}\int_0^T |\sum_{\vec{k}} 2C_o(\vec{k})cos(\omega t + \vec{k}\cdot\vec{x} + \phi)|^2 dt \tag{2.38}$$

At first glance Eq. (2.38) looks quite complicated due to the fact that squaring the summation results in an enormous amount of terms. However, When averaged over time, the only nonzero terms in the square of the summation are the terms with identical wavenumber vectors. This allows us to move the summation outside of the integral, leaving us with the form shown below.

$$P = \sum_{\vec{k}} \frac{1}{T} \int_0^T 4C_o(\vec{k})^2 cos(\omega t + \vec{k} \cdot \vec{x} + \phi)^2 dt \tag{2.39}$$

This integral can now be easily evaluated to produce a much simplified equation for the power contained in the Fourier model. Most importantly, this formulation is completely described in terms of the amplitude of each Fourier component.

$$P = \sum_{\vec{k}} 2C_o(\vec{k})^2 \tag{2.40}$$

2.2.2 JONSWAP Spectrum

For scientific purposes, a simulated ocean surface should be accurate beyond just looking like an ocean surface. The power spectrum used to represent the surface should be based off physical parameters and the spectrum used should be appropriate for the circumstance to be modelled. There are a variety of different spectra which have been used to represent a wavy ocean surface such as the Phillips spectrum and the Pierson-Moskowitz spectrum. The spectrum used in this study, the JONSWAP spectrum (Joint North Sea Wave Observation Project), is an extensively used, more modern spectrum[30]. The JONSWAP spectrum is a modified version of the Pierson-Moskowitz spectrum which was designed to describe wind driven waves on a fully developed sea (meaning the wind has been blowing constantly over a large area for a long time). The JONSWAP spectrum differs in that an artificial peak enhancement factor is added which attempts to capture the idea that the wave spectrum is never fully developed. The main dependencies for the JONSWAP spectrum are on wind speed and fetch length. Fetch length refers to the distance over which there is a constant wind speed so that a mature sea state is produced. The JONSWAP spectrum is defined

according to the following expressions.

$$\begin{aligned} S(\omega) &= \frac{\alpha g^2}{\omega^5} e^{\frac{-5}{4}(\frac{\omega_m}{\omega})^4} \gamma^R \\ R &= e^{-\frac{(\omega-\omega_m)^2}{2\sigma^2\omega_m^2}} \end{aligned} \tag{2.41}$$

In the equation above, ω is the angular frequency of the waves (given in radians per second). Since the Fourier model is described in terms of wavenumber, ω is determined using the dispersion relation, $\omega^2 = gk$. Many of the other parameters in Eq. (2.41) have their own respective formulas as shown below.

$$\alpha = .076\bar{X}^{-.22} \tag{2.42}$$

In this equation, $\bar{X}$ is equivalent to $\frac{gx}{V^2}$ where V is the wind velocity 10 meters above the ocean and x is the fetch length. Typically, α is between .0081 and .01. For the simulations discussed in this paper, it is kept constant at .009. The center frequency of the spectrum w_m can be calculated according to Eq. (2.43).

$$w_m = 22(\frac{g}{V})(\bar{X})^{-.33} \tag{2.43}$$

The final two constants that must be determined are γ and σ. γ is the peak enhancement factor. This value represents the wind-wave growth rate and ranges from 1.5 to 6. The value used in this model is 3.3 [31]. By changing γ, the JONSWAP spectrum can be made to look more or less like the Pierson-Moskowitz spectrum. The shape of the spectrum peak is controlled by σ is the peak shape factor and is determined as shown below.

$$\begin{aligned} \sigma &= .07, \qquad w \leq w_m \\ \sigma &= .09, \qquad w > w_m \end{aligned} \tag{2.44}$$

A typical power spectral density generated with the JONSWAP spectrum is shown below in Fig. (2.1).

Figure 2.1: Example JONSWAP power spectral density. The wind speed was set to 7 m/s.

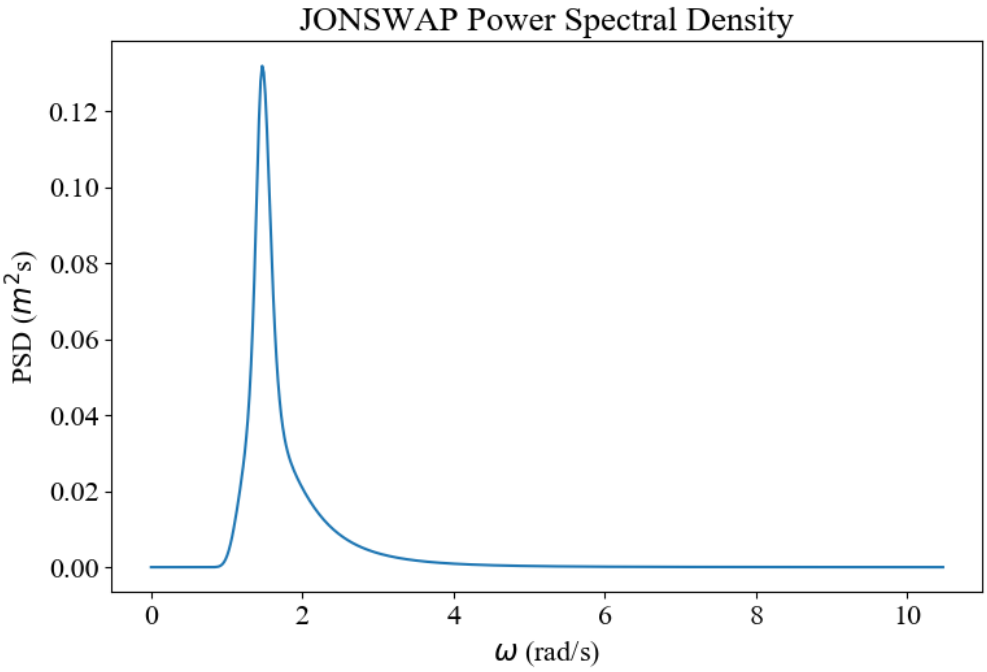

Since the JONSWAP spectrum provides a power spectral density, the total power contained within the spectrum can be found by taking the integral of the spectrum with respect to ω. Ocean power spectral densities also have the trait of an integrated power being equivalent to the surface variance, $\langle\zeta^2\rangle$[17]. This is important for later when statistics are applied to surface. The JONSWAP spectrum is only meant to represent positive frequencies so the integral is bound between 0 and positive infinity.

$$\langle\zeta^2\rangle = P = \int_0^\infty S(\omega)d\omega \tag{2.45}$$

Currently, the JONSWAP spectrum is described solely in terms of ω. This is an issue for our purposes since the spectrum should have directional dependence. Something must therefore be added to the spectrum's formulation such that it becomes S(ω,θ). To do this, a directional

spreading function, D(θ), must be derived. S(ω,θ) will then be found using the definition below. An important condition that must be satisfied by S(ω,θ) is that it's integral must be equal to the integral of S(ω) (equation 2.45).

$$S(\omega, \theta) = S(\omega)D(\theta) \tag{2.46}$$

$$P = \int_0^{2\pi} \int_{-\infty}^{\infty} S(\omega, \theta) d\omega d\theta = \int_{-\infty}^{\infty} S(\omega) d\omega \tag{2.47}$$

Since S(ω,θ) is composed of two functions which are completely independent in ω and θ, each integral can be evaluated separately for the double integral in equation 2.47. Therefore, D(θ) must simply satisfy the condition below.

$$\int_0^{2\pi} D(\theta) d\theta = 1 \tag{2.48}$$

A popular choice for D(θ) involves cos() to some power. A commonly used family of spreading functions are known as the cosine 2s functions. They are of the form A$\cos^{2s}(\theta/2)$. For this model, the s=2 spreading function was chosen from this family[17]. For this to satisfy equation 2.48, it must be scaled by $4/3\pi$. This leaves us with

$$D(\theta) = \frac{4}{3\pi} cos^4(\theta/2) \tag{2.49}$$

In the definition above, a value of θ of zero corresponds to waves travelling in the same direction as the wind. The scaling constant a can be adjusted to control the distribution of energy in forward versus backward travelling waves. This constant is bound between -1 and 1 with 1 resulting in all the spectral energy concentrated in waves travelling in the same direction as the wind. Now that a function for D(θ) has been developed, we can proceed with analyzing S(ω,θ). A visualization of the full, directional spectral density is shown below.

Figure 2.2: JONSWAP power spectrum with wave direction included. The wind speed was set to 7 m/s.

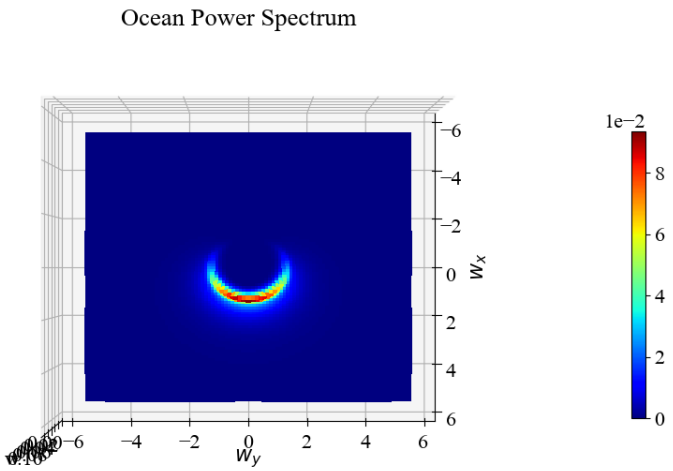

2.2.3 Power Spectral Density to Fourier Amplitude

In order to obtain the amplitudes of the Fourier components from the power spectral density, the two representations of power must be equated. Since the power spectral density representation of power is in the form of an integral it is difficult to directly equate the two forms. The power in S(ω,θ) for each wavenumber vector could be determined by integrating the power spectral density just over that region. This is difficult to do in practice due to the complexity of S(ω,θ). Additionally, computationally evaluating an integral for each $\vec{k}$ would be time consuming. A simpler way to equate the power spectral density and the Fourier amplitudes is to approximate the power spectral density integral as a summation[31]. The various power representations are shown below.

$$P = \sum_{\vec{k}} 2C_o(\vec{k})^2 = \int_0^{2\pi} \int_0^{\infty} S(\omega,\theta) d\omega d\theta \approx \sum_{\theta} \sum_{\omega} S(\omega,\theta) \Delta\omega \Delta\theta \tag{2.50}$$

The form shown above is good in that the power spectral density integral is now avoided. However, the summations for power spectral density and for the Fourier components do not match. If the power spectral density integral could be represented in terms of wavenumber as opposed to ω and θ, then the summations could be equated. The process of converting S(ω,θ) into S($\vec{k}$) will now be discussed.

To start, S(ω) must be converted to S(k). When expressing the power spectral density in terms of k (the magnitude of the wavenumber), the variance must be conserved [32]. This leaves us with Eq. (2.51).

$$\int S(k)kdk = \int S(\omega)d\omega \tag{2.51}$$

Using this equation, S(k) can be found from S(ω). The steps taken to do this are shown below. Eq. (2.53) may seem familiar seeing as it is simply a reformulation of the previously mentioned dispersion relation.

$$S(k) = \frac{1}{k}\frac{d\omega}{dk}S(\omega) \tag{2.52}$$

$$\omega(k) = \sqrt{gk} \tag{2.53}$$

$$\frac{d\omega}{dk} = \frac{1}{2}\sqrt{\frac{g}{k}} \tag{2.54}$$

$$S(k) = \frac{\sqrt{g}}{2k^{\frac{3}{2}}}S(\omega(k)) \tag{2.55}$$

With the ocean theoretical power spectrum now described in terms of wavenumber, we can proceed to adding directionality and converting S(k,θ) to S(**k**). The various forms of S and their equivalences are shown below.

$$\int_0^{2\pi}\int_0^{\infty} S(\omega,\theta)d\omega d\theta = \int_0^{2\pi}\int_0^{\infty} S(k,\theta)kdkd\theta = \int_{-\infty}^{\infty}\int_{-\infty}^{\infty} S(\vec{k})kdk_xdk_y \tag{2.56}$$

As can be seen from Eq. (2.56), in order to obtain S(**k**), dkdθ must be converted to dk$_x$dk$_y$. Change of variables in the presence of a double integral is done using a Jacobian. To do this, k and θ must first be expressed in terms of $\vec{k}$ = (k$_x$,k$_y$).

$$k = \sqrt{k_x^2 + k_y^2} \tag{2.57}$$

$$\theta = tan^{-1}(k_y/k_x) \tag{2.58}$$

The formula for the Jacobian with these variables is shown below.

$$\frac{dkd\theta}{dk_x dk_y} = \begin{vmatrix} \frac{\partial k}{\partial k_x} & \frac{\partial k}{\partial k_y} \\ \frac{\partial \theta}{\partial k_x} & \frac{\partial \theta}{\partial k_y} \end{vmatrix} \tag{2.59}$$

When evaluated, this becomes:

$$\frac{dkd\theta}{dk_x dk_y} = \begin{vmatrix} \frac{k_x}{\sqrt{k_x^2+k_y^2}} & \frac{k_y}{\sqrt{k_x^2+k_y^2}} \\ \frac{-k_y}{k_x^2(1+(\frac{k_y}{k_x})^2)} & \frac{1}{k_x(1+(\frac{k_y}{k_x})^2)} \end{vmatrix} = \frac{1}{\sqrt{k_x^2 + k_y^2}} \tag{2.60}$$

The conversion between dkdθ and dk$_x$dk$_y$ is the last step in expressing the power spectrum in terms of the wavenumber vector. S($\vec{k}$) can now be defined and the integral of S(ω,θ) can be written in terms of $\vec{k}$.

$$S(\vec{k}) = \frac{\sqrt{g}}{2(k_x^2 + k_y^2)^{\frac{5}{4}}} S(\omega(\vec{k}), \theta(\vec{k})) \tag{2.61}$$

$$P = \int_0^{2\pi} \int_0^{\infty} S(\omega, \theta) d\omega d\theta = \int_{-\infty}^{\infty} \int_{-\infty}^{\infty} \frac{\sqrt{g}}{2(k_x^2 + k_y^2)^{\frac{3}{4}}} S(\omega(\vec{k}), \theta(\vec{k})) dk_x dk_y \tag{2.62}$$

When approximated as a summation, it is now clear how the Fourier amplitudes and power spectrum are related. Using Eq. (2.56) (and in practice Eq. (2.62)), the power spectrum can be converted

to a summation over $\vec{k}$. The summations are identical in $\vec{k}$ allowing us to come up with a direct equation for $C_o(\vec{k})$ that can be used with the Fourier based model implementation.

$$\sum_{\vec{k}} 2C_o(\vec{k})^2 = \sum_{\vec{k}} S(\vec{k})k\Delta k_x \Delta k_y \tag{2.63}$$

$$C_o(\vec{k}) = \sqrt{\frac{S(\vec{k})k\Delta k_x \Delta k_y}{2}} \tag{2.64}$$

When modeling ocean surface behavior with the Fourier series approach, Eq. (2.64) is the equation to use for determining the amplitudes of the Fourier components when a theoretical power spectral density is used. Using a theoretical power spectrum, based on physical parameters, that is described in terms of ω without properly converting into Fourier amplitudes can easily produce significantly erroneous results. The simulated surface may still take on the appearance of an ocean, but the actual behavior of the ocean waves will not be correct.

2.2.4 Random Behavior

Oceanographic research involving analysis of buoy height and radar measurements indicates that the ocean wave amplitudes are well described as statistically stationary, independent, Gaussian fluctuations[26]. This behavior can be added to the model by making the Fourier amplitudes random variables. The amplitude will still be based off Eq. (2.64) however for each time t it will now be scaled by a draw from a Gaussian distribution. In order to preserve the energy in the Fourier model and ensure the previous analysis done in this paper is still valid, the expectation of the Fourier coefficients must stay the same.

$$C_o(\vec{k})^2 = \langle |\widetilde{c}_o(\vec{k})|^2 \rangle \tag{2.65}$$

With the addition of random behavior, the Fourier coefficients are defined slightly differently

than in Eq. (2.35).

$$\widetilde{c}_o(\vec{k}) = N(0,1)Ae^{i\phi} \tag{2.66}$$

The distribution used is a Gaussian distribution with a mean of 0 and a standard deviation of 1. When Eq. (2.66) is plugged in to Eq. (2.65) the following equation is obtained.

$$C_o(\vec{k})^2 = \langle N(0,1)^2 A^2 \rangle \tag{2.67}$$

Conveniently, the expectation of a squared normal distribution is simply 1 so Eq. (2.67) reduces to $C_o(\vec{k})$ = A. In the end, the Fourier amplitudes are unchanged when averaged. The only difference in $\widetilde{c}_o(\vec{k})$ is the addition of the random amplitude scaling. Different, non-Gaussian, distributions can also be used to give the simulated waves slightly different shapes. If a different random distribution is used, the constant A may need to be calculated as it may not be equal to $C_o(\vec{k})$.

The other random variable encountered in this analysis is the initial phase of the Fourier components, ϕ. As opposed to the wave amplitude, which draws from a Gaussian distribution, the wave phase should be a random number in the range of 0 to 2π. There should be an even probability of obtaining any value within this range. From Eq. (2.66) it can be seen that negative draws from the distribution add a 180 degree phase shift. Since the initial phase is a uniformly distributed random variable, this has no overall effect. An ocean surface generated using random wave amplitude and phase is shown below with a grey scale image generated from another study included for reference. From a pure visual perspective, these images do not pass the eye test for 'looking' like an ocean surface. This is because when viewing the ocean, our eyes perceive light reflected off the ocean surface which is typically a function of slope. Visually appealing simulated ocean surfaces such as those seen in videogames or movies require an intricate shading procedure in addition to an ocean surface. For this analysis, this is not necessary. However, in order ensure the simulated ocean surfaces qualitatively are correct, a figure was created using a simple shader

based off x-direction surface slope.

Figure 2.3: Two simulated ocean surfaces colored according to surface height. On the left is a surface generated according to the analysis in this paper at a wind speed of 9 m/s. On the right is a surface generated in [26] using similar methods.

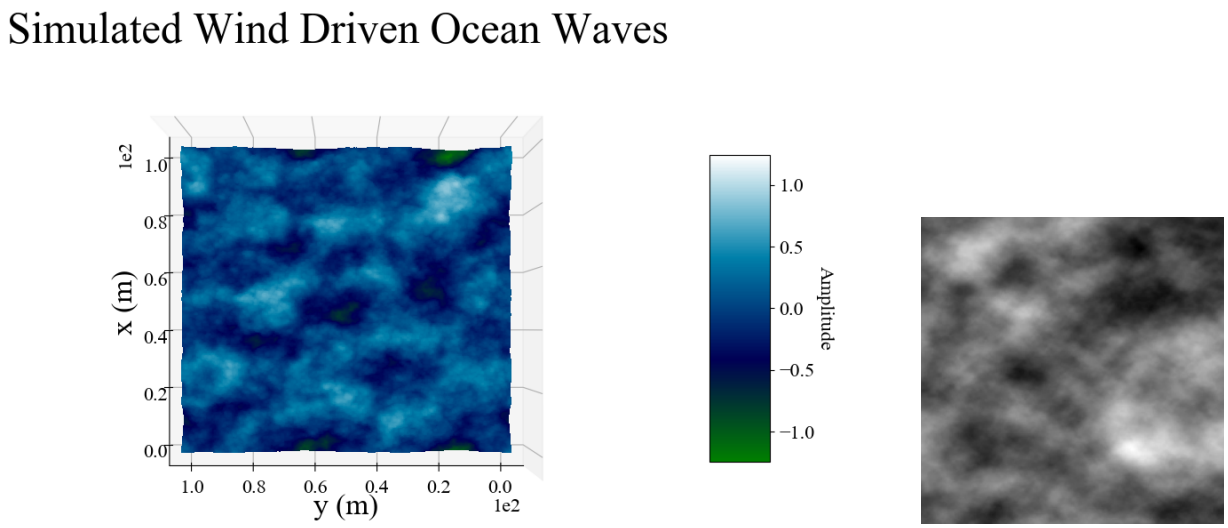

Figure 2.4: An ocean surface like those shown above however in this case the surface is colored according to slope to make for a more realistic visualization. A 20 meter long boat is included for reference.

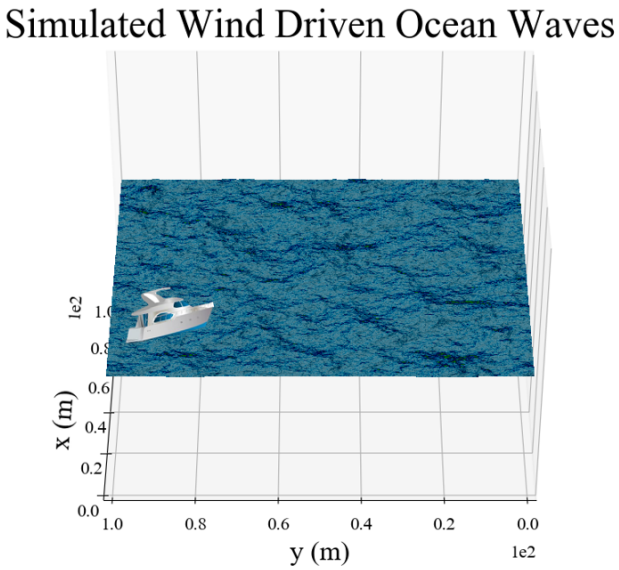

2.2.5 Simulation Constraints and Spectral Error

There are a variety of constraints and limitations which impact the ocean surface model, many of which are inherent in it's derivation. These were discussed earlier but are important to keep in mind. For example, the model relies on a flat, sufficiently deep sub-surface, a constant wind velocity, and waves large enough that surface tension can be ignored. The simulation is designed for modelling waves in the open ocean and in shallow waters close to shore, some changes occur. In very shallow waters, breaking waves will occur. These waves behave extremely differently than those considered in this thesis and as such, results from this model should not be applied to the breaking wave regime. If we move further offshore to waters outside the breaking wave regime, wave behavior changes slightly and waves become smaller, steeper, and more longitudinal. This can be accounted for by using a different theoretical spectral density and a different dispersion relation. This complicates the ocean model and is therefore not included in this study. Provided that breaking waves are not present in the vicinity of the ALB measurements, this model should still do a good job of representing the ocean surface.

As far as model implementation goes, computational expense is a significant limiting factor. High resolution simulations that accurately capture behavior on a scale ranging from kilometers to centimeters require near impossible computational resources. Unfortunately, it is necessary to be able to accurately portray this scale in order to create simulations that are correct and not just visually appealing. Due to computational constraints and time constraints, it was necessary to shrink the scale of the simulation. As a result, the errors incurred by doing this must be analyzed. Important to consider, are errors related to the variance of the surface height and the variance of the surface slope. Due to how the wavenumber arrays are initialized, the error in the surface height variance, or total spectral power is related to the expanse of the simulated grid. On the other hand, the error in the slope variance is related to the shortest wavelength that can be simulated. There is a trade off between these two errors that is constrained by computational expense. However, they are both essential to the accuracy of the model since the height variance governs the shape of the

simulated surface and the slope variance governs the effect of refraction on the lidar measurements. The total slope variance for an ocean surface as a function of wind speed is given by

$$\begin{aligned} \sigma_c^2 &= 0.003 + 1.92 \times 10^{-3} W \pm 0.002 \\ \sigma_u^2 &= 3.16 \times 10^{-3} W \pm 0.004 \\ \sigma_c^2 + \sigma_u^2 &= 0.003 + 5.12 \times 10^{-3} W \pm 0.004 \end{aligned} \tag{2.68}$$

where σ_c^2 is the slope variance in the cross-wind direction, σ_u^2 is the slope variance in the up-wind direction, $\sigma_c^2 + \sigma_u^2$ is the total slope variance, and W is the wind magnitude[33]. These equations for slope variance include the effect of capillary waves which add a significant amount of slope variance. Just for capillary waves, the slope variance is

$$\begin{aligned} \frac{\sigma_{cap,u}^2}{\sigma_{cap,c}^2} &= 2 \\ \sigma_{cap}^2 = \sigma_{cap,c}^2 + \sigma_{cap,u}^2 &= 0.000012 W^{2.1} ln\left(\frac{k^2}{2.5 \times 10^4} + 1\right) \end{aligned} \tag{2.69}$$

where k is the largest wavenumber simulated[34]. For capillary waves, this should extend to wavelengths on the scale of millimeters.

Just for the JONSWAP spectrum, the slope variance is given by[35]

$$\begin{aligned} \frac{\sigma_{J,c}^2}{\sigma_{J,u}^2} &= \frac{1}{0.9} \\ \sigma_J^2 = \sigma_{J,c}^2 + \sigma_{J,u}^2 &= 0.0033 + .0088 ln(W) + 0.00219 \left(ln\left(\frac{k^2}{k^2 + 100}\right) - ln\left(\frac{(6\pi)^2}{(6\pi)^2 + 100}\right)\right) \end{aligned} \tag{2.70}$$

By summing the JONSWAP and capillary variance and using a large value for k, one gets very close to Eq. (2.68). The capillary waves account for a significant portion of this variance and as such, they cannot be ignored. Since the simulation can't handle waves this small, capillary wave behavior is accounted for by adding a normal distribution with zero mean and variance determined

according to Eq. (2.69) to the local surface slope when calculated according to Eq. (2.30). Due to the miniscule amplitude of capillary waves, they are ignored when it comes to surface height calculations. Any error in the slope variance now comes from the JONSWAP spectrum and not using enough points to simulate a sufficiently small wavelength.

Below are plots of the error in the integrated power and in the total slope variance as a function of maximum and minimum wavelength respectively.

From the integrated power plot, it can be seen that it is important to maintain a large enough grid length or else the errors can quickly get out of control. In order to keep the error below 10-15%, the grid size should be set to 200 meters for wind speeds up to 10 m/s, 300 meters for wind speeds up to 12.5 m/s, and >400 meters for wind speeds greater than 15 m/s. However, to keep the error in the slope variance produced by the JONSWAP spectrum on the order of 10-15%, wavelengths at least as small as 10 cm must be captured. The combination of these requirements forced the grid size to be over 4096 points for all cases. For some wind speeds, a grid size of 16384 is required. Generally, for any grid size greater than 2048 the simulation takes well over a day to complete. To get around this, the grid length is selected such that the surface height variance error is below 10-15% and the missing slope variance is then manually added back in the same way the capillary wave variance is added. This solution is better than sacrificing grid length for the ability to simulate small wavelengths. The JONSWAP spectrum was designed to represent larger wavelengths and is not ideal when it comes to small wavelengths[36]. Furthermore, small scale behavior such as slope variance can be partially accounted for whereas large uncertainties in the total spectral power are guaranteed to yield erroneous results. Additionally, the missing slope variance can be attributed to wavelengths smaller than the lidar beam spot, which is approximately 1 meter in diameter on the surface, and since the correlation length of these waves is generally much smaller than the lidar beam, using a normal distribution to make up for their lost variance actually yields near identical results.

Figure 2.5: Error associated with numerical representation of ocean spectra. On the top is the error in the surface variance/integrated power spectral density as a function of the grid sized used for the simulation. On the bottom is the error in the slope variance of the surface as a function of the smallest wavelength simulated.

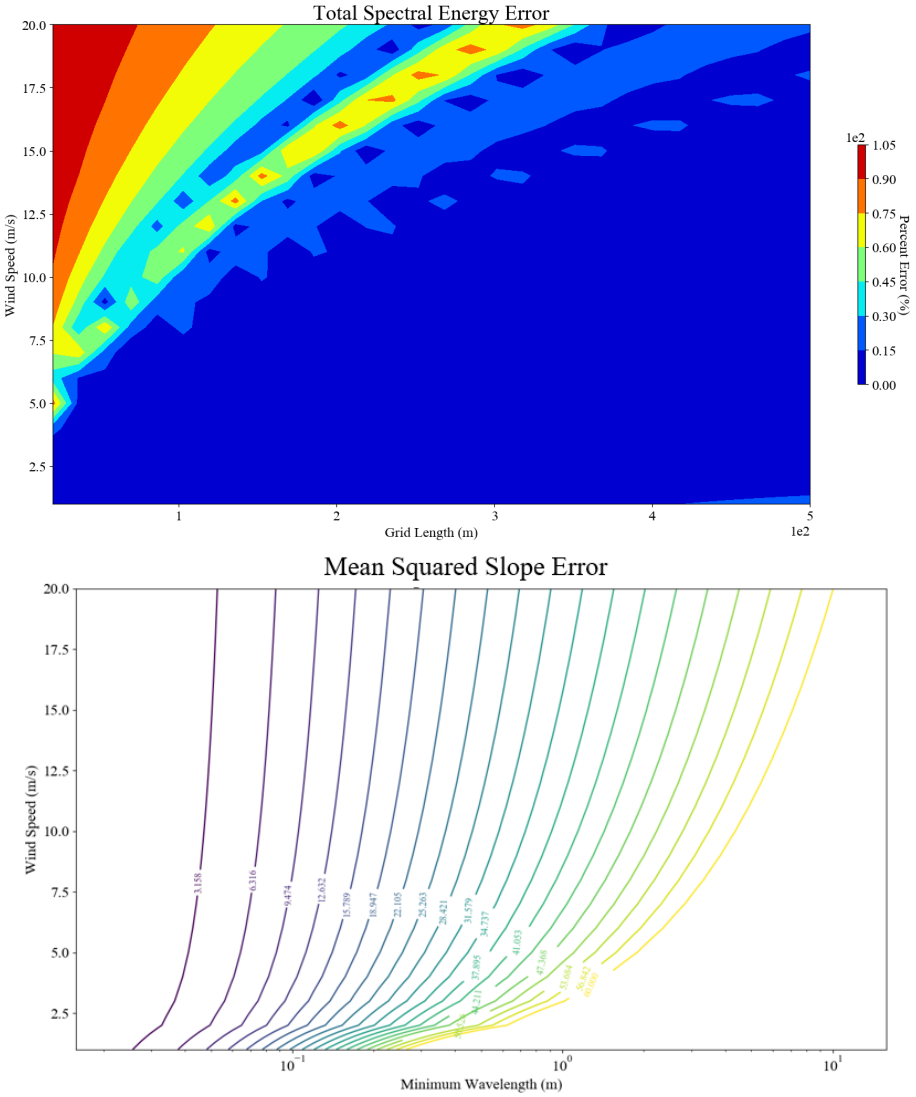

2.3 Lidar Simulation

The other side of this model is the lidar simulation. Once a realistic ocean surface has been generated, the lidar is simulated by approximating the beam as a set of rays and performing ray tracing until intersection with the ocean floor. Important to this portion of the simulation are

approximation of the beam, ray tracing and refraction, polarization, and treatment of reference frames. Lidars are complicated scientific instruments and the complexity of their models can vary greatly from laser physics, to physical optics, to embedded circuitry. This analysis ignores many of these characteristics for the sake of simplicity and so that the effect of the ocean surface on the received lidar signal can be better isolated.

2.3.1 The Lidar Beam

From a lidar model standpoint, one of the most valuable abilities of this model is the capability to represent the lidar beam as a volumetric entity as opposed to a single ray. By doing this, effects on the same scale as the lidar spot size can be modeled. Modeling the lidar beam is done by discretizing the beam as a collection of rays. Each ray represents a portion of the beam's solid angle and has a corresponding power attached. The power of each ray is calculated according to a Gaussian beam profile. The distribution of rays representing the beam are a set of points located on concentric circles within the beam however other distributions can be used. The direction of the rays is made so that their relative spacing is unchanged as they progress.

To start, the solid angle of each ray was determined by finding the area represented by each ray at a location far from the beam waist. For a radial distribution (concentric circle case), the area is dependent on which ray is being analyzed and is found by subtracting slices of two circles. The solid angle is then approximated according to the following formula.

$$\Omega_{SA} = \frac{Area}{r^2} \tag{2.71}$$

In this equation, the r is radius from the lidar source to the point at which the ray area's are calculated. As previously mentioned, this is simply an approximation for the solid angle. This approximation relies on the area in equation 2.71 being small in relation to the surface area of the sphere with radius r. This is universally true for our case given the small beam divergence modeled, which is on the order of milliradians.

Now that solid angle values have been calculated, the next step is to assign power to each

ray. The following formula describes the intensity of a Gaussian beam at some axial range down the beam and at some radial location out from the beam's axis[37].

$$I(z) = I_o\Big(\frac{w_o}{w(z)}\Big)^2 e^{\frac{-2r^2}{w(z)^2}} \tag{2.72}$$

The variables seen in this equation are as follows. I_o is the peak intensity at the beam waist, w_o is the beam waist radius, $w(z)$ is the radial point in the beam at which the intensity is $1/e^2$, r is the radial distance on the beam at which the intensity is evaluated, and z is the axial distance from the center of the beam. Many of these parameters are described with other equations. The equation for $w(z)$ is shown below[37].

$$w(z) = w_o\sqrt{1 + \Big(\frac{z}{z_R}\Big)} \tag{2.73}$$

In this equation, z_R is the Rayleigh range which can be found using Eq. (2.74)[37]

$$z_R = \frac{n\pi w_o^2}{\lambda} \tag{2.74}$$

where n is the index of refraction in the local media and λ is the wavelength of the laser light. As the axial distance increases to be far away from the beam waist, equation 2.73 can be approximated as $w_o\frac{z}{z_R}$ since z is much larger than z_R. It is apparent that w_o is an important parameter to be calculated for a Gaussian beam. In order to find w_o, knowledge of either the FWHM (full width half maximum) length of the beam or the beams divergence angle must be utilized.

$$w_o = \frac{FWHM}{\sqrt{2ln(2)}} \approx \frac{\lambda}{n\pi\theta} \tag{2.75}$$

At last, I_o is calculated according to Eq. (2.76). This equation is based off the total integral of the intensity profile at any axial distance being equivalent to the pulse power (P_o).

$$I_o = \frac{2P_o}{\pi w_o^2} \tag{2.76}$$

In order to determine the power of a ray according to this profile, the area represented by the ray should be multiplied by the intensity distribution of the ray at the proper distance. With the formulas above accounted for, the power of any ray can be found by multiplying equation 2.72 by area and then simplifying so that the end result is in terms of solid angle (equation 2.77).

$$P(z) = (\Omega_{SA} I_o)(z_R)^2 e^{\frac{-2r^2}{w(z)^2}} \tag{2.77}$$

An interesting consequence of expressing the power distribution in this form is that when external effects, such as atmospheric attenuation, are ignored, the power of each ray is invariant with respect to range. Therefore, the power of each ray can be treated as a constant as the rays are propagated forward. These rays maintain their relative spacing as one moves along the beam and therefore accurately approximate the beam's power and shape at any distance from the lidar. In order to determine how the simulated surface affects the beam, these rays are traced through the surface as described in the next section.

2.3.2 Ray Tracing and Refraction

A fundamental component of the lidar simulation is the ray tracing done in order to model the light path, starting with emission at the lidar source and ending at the receiver. The ray tracing process involves propagation of the rays until intersection with the water surface, changed direction of the rays due to refraction, propagation of the rays until intersection with a submerged planar "ocean floor", and then propagation of the rays back to the lidar receiver.

The first step in the ray tracing is to propagate each ray until intersection is achieved with the water surface. Although it is possible to determine the height of the surface at any x-y location, the analytical description of the surface shape is prohibitively complicated and as such, the ray intersection with the surface cannot be immediately determined. To get around this, the sea-surface is assumed to be flat and planar at the nominal sea-surface altitude. The rays are propagated until intersection with this flat surface using a vectorized equation for intersection with a plane (equation

2.78 and 2.79).

$$t = \frac{\hat{n}_{ocean} \cdot (\vec{p}_{ocean} - \vec{p}_{lidar})}{\hat{n}_{ocean} \cdot \hat{n}_{lidar}} \tag{2.78}$$

$$\vec{p_f} = t\hat{n}_{lidar} + \vec{p}_{lidar} \tag{2.79}$$

In these equations, $\hat{n}$ is the direction unit vector for either the lidar rays or for the ocean normal. In this case, the ocean is assumed to be flat so the normal vector points solely in the z direction. Additionally, $\vec{p}$ is position vector for either the start of each lidar ray or for the center of the ocean surface plane. Eq. (2.79) propagates each ray by the correct distance to find the position of intersection ($\vec{p_f}$). Once the position of intersection on the flat ocean surface has been found for each ray, the ocean height at the x-y point of intersection is determined using the equations described in the ocean surface model section. The normal of the surface is also determined. For non-nadir rays, adding waves will result in a slightly altered ray direction since the estimated point of direction for each ray did not include wave height. This effect is inherent to this method yet can be accounted for by simply adjusting the ray direction and initial location to match propagation from the beam waist to the new point of sea-surface intersection. It should be noted that the initial ray location is generally not the beam waist since there may be precursory propagation of the beam within the lidar before the beam exits. For this model, the point at which the beam exits the system is what is defined as the lidar origin/initial position.

Upon reaching the sea-surface, each ray undergoes refraction. Afterwards, the ray location is unchanged however the direction vector is altered. The first step in calculating the direction vector after refraction is to set up a coordinate system located on the ocean surface. A visualization of this coordinate can be seen in Fig. (2.6).

Figure 2.6: The coordinate system attached to the ocean surface used for refraction calculations. The basis vector for this system are shown in orange. Also shown is the unit vector for the surface normal and the lidar beam normal.

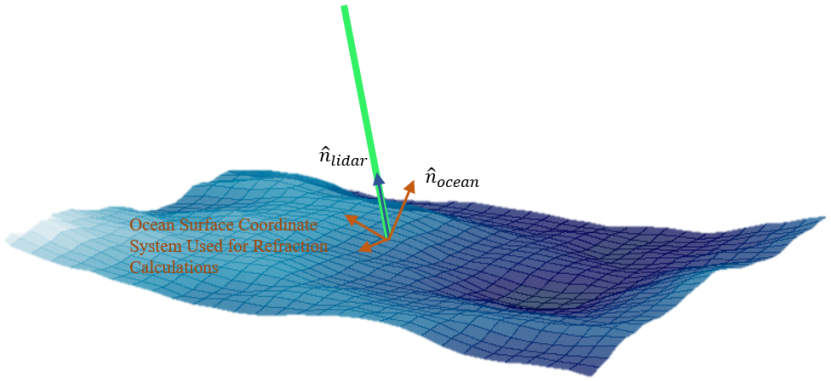

To assemble this coordinate system, the cross product is taken between the ocean normal vector and the incoming ray direction vector. This result is normalized giving one of the basis vectors for this coordinate system. Next, the cross product is taken between this new basis vector and the original ocean normal vector. This, along with the ocean normal vector make an orthogonal basis attached to the ocean surface. The incident lidar direction vector lies in the plane defined by two of these vectors (the ocean normal and the final calculated basis vector). According to Snell's law, the angle of the output ray is dependent on the input angle and the indices of refraction of the two media. Snell's law was stated earlier in Eq. (1.2. The indices of refraction for air and water are known as 1.00029 and 1.33 approximately, so only the incident angle remains to be determined. This is done using a dot product between the ray direction vector and the ocean normal. After using Snell's law to determine the angle of refraction, the output direction vector can be assembled using the basis vectors which comprise the plane of incidence. These vectors are simply scaled and added such that they make the correct angle with the surface normal. From here, equations 2.78 and 2.79 can be used once again to propagate the ray until intersection with a planar surface meant to represent the ocean floor.

For the returning lidar rays, both returns off the ocean surface and returns from a sub-

surface scatterer are considered. The first and most simple return path is the specular reflection off the water surface. This path requires much less analysis since refraction is not important and polarization is preserved. Additionally, it can be assumed that, if a specular reflection is detected by the lidar, the ray has taken the same path back to the receiver. Specular lidar returns are dependent on small scale surface roughness creating surface facets orientated normal to the incident beam. The magnitude of this reflection is dependent on the number and size of such oriented facets. This phenomenon, known as glint, has been the focus of several past studies and is not discussed further in this thesis. The main takeaway for the specular reflection is that under most circumstances, a reflection off the ocean surface is seen by the lidar. For the diffuse reflection off the ocean floor this isn't necessarily true. Due to the wavy nature of the ocean surface, it is possible for there to be multiple different paths that lead back through the water surface to the lidar receiver. This effect is ignored in this model and propagation along the return path is simplified by assuming the rays return to the receiver along the path of transmission. For a coaligned or nearly coaligned receiver and transmitter, this is generally a valid assumption[21]. The reasoning behind making this simplification is mainly related to the added complexity that would be forced upon the ray-tracing model. This comes from the fact that simulating the many possible paths of diffuse scattering would require us to split each ray into countless secondary rays at the ocean floor. These numerous secondary rays would then have to be re-propagated through the surface. The computational expense of this analysis is simply too great seeing as this would have to be done for each of the many primary rays. Additionally, very few of the secondary rays would return to the receiver and we already know that a return ray following the initial path will be received. Even though the only return ray analyzed is the one that follows the initial path, the power loss from a diffuse reflection is accounted for. This is done by treating the floor as a Lambertian scatterer and assuming the return ray solid angle is equivalent to that subtended by the receiver area. A more in depth discussion of power losses along the lidar path will occur in the polarization and power section.

2.3.3 Polarization and Power

Although not all ALB systems utilize polarization, polarization is a key component for the system (INPHAMIS 1) that this work was directed towards[13]. Even for lidars that are not reliant on polarization, the transmitted beam is typically highly polarized and the amount of return power can be polarization dependent. In order to see how the ocean surface affects the lidar polarization, Mueller matrices are used to describe various aspects of the ray path. Mueller matrices operate on a Stoke's vector and are meant to represent physical effects that affect polarization. These 4x4 matrices can express effects such as polarization dependent attenuation, depolarization, or polarization dependent phase shifts.

The equation used to analyze power and polarization effects along the lidar path is the Stoke's vector lidar equation[27]. This equation consists of a chain of Mueller matrices which together describe each step in a lidar measurement.

$$\vec{S}_{RX}(R) = \boldsymbol{M_{RX}}[(G(R)\frac{A}{R^2}\Delta R)\boldsymbol{T_{atm}}(\vec{k}_s, R)\boldsymbol{F}(\vec{k}_i, \vec{k}_s, R)\boldsymbol{T_{atm}}(\vec{k}_i, R)\boldsymbol{M_{TX}}\vec{S}_{TX} + \vec{S}_B] \tag{2.80}$$

The Stoke's vector lidar equation in this form is meant to describe general polarization effects on a lidar measurement in air. The various terms in this equation are as follows: $\vec{S}_{RX}(R)$ represents the Stokes vector received by the system as a function of range, $\boldsymbol{M_{RX}}$ represents a Mueller matrix that describes the receiver, G(R) is a function to describe the receiver/beam overlap, A represents the area of the receiver aperture, R represents the range, ΔR is the range bin length, $\vec{k}_i$ and $\vec{k}_s$ represent the direction of propagation as the beam propagates outward and then returns respectively, $\boldsymbol{T_{atm}}$ is a Mueller matrix that describes the effects of transmission through the atmosphere, $\boldsymbol{F}$ describes the scattering off the target surface, $\boldsymbol{M_{TX}}$ is the Mueller matrix for the transmitter, $\vec{S}_{TX}$ is the transmission Stokes vector, and $\vec{S}_B$ is the noise. For the model described in this thesis, $\vec{S}_{TX}$ is always the Stokes vector for perfectly linearly polarized light where S0 and S1 equal 1 and S2 and S3 equal 0.

For usage with bathymetry, several modifications must be made to Eq. (2.80) in order to

capture the effect of the water surface and transmission through the water column. Therefore, terms must be added on either side of the back-scattering matrix, $\boldsymbol{F}$, which describe rotation into the S-P polarization reference frame, Fresnel reflectivity and transmission, and water column attenuation.

$$\begin{aligned}\vec{S}_{RX}(R) &= \boldsymbol{M_{RX}}[(G(R)\Omega_{SA}\Delta R)\boldsymbol{T_{atm}}(\vec{k}_s,R)\boldsymbol{R^{L}_{sp}}(\theta)\boldsymbol{T_w}(\vec{k}_s,R)\boldsymbol{T_{wa}}(\vec{k}_s,R) \\ &\quad \boldsymbol{F}(\vec{k}_i,\vec{k}_s,R)\boldsymbol{T_w}(\vec{k}_i,R)\boldsymbol{T_{aw}}(\vec{k}_s,R)\boldsymbol{R^{sp}_{L}}(\theta)\boldsymbol{T_{atm}}(\vec{k}_i,R)\boldsymbol{M_{TX}}\vec{S}_{TX}+\vec{S}_B]\end{aligned} \tag{2.81}$$

The added terms are $\boldsymbol{R^{sp}_{L}}(\theta)$ and $\boldsymbol{R^{L}_{sp}}(\theta)$ which describe rotation of the transmitted lidar Stoke's vector into a polarization frame with axes parallel and perpendicular to the plane of incidence (the s-p frame) and back to the original lidar frame, $\boldsymbol{T_{aw}}$ and $\boldsymbol{T_{wa}}$ which describe the Fresnel transmission through the water surface, $\boldsymbol{T_w}$ which describe the effect of transmission through the water column, and Ω_{SA} which is the solid angle subtended by the receiver, adjusted for refraction. Originally the solid angle could be approximated according to Eq. (2.71) with the area term being the area of the receiver aperture. When refraction is considered, this changes. By viewing the solid angle as a cone, the angular width of the solid angle can be found under the assumption of no refraction.

$$\phi_{air} = cos^{-1}\left(1-\frac{\Omega}{2\pi}\right) = cos^{-1}\left(1-\frac{A}{2\pi R^2}\right) \tag{2.82}$$

Since the receiver area is small in comparison to the distance to the ocean floor, ϕ_{air} can be assumed as small. The change in this angle can therefore be calculated by taking the derivative of Snell's law and by applying the small angle approximation.

$$\begin{aligned} n_1 cos(\theta_i)d\theta_i &= n_2 cos(\theta_r)d\theta_r \\ n_1 cos(\theta_i)\phi_{air} &= n_2 cos(\theta_r)\phi_{water}\end{aligned} \tag{2.83}$$

Using this equation in conjunction with Eq. (2.82), the correct receiver solid angle can be

Figure 2.7: A visualization of how refraction changes the solid angle of the receiver.

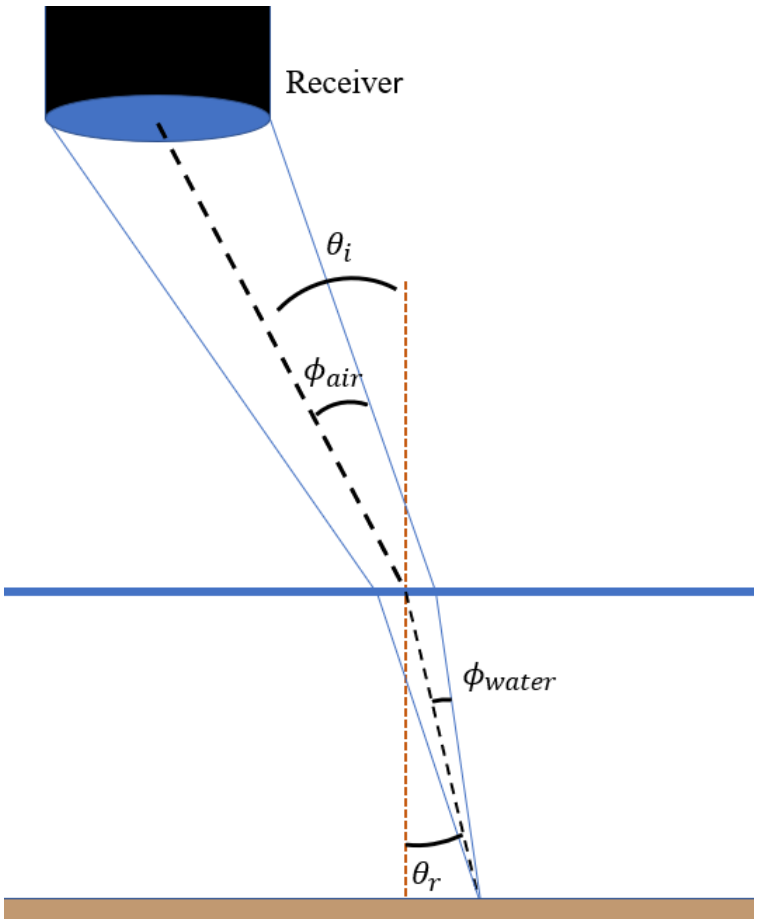

determined.

$$\Omega_{SA} = 2\pi(1 - cos(\phi_{water})) \tag{2.84}$$

When used in the lidar-ocean model, Eq. (2.82) is applied to each ray in the lidar beam. Several simplifications are made to Eq. (2.82) for implementation in the ocean-lidar model. For one, lidar returns from volume scattering in the atmosphere or water column are ignored. Therefore, the only scattering matrices, $\boldsymbol{F}$, used are those related to the specular water surface and the ocean floor. Since these are hard targets, their response should not be integrated over a full range bin and as such, ΔR can be dropped. Additionally, the background noise term, $\vec{S}_B$ is ignored so that the ocean surface effects can be better isolated. The receiver and transmitter Mueller matrices are

also simplified as identity matrices. This assumes that there are no polarization dependent optics in the receiver and transmitter. In general, the transmitter will have a polarizing filter and/or a phase-shifting half wave plate. Since the effect of these components will be lost, they can be accounted for simply by setting the transmitted Stoke's vector to that measured at the output of the lidar system. Similarly, optics within the receiver will not properly modelled. $\vec{S}_{RX}$ therefore gives the Stoke's vector for the light at the entrance of the receiver aperture. In order to obtain the polarization state of the light at the lidar detector, $\vec{S}_{RX}$ must be subsequently multiplied by a Mueller matrix for the detector. For the INPHAMIS system, there are two polarization dependent detector channels so the Stoke's vector at each channel can be found by using different $\boldsymbol{M_{RX}}$ expressions after finding $\vec{S}_{RX}$. The last simplification made is with regards to the receiver beam overlap function, G(R). It is assumed that there is always full overlap between the beam and the receiver field of view which is generally true for the ocean surface and floor with a properly designed bathymetric lidar.

The important Mueller matrices which must be calculated are then: $\boldsymbol{T_{atm}}$, $\boldsymbol{R_L^{sp}}(\theta)$ and $\boldsymbol{R_{sp}^L}(\theta)$, $\boldsymbol{T_{aw}}$ and $\boldsymbol{T_{wa}}$, $\boldsymbol{T_w}$, and $\boldsymbol{F}$. First, the formula for $\boldsymbol{T_{atm}}$ is given. For atmospheric transmission, only Rayleigh scattering is considered. Attenuation by Rayleigh scattering is mostly polarization maintaining so $\boldsymbol{T_{atm}}$ can be assumed to be an identity matrix multiplied by an attenuation coefficient[38].

$$\boldsymbol{T_{atm}} = A \begin{bmatrix} 1 & 0 & 0 & 0 \\ 0 & 1 & 0 & 0 \\ 0 & 0 & 1 & 0 \\ 0 & 0 & 0 & 1 \end{bmatrix} \tag{2.85}$$

The attenuation coefficient, A, in this equation is determined according to Beer's law.

$$A = e^{-\int_0^R \alpha(r)dr} \tag{2.86}$$

This equation relies on the integral of the atmospheric extinction coefficient over range. This coeffi-

cient is dependent on pressure and temperature which are functions of altitude for the atmosphere. The extinction coefficient for Rayleigh scattering can then be given as a function of r as shown below.

$$\alpha(r) = 1.5859 \times 10^{-33} \lambda^{-4.0117} \frac{P(r)}{T(r)} \tag{2.87}$$

Here, P(r) and T(r) are the pressure and temperature in Pascals and in Kelvin respectively. These quantities can be found using atmospheric models allowing for easy calculation of A through numerical integration.

The interaction of the lidar beam with the ocean surface is described using the following two terms. As discussed above, the polarization of the lidar must be expressed in a frame with axes parallel and perpendicular to the plane of incidence in order for the Fresnel Mueller matrices to be used. This is known as the S-P frame, where S polarization corresponds to electric field oscillations perpendicular to the water surface normal and P polarization corresponds to oscillations in the plane of incidence. Conversion into the S-P polarization frame is done using a Mueller transformation matrix. The angle θ in this matrix is the angle between the P polarization axis and the horizontal polarization axis for the lidar. This angle can be calculated using transformation matrices by creating a lidar coordinate frame and an S-P coordinate frame and then finding the rotation about the z-axis needed for converting between the two. In literature, the S-P frame required for use of the Fresnel Mueller matrices is defined with an upwards pointing z-axis[39]. To account for this, after transforming into the coordinate frame obtained from the rotation shown below, the z and y axis' should be inverted. The Stokes vector of the lidar can be expressed in this new frame with the following Mueller matrix.

$$\boldsymbol{R}(\theta) = \begin{bmatrix} 1 & 0 & 0 & 0 \\ 0 & cos(2\theta) & -sin(2\theta) & 0 \\ 0 & sin(2\theta) & cos(2\theta) & 0 \\ 0 & 0 & 0 & 1 \end{bmatrix} \tag{2.88}$$

Once in the correct frame, the Mueller matrices for Fresnel reflection and transmission for transition between media 1 and media 2 are used. The formulas for these are shown below[39].

$$\boldsymbol{R}_{12} = \begin{bmatrix} \alpha+\eta & \alpha-\eta & 0 & 0 \\ \alpha-\eta & \alpha+\eta & 0 & 0 \\ 0 & 0 & \gamma & 0 \\ 0 & 0 & 0 & \gamma \end{bmatrix} \tag{2.89}$$

$$\alpha = \frac{1}{2}\left[\frac{tan(\theta_i - \theta_t)}{tan(\theta_i + \theta_t)}\right]^2 \tag{2.90}$$

$$\eta = \frac{1}{2}\left[\frac{sin(\theta_i - \theta_t)}{sin(\theta_i + \theta_t)}\right]^2 \tag{2.91}$$

$$\gamma = -\frac{tan(\theta_i - \theta_t)sin(\theta_i - \theta_t)}{tan(\theta_i + \theta_t)sin(\theta_i + \theta_t)} \tag{2.92}$$

For normal incidence, we have divide by zero cases for the terms in the reflection matrix. This is an important case for our purposes since the lidar water surface returns are assumed to be specular reflections. For normal incidence specular reflections, the reflection Mueller matrix is

$$\boldsymbol{R}_{spec} = \left(\frac{n_2 - n_1}{n_2 + n_1}\right)^2 \begin{bmatrix} 1 & 0 & 0 & 0 \\ 0 & 1 & 0 & 0 \\ 0 & 0 & -1 & 0 \\ 0 & 0 & 0 & -1 \end{bmatrix} \tag{2.93}$$

Specular reflections, which occur at normal incidence are assumed to be the only surface returns that reach the receiver however it is rare for normal incidence to occur with the simulated rays. The specularly reflected light that returns to the system generally occurs due to ocean roughness on a scale smaller than can be represented with the collection of rays representing the lidar beam. These small scale specular reflections are known as glint and have been the subject of several studies. Since the simulation is not capable of functioning on this scale, it is assumed that glint occurs for each

ray and a scaling factor is added to control how much glint occurs. An improvement that could be added which would better capture glint behavior would be to change this scaling factor depending on slope and wind conditions.

For general transmission from media 1 to media 2, the following equations are used[39]:

$$\boldsymbol{T}_{12} = \kappa \begin{bmatrix} \alpha' + \eta' & \alpha' - \eta' & 0 & 0 \\ \alpha' - \eta' & \alpha' + \eta' & 0 & 0 \\ 0 & 0 & \gamma' & 0 \\ 0 & 0 & 0 & \gamma' \end{bmatrix} \tag{2.94}$$

$$\alpha' = \frac{1}{2}\left[\frac{2sin(\theta_t)cos(\theta_i)}{sin(\theta_i + \theta_t)cos(\theta_i - \theta_t)}\right]^2 \tag{2.95}$$

$$\eta' = \frac{1}{2}\left[\frac{2sin(\theta_t)cos(\theta_i)}{sin(\theta_i + \theta_t)}\right]^2 \tag{2.96}$$

$$\gamma' = \frac{4sin^2(\theta_t)cos^2(\theta_i)}{sin^2(\theta_i + \theta_t)cos(\theta_i - \theta_t)} \tag{2.97}$$

$$\kappa = \frac{n_2 cos(\theta_t)}{n_1 cos(\theta_i)} \tag{2.98}$$

Again, there is a special case for normal incidence. In this scenario, the transmission coefficient can be obtained from the knowledge that the sum of the reflection and transmission coefficients must be 1.

$$\boldsymbol{T}_{spec} = \left(1 - \left(\frac{n_2 - n_1}{n_2 + n_1}\right)^2\right) \begin{bmatrix} 1 & 0 & 0 & 0 \\ 0 & 1 & 0 & 0 \\ 0 & 0 & 1 & 0 \\ 0 & 0 & 0 & 1 \end{bmatrix} \tag{2.99}$$

These formulas are complicated and their effect is not intuitive. It is however apparent that the ocean surface can easily affect the polarization of the light, even for unpolarized incident light.

An extreme example of this is for incidence at the Brewster angle. At this angle, the P polarized light is perfectly transmitted resulting in a polarized reflection.

After transmission through the water surface, attenuation by the water column is experienced. This attenuation takes a form similar to the atmospheric attenuation. Unlike with the atmospheric attenuation, the extinction coefficient for water is assumed to not be dependent on range.

$$\boldsymbol{T_w} = e^{-\alpha_w R} \begin{bmatrix} 1 & 0 & 0 & 0 \\ 0 & 1 & 0 & 0 \\ 0 & 0 & 1 & 0 \\ 0 & 0 & 0 & 1 \end{bmatrix} \tag{2.100}$$

The extinction coefficient for water depends on water conditions[40].

$$\alpha_w = \begin{cases} 0.151 & \text{for clear waters} \\ 0.398 & \text{for coastal waters} \\ 2.19 & \text{for turbid waters} \end{cases} \tag{2.101}$$

The final interaction that needs to be represented with a Mueller matrix is depolarization from the diffuse scattering off the ocean floor. Depending on the ocean floor, this matrix could take a variety of shapes. For this model, a depolarization matrix for randomly orientated scatterers is used[41]. This matrix allows for the representation of a partially depolarizing subsurface scatterer. The parameter d in this equation is a measure of how much the scattering medium depolarizes incident light. For complete depolarization, d should be set to 1. In the lidar-ocean model, d is set to be .7 meaning the floor is mostly depolarizing. The parameter β, governs the reflectivity of the ocean floor. This constant was chosen to equal .4. The optical behavior of the ocean floor can vary greatly and is not a focus for this study. As such, it should be understood that these constants are

simply rudimentary estimates.

$$\boldsymbol{F} = \beta \begin{bmatrix} 1 & 0 & 0 & 0 \\ 0 & 1-d & 0 & 0 \\ 0 & 0 & d-1 & 0 \\ 0 & 0 & 0 & 2d-1 \end{bmatrix} \tag{2.102}$$

2.3.4 Reference Frames

The treatment of reference frames is critical to this simulation especially as we seek to simulate an aircraft mounted lidar. There are many different reference frames that need to be considered. These are the lidar reference frame (in which the polarization is defined), the aircraft reference frame (in which position and attitude information are defined), the global reference frame, the local ocean surface reference frame (in which refraction is defined), and the S-P reference frame (in which Fresnel reflection and transmission are defined). The main tool used for analysis of reference frames are transformation and rotation matrices along with Euler angles.

In order to convert coordinates from some body frame to an inertial frame where the body frame's orientation is described using yaw, pitch, and roll Euler angles, the following transformation matrices are used. Here, ψ, θ, and Φ, are the yaw, pitch, and roll angles respectively.

$$\vec{X}_I = \boldsymbol{T}_B^I \vec{X}_B \tag{2.103}$$

$$\boldsymbol{T}_B^I = \boldsymbol{R}_y(\psi)\boldsymbol{R}_p(\theta)\boldsymbol{R}_r(\Phi) \tag{2.104}$$

$$\boldsymbol{R}_y(\psi) = \begin{bmatrix} cos(\psi) & -sin(\psi) & 0 \\ sin(\psi) & cos(\psi) & 0 \\ 0 & 0 & 1 \end{bmatrix} \tag{2.105}$$

$$\boldsymbol{R}_p(\theta) = \begin{bmatrix} cos(\theta) & 0 & sin(\theta) \\ 0 & 1 & 0 \\ -sin(\theta) & 0 & cos(\theta) \end{bmatrix} \tag{2.106}$$

$$\boldsymbol{R}_r(\Phi) = \begin{bmatrix} 1 & 0 & 0 \\ 0 & cos(\Phi) & -sin(\Phi) \\ 0 & sin(\Phi) & cos(\Phi) \end{bmatrix} \tag{2.107}$$

The first reference frame considered is the lidar reference frame. This is the frame attached to the lidar that would be used when working in a laboratory setting. The z-axis points along the direction of the center of the lidar beam. This is the reference frame in which the polarization of the lidar should be defined. For airborne lidar bathymetry, the lidar is rigidly mounted to the aircraft and the orientation of this mounting must be measured so that the lidar measurement can be referenced to the aircraft.

The next reference frame considered is the aircraft reference frame. This is the classical reference frame used when working with aircraft and has the x-axis directed along the aircraft fuselage, the y-axis situated along the wings, and the z-axis pointing downwards such that a right hand coordinate system is completed. Conversion between this reference frame and the lidar frame is done with a transformation matrix developed with the lidar mounting Euler angles. In the aircraft frame, arrays of yaw, pitch and roll measurements can be input in order to simulate aircraft motion. Additionally, the aircraft center position can be changed. It is assumed that the aircraft position is equivalent to the lidar position. In reality, a lever arm from the lidar to the aircraft GPS must be considered.

The global reference frame is the next considered. This reference frame relates all others to a frame based off East, North, and up. In this frame, East is the x-axis, North is the y-axis, and up is the z-axis. The aircraft is expressed in this frame by describing the orientation in a North-East-Down frame depending on the current aircraft Euler angles. This is then translated to the global frame using a rotation matrix with a yaw of -90 degrees and a pitch of 180 degrees.

In order to properly model refraction, a coordinate system attached to the ocean surface, that is also tangential to the surface, is required. This reference frame was covered in the ray tracing section. It is determined by taking the cross product between ocean normal and the ray direction vector, creating an orthogonal coordinate system consisting of, the ocean normal vector (pointing upward), a vector tangential to both the ray direction and the ocean normal, and a third vector that lies within the plane defined by the ocean normal and the ray direction. The incident ray can be decomposed in this frame and then reassembled after it's components are altered by refraction.

The final reference frame is similar to the one previously described however, in this case, the lidar direction vector forms part of the basis. This frame is needed for converting the polarization from the lidar frame to one aligned with the S-P frame as dictated by the ocean slope. For the first basis vector, the cross product between the ray direction vector and the ocean normal is used. The final basis vector is then found by crossing the basis vector just found with the lidar z-axis vector. This coordinate system has a z-axis closely aligned to that of the lidar frame when expressed in global coordinates. The main difference is that this system is rotated so that it's x and y axis' correspond to P and S polarizations in the plane of incidence. The polarization, initially defined in the lidar frame, can be converted to this frame as dictated in the previous section once the angle required to convert between the two frames has been found. The rotation required comes from determining the transformation matrix that relates the lidar frame to this S-P frame and then calculating the yaw that this transformation represents. The equations used for extraction of this angle are shown below.

$$\boldsymbol{T}_L^{sp} = (\boldsymbol{T}_{sp}^{ENU})^{-1}\, \boldsymbol{T}_L^{ENU} \tag{2.108}$$

$$\chi = tan^{-1}\left(\frac{\boldsymbol{T}_{21}}{\boldsymbol{T}_{11}}\right) \tag{2.109}$$

An illustration of the different frames encountered in the model is shown below in Fig. (4.1). Although the amount of reference frames required for this model may seem complicated,

Figure 2.8: The different reference frames utilized in the lidar-ocean model.

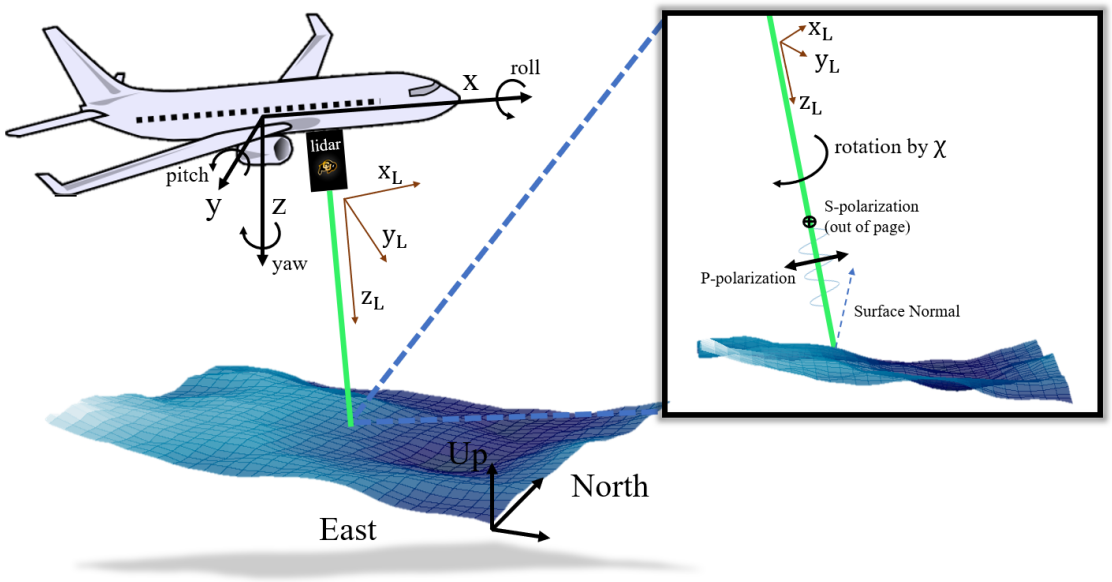

converting between the various frames actually becomes quite easy when transformation matrices are used. Once the basis vectors or Euler angles describing a frame are known, it is easy to construct a transformation matrix linking vectors between two frames. Additionally, these matrices can be linked in order to convert between any of the frames with ease. There are advantages associated with analysis in each frame so it is important to be able to transition between the frames. The "main" reference frame used, in which all final analysis is done, is the lidar frame as this best represents how the behavior simulated in this model affects the lidar system. However the primary frame for visualization and for ocean surface modeling with the lidar excluded is the global, East-North-Up frame.

Chapter 3

Model Results

The model described in the previous sections is capable of producing a wide variety of different types of results. There are seemingly endless different parameters and inputs which can be varied and studied. For this thesis, we seek to answer how a wavy water surface affects airborne lidar bathymetry measurements and ocean surface detection. Additionally, what conditions limit lidar's capabilities for use in the presence of a wavy water surface? For a single lidar measurement, how much uncertainty does the water surface add in regards to range errors and horizontal coordinate error? For many measurements taken over a long period of time, what is the surface's effect and can the lidar measurements be used to obtain information about the ocean? To better understand these questions, the lidar-ocean model is used to estimate the distributions of lidar measurements in this environment. The conditions which will be the focus of this analysis are changing wind speeds and variation in the lidar off-nadir pointing angle.

To start, a plot is created which shows the lidar beam, the wave surface, and the refracted rays. This plot does a great job of illustrating what is happening in the simulation however it does not provide much quantitative information.

3.1 Return Signal Distributions

For both the ocean surface returns and ocean floor returns, the bundle of rays which make up the lidar beam are traced from the lidar transmitter back to the receiver according to the methods described in the previous chapter. The time of flight for each of these rays is determined

Figure 3.1: Model visualization. For this scene, the wind is set to 7 meters per second and the lidar is given a pitch angle of 10 degrees.

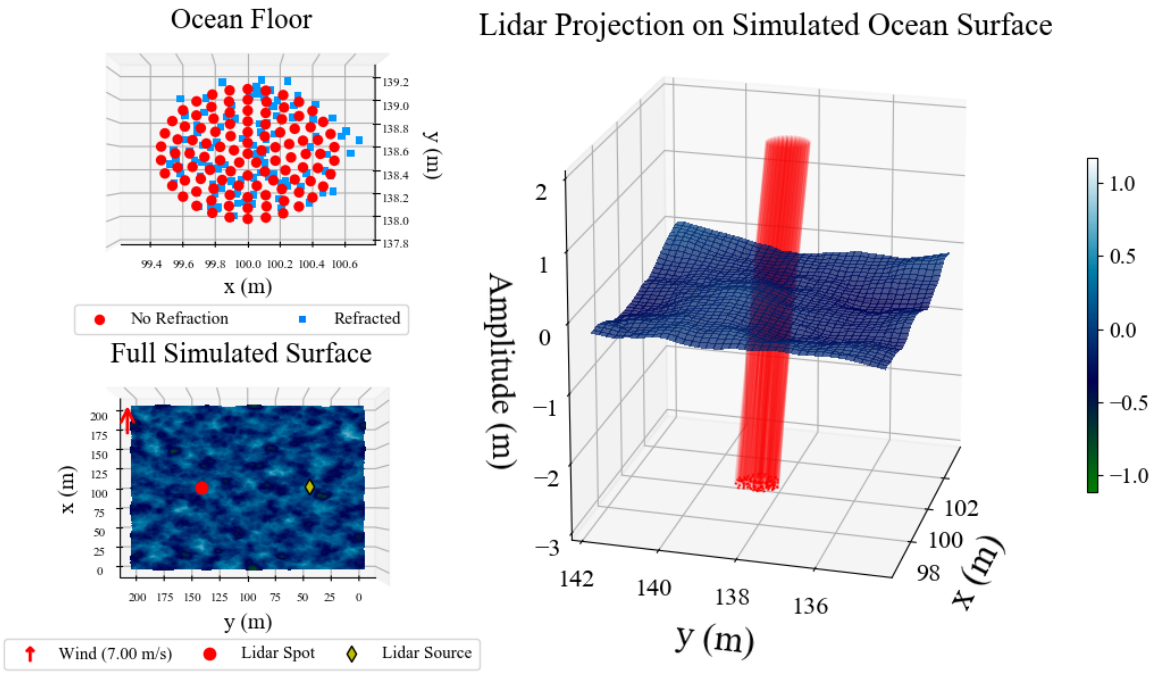

based off the distance they travelled and the speed of light, in both air and water, in order to best represent signal seen by a real lidar. The INPHAMIS 1 system records these times by binning photon detections in 27 picosecond time bins. To best approximate this effect, the power from the received rays is also binned according to 27 picosecond intervals. Elevation changes on the ocean surface caused by waves make it so rays in different parts of the beam return at different times. This results in a shaped surface response that is related to the uncertainty in a single surface detection. The same goes for the floor response, however, the distribution of floor returns is affected by refraction in addition to surface height elevation changes. Many factors can affect these distributions such as wave size, slope, and direction. In order to isolate these effects, the laser pulse width and lidar receiver impulse function have been ignored. Additionally, the impulse response of the ocean surface or floor for a single ray interaction has been simplified as a delta function.

Specifically, wave scale can have an enormous effect on the lidar distributions and it is im-

portant to understand how different wave scales can have different effects on the lidar. For the surface signal, waves that are much greater in size than the lidar beam act as a flat slanted surface and spread the distribution. Waves that are of similar size to the lidar spot are more unpredictable in their effect and often times create bimodal distributions. Waves that are smaller than the lidar beam do not significantly affect the surface distribution besides adding some slight spread. For the floor signal, large wave will result in uniform refraction throughout the beam. The beam structure will be preserved and all the rays will be identically deflected. Wave structures on the same order as the lidar spot size will cause different refractive effects throughout the beam spot. This leads to a deflection and focusing or defocusing of the beam. Since the correlation length of these waves is similar to the beam size, the beam structure will be distorted but not destroyed. For the floor response, waves that are smaller than the lidar beam can be very significant. These waves randomly scatter the beam causing spread and destruction of beam structure.

Below are some different examples of single shot distributions that can occur. The variability of these distributions is important to note. For the plots shown below the wind was kept fixed at 8 m/s, the depth was set to 3 meters, and the lidar was pointed nadir. A wind speed of 8 m/s will be used for many simulations going forward since many effects can be witnessed at this wind speed. 8 m/s is also a very common wind velocity over the open ocean and the surface conditions that result from this speed are well representative of a typical ocean surface. These plots, obtained at a single wind speed, demonstrate all the different possible wave effects. Both the surface and floor distributions are shown. The nominal line in the floor distributions corresponds to the detection time that would be seen by the lidar if the ocean surface were flat at the point of ray intersection. A slanted surface response can be seen in Fig. (3.2). This response is evenly spread around the nominal time for the surface return signal. For the floor signal, many of the rays are deflected in the same direction resulting in a bias in the response. The middle figure, Fig. (3.3), shows the effect of waves that are sized similarly to the beam spot. The surface distribution is irregular and bimodal. Focusing is the main effect seen in this floor response, as is expected for waves with curvature on the same scale as the lidar beam. The focusing occurs at the center of the beam and therefore

the distribution is narrowed. At last, in Fig. (3.4), the effect of a mostly flat surface with waves smaller than the lidar footprint can be seen. There is little effect on the surface response besides minor spreading. The floor response for small waves is also shown here. As expected, the small waves spread the rays for this measurement creating a wider distribution. The wave surface shape for each of these plots was verified visually by plotting the ocean surface in the region local to the lidar beam.

Figure 3.2: The surface and floor response obtained at 8 m/s wind speed. The red line marks the return time of the center of the beam. The effect of a slanted surface can be seen

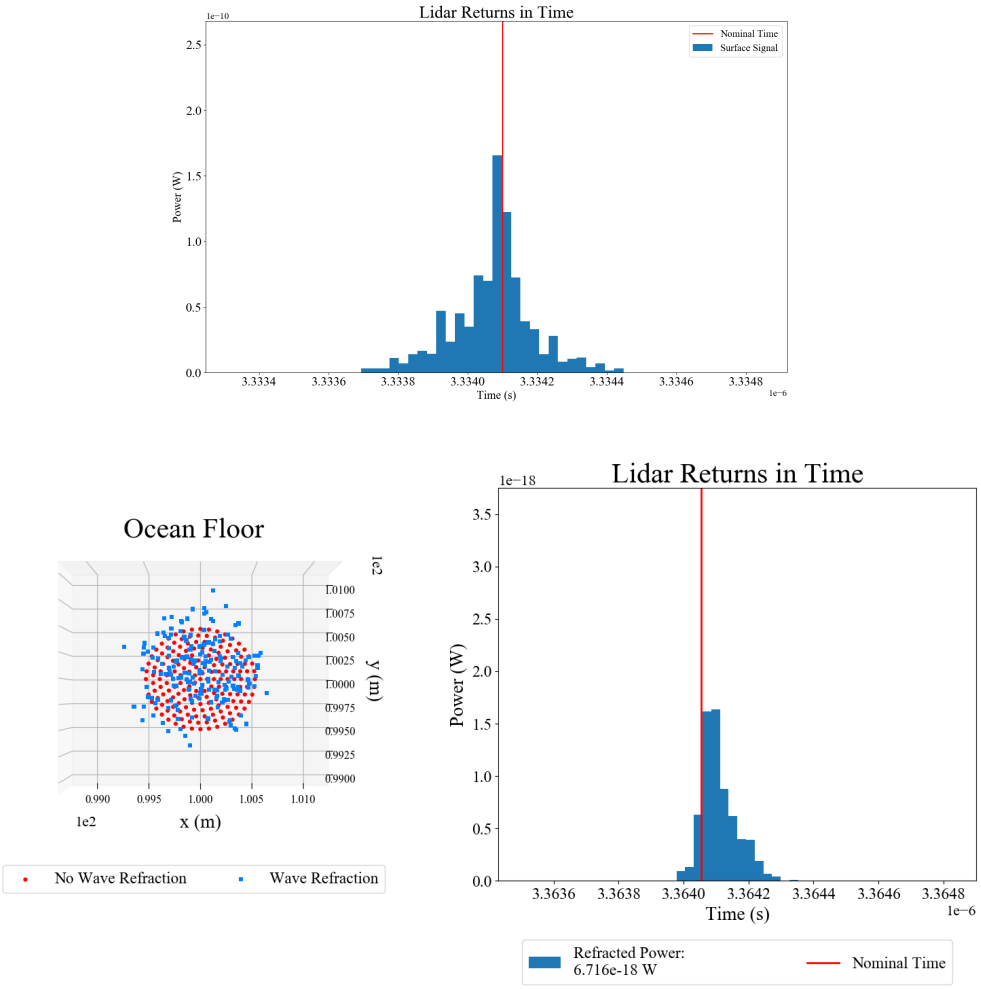

For multiple lidar measurements, a similar idea can be applied. If the lidar records ocean

Figure 3.3: Surface and floor response from a simulation with the same conditions as Fig. (3.2). However, in this case a bimodal effect can be seen.

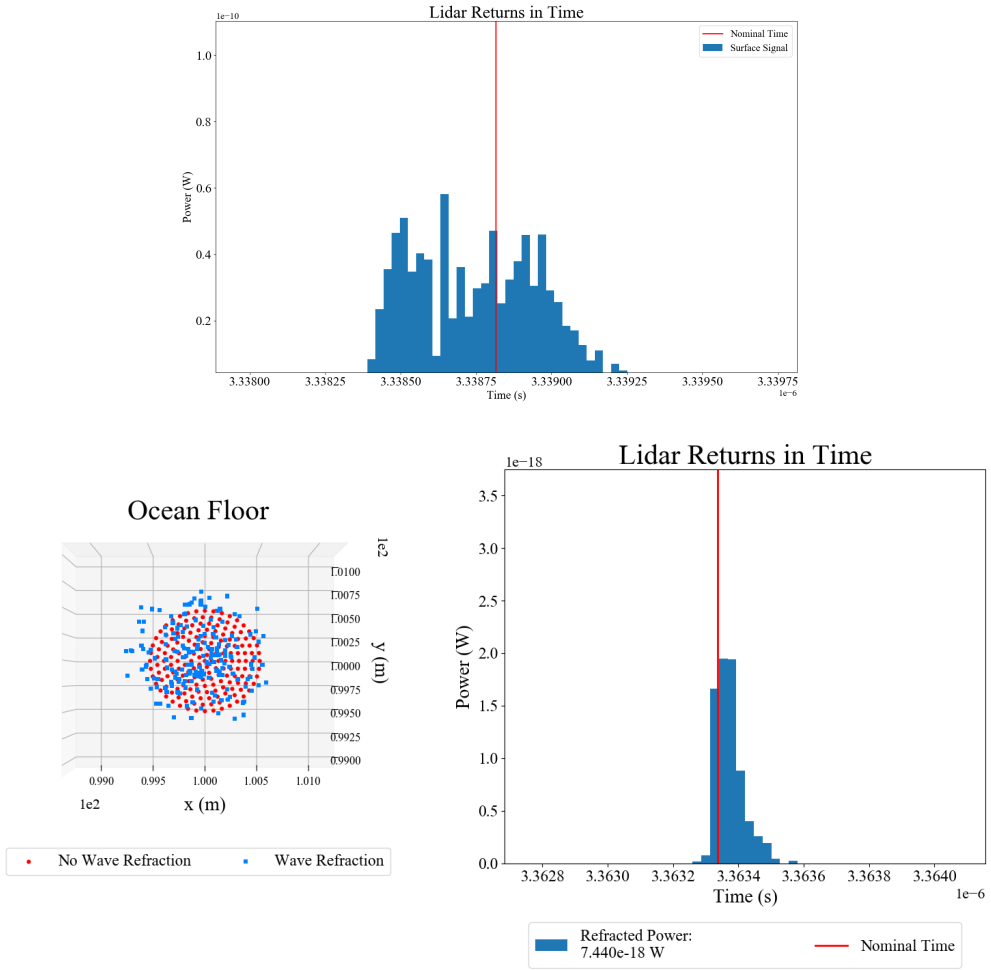

wave height measurements for a long period of time, another, much wider distribution will be formed. The variance of this distribution will relate to the sea surface variance and the mean will relate to the mean sea level. In comparison to satellite radar systems which have a spot size large enough to capture many wave cycles, the lidar spot size is usually smaller than wavelength of the ocean waves. The variance in a single radar measurement is representative of the surface variance whereas the variance in a single lidar wave measurement is often more similar to that seen when pointed at a flat, sloped target[34]. The total surface variance is an important quantity for ocean

Figure 3.4: Surface and floor response with conditions identical to the previous two figures. However, here the effect of a mostly flat surface can be seen.

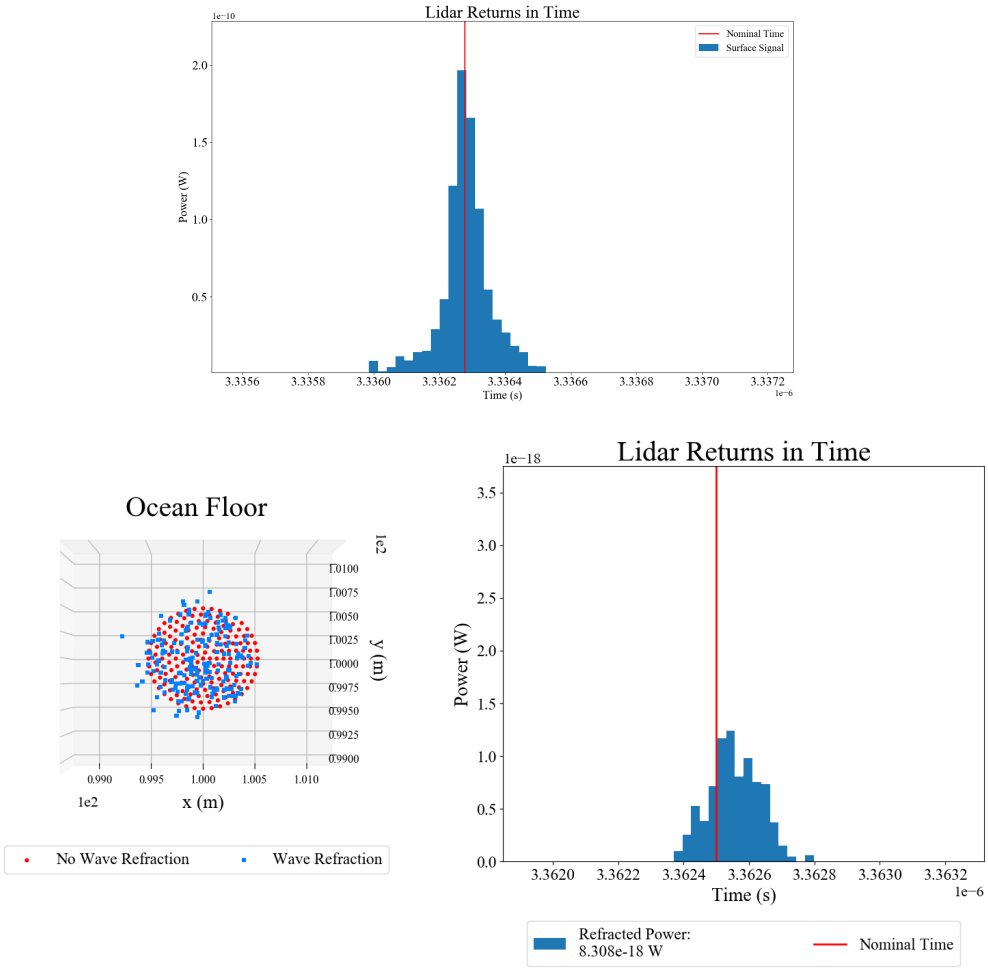

wave sensing as it provides a means for determining significant wave height and wind speed. A lidar obtains this measurement by first mapping the ocean wave structure and then calculating the variance of the recorded point cloud. The single shot surface distribution will be convolved into this measurement and will dictate the uncertainty associated with each surface detection[42]. For decreasing wave size, waves begin to have an effect on the same scale as the lidar beam spot. The single shot variance broadens and begins to approach the total surface variance. Eventually when waves are smaller than the lidar spot, the same effect as observed with radar is obtained and the

variance on a single lidar measurement is equivalent to the total surface variance. This effect is not modeled in this thesis since the ocean model is not designed to simulate such low wind speeds.

The floor signal also exhibits interesting behavior when viewed over many measurements. Since the floor signal is dependent on the amount of time spent in the water, the variance is strongly related to the surface signal. This relationship dwarfs the effects that control the single-shot floor response. Like the surface distribution for multiple shots, the floor distribution can be used to obtain information related to the ocean environment. Since the variance of the floor response is strongly correlated with the surface response any discrepancies between these two indicate that the subsurface roughness is of comparable scale to the sea surface.

3.1.1 Wave Height and Depth Distributions

In the context of a real lidar measurement, heights and depths are the desired quantities as opposed to surface and floor times. The surface and floor times, t_s and t_f, can be converted into ranges using the speed of light and the index of the local media, however, if refraction or off nadir pointing is involved further analysis must be conducted. A diagram of the parameters that must be considered is shown in Fig. (3.5). The surface height and depth can be calculated based off the surface and floor distributions for a single measurement. The height is dependent on the aircraft position, lidar pointing angle, and recorded time. The depth is dependent on the lidar pointing angle, and difference between the two responses. The horizontal coordinate error is related to deflection of the beam and spreading of the beam. As shown in Fig. (3.5), deflection of the beam causes the error dh. Additionally, horizontal coordinate uncertainty is caused by the width of the beam.

Calculation of the ocean height when the aircraft altitude is known is simple for this model since the aircraft position is known. In a real system, this process is much more difficult and will be discussed in the next chapter. Given the surface detection times, the wave height is found according

Figure 3.5: The different ranges involved with an ALB measurement. The range to the surface is r_1. The range from the surface to the floor without knowledge of the wave slope (this assumes the surface is flat) is r_2. The true range from the surface to the floor is $r_2^{'}$. The difference between the horizontal position of the surface detection and floor detection is h. Given an off-nadir angle, this can be estimated by once again assuming the surface is flat. In reality, refraction changes this to $h^{'}$. The horizontal position error is therefore dh.

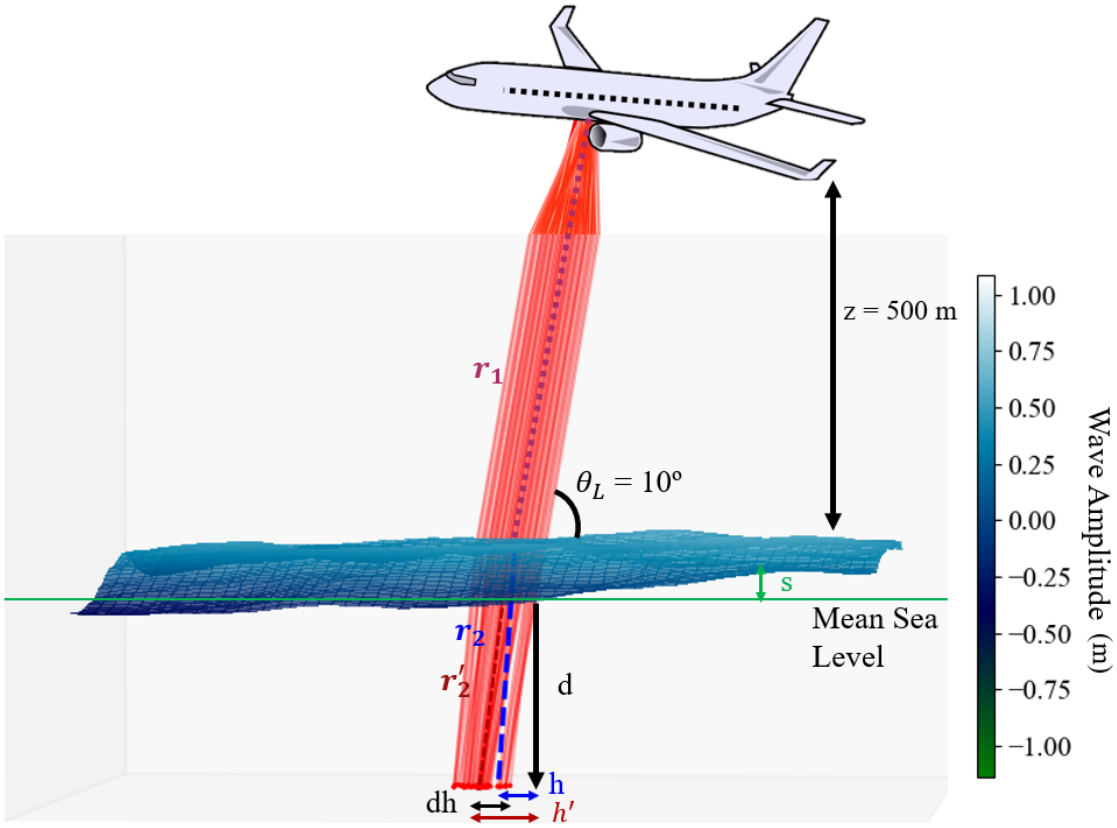

to

$$s = z - \frac{ct_s cos(\theta_L)}{2n_1} \tag{3.1}$$

where s is the wave height, z is the aircraft altitude, t_s is the surface detection time, c is the speed of light, and n_1 is the index of refraction of the first media (air). If the aircraft altitude is assumed to be known with certainty, the distribution of surface times directly translates into a distribution around the measured wave height.

The determination of the depth is more complicated due to the fact that two distributions

must be subtracted. If these distributions are thought of as probability distributions that describe random variables, the difference between them can be determined from probability theory. Since the surface slope isn't known, it must be assumed to be flat so that the angle of refraction can be calculated. Once the angle of refraction is known, r_2 can be used to determine d.

$$\begin{aligned} r_2 &= \frac{c(t_f - t_s)}{2n_2} \\ \theta_r &= sin^{-1}\left(\frac{n_1}{n_2} sin(\theta_L)\right) \\ d &= r_2 cos(\theta_r) \end{aligned} \tag{3.2}$$

Since t_s and t_f are being treated as random variables, their difference is also a random variable.

$$\begin{aligned} t_s &\sim X \\ t_f &\sim Y \\ Z &= Y - X \end{aligned} \tag{3.3}$$

According to probability theory, Z, as a difference between two random variables, is found by taking the discrete cross-correlation of their distributions.

$$(x \star y)[n] = \sum_{m=-\infty}^{\infty} x[m]y[m+n] \tag{3.4}$$

After performing this operation, the depth can be determined with Eq. (3.2). By performing a cross-correlation, both the surface and floor response contribute to the depth measurement. This alters the variance of the determined depth and causes the distribution to take more of a bell shaped form. One would think that this should increase the variance of the depth distribution however due to correlation between the surface and floor response, this isn't necessarily the case.

The single-shot wave height and depth distributions are shown below in Fig. (3.6). It should be noted that by single-shot, we mean a lidar measurement taken over a time scale so small that

the ocean can be assumed as stationary. Since the laser for most lidar systems pulses at at least several kilohertz, it is very possible that multiple detections could be received in a short enough time to be characterized by this "single-shot" distribution.

Again, the wind speed for this simulation was 8 m/s. These plots are representative of the uncertainty produced by the ocean surface for a single lidar measurement given the stated sea surface conditions. For both distributions the sea surface adds about 10 centimeters of uncertainty. This imposes a limit on the lidar's ability to resolve surface wave structure and to resolve subsurface objects in range. Additionally, for the depth measurement there is an offset between the location of the mean of the distribution and the actual depth at this location. The source of this offset can be seen from Fig. (3.5). The signal recorded off the floor by the lidar corresponds to $r_2^{'}$. Since the wave structure isn't known, refraction is assumed to occur along r_2 leading us to erroneously attribute the signal returns from $r_2^{'}$ to r_2. This often times will lead to an overestimation of depth although it is possible for refraction to cause an underestimation.

Another important measurement error which must be considered is the horizontal error, dh, as can be seen in Fig. (3.5). This error can be attributed to any combination of refraction, beam spread, the beam spot size, and beam focusing. There are two ways by which this horizontal uncertainty can be analyzed. To investigate how the ocean surface adds to this horizontal uncertainty we use the power profile of the lidar rays in the plane of the ocean floor to calculated a weighted beam centroid. This centroid can then be compared to the unperturbed beam center to better understand how effects such as refraction and focusing change the beam's underwater profile. In the ocean plane, the intensity of the rays can be binned to estimate the beam power profile after interaction with the wave surface. For the 8 m/s wind speed models, the beam centroid error is typically less than 10 centimeters however this changes when the wind speed and lidar pointing angle are varied.

The horizontal uncertainty can also be measured by determining the distance from each ray to the beam centroid. The power of the rays can then be binned according to these distances so that a distribution of energy as a function of distance from the lidar is obtained. While the centroid

Figure 3.6: Lidar wave height and depth single-shot distributions. The depth distribution is on the top. It can be seen that there is a bias towards a large depth. The surface distribution is on the bottom. This distribution is nearly identical to the surface response at this time.

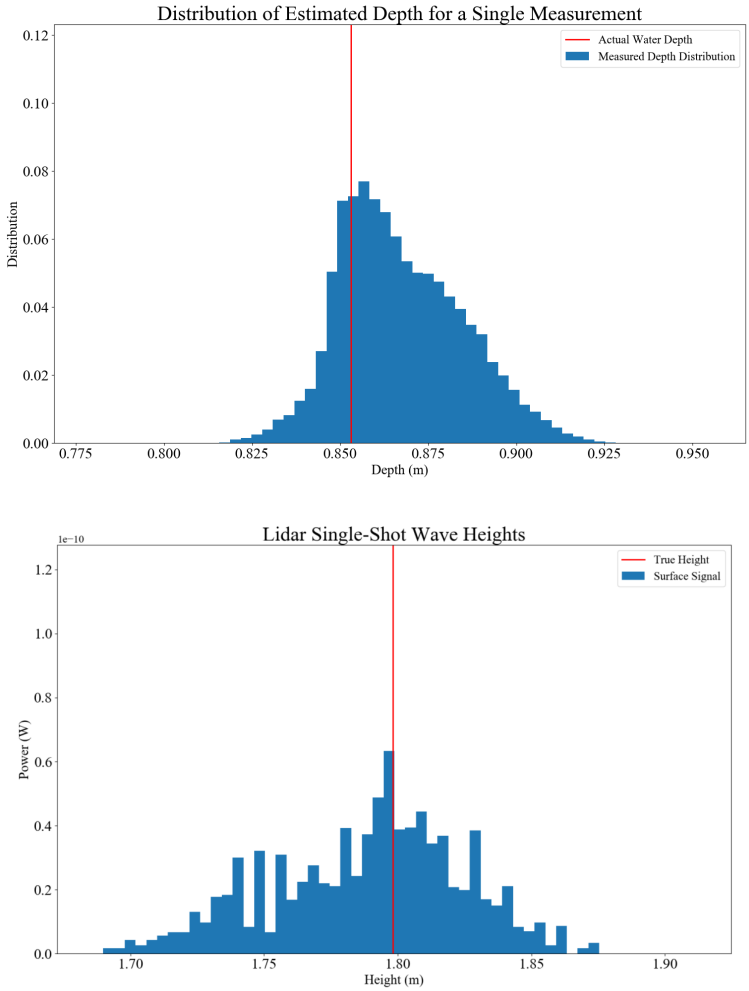

method is better for answering questions related to beam deflection and refraction, this method is well suited for analyzing beam spread. Due to the size of the lidar footprint, this method will always yield a somewhat significant spread. Nonetheless, it is important to consider this spread even if it is caused by the ocean lidar footprint as opposed to the ocean surface. This energy spread is an important source of uncertainty and is a limiting factor for the lidar's spatial resolution. A distribution for this horizontal spread is shown in terms of x difference and y difference. The

Figure 3.7: Beam power profile at the ocean floor. A combination of refraction and focusing moved the centroid off-center.

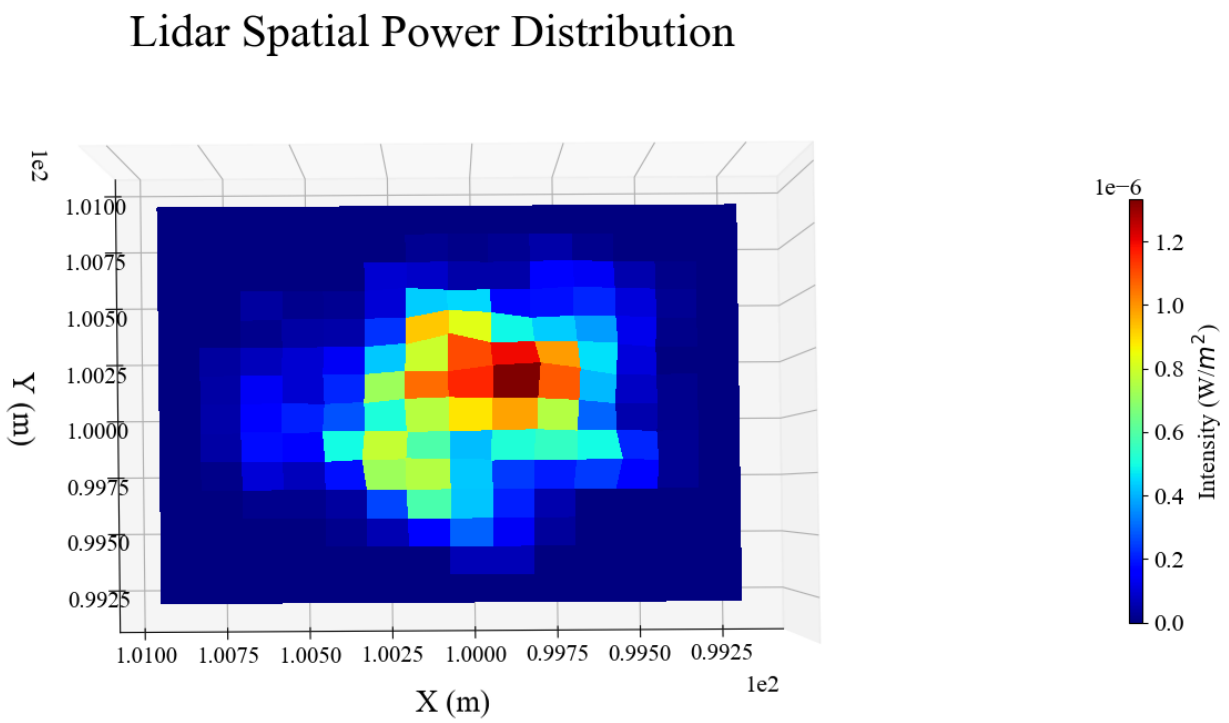

variance of these two distributions can be used to estimate the standard deviation for the horizontal error due to spread.

The depth and surface distributions obtained for multiple shots have also been calculated. The surface height and depth distributions obtained over multiple shots contain several useful quantities. For the surface height distribution, taking the mean yields the mean sea level while the variance gives significant wave height. On the other hand, the mean of the depth distribution gives the average water depth whereas the variance contains information about the subsurface roughness. Multiple shot distributions collected over 80 seconds and obtained at 8 m/s wind speed are shown below in Fig, (3.9).

As expected, the width of these distributions is much larger than with the single lidar measurement distributions. The behavior seen in these plots is also more irregular and sporadic. This is likely due to the narrowness of the surface response in regards to the total surface response.

Figure 3.8: Energy spread of rays in lidar beam at the ocean subsurface. The spread is centered on the centroid. Both the spread in the x direction and the y direction are shown.

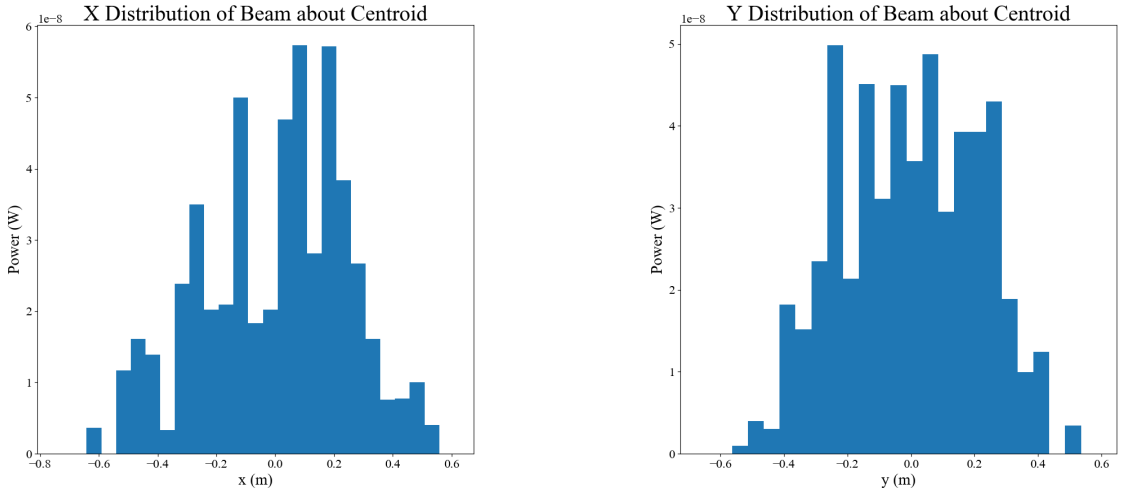

When the single-shot response is superimposed on the waves, the single-shot distribution manifests as peaks in the total distribution. When a shorter simulation length is used, this "spiky" behavior becomes exaggerated. To solve this, lidar data should be simulated for a longer period of time, at a smaller time interval. Unfortunately, simulating a larger number of lidar points with good temporal resolution is a time consuming process for the simulation. This brings up a constraint that must be considered when using a real lidar to build up a distribution like that shown in Fig. (3.9). The lidar data must be collected over a long enough time or over enough wave cycles so that a distribution representative of the sea state can be built.

The statistics for the distributions in Fig. (3.9) are fortunately only slightly affected by the imperfect shape of the distributions. The expectation of the measured depth is 3.008 meters and the variance is .215 meters. For the surface signal, the expectation of the ocean surface height is .0003 meters, and the variance is still .21. The expected variance for the simulated wind speed (8 m/s) was found to be .181 by integration of the JONSWAP spectrum. The means of these distributions are extremely close to their expected values. This indicates that lidars can accurately measure average depth and mean sea level in the presence of ocean waves.

Figure 3.9: Distributions of lidar data taken above a wavy surface with wind blowing at 8 m/s. The data was collected over 80 seconds.

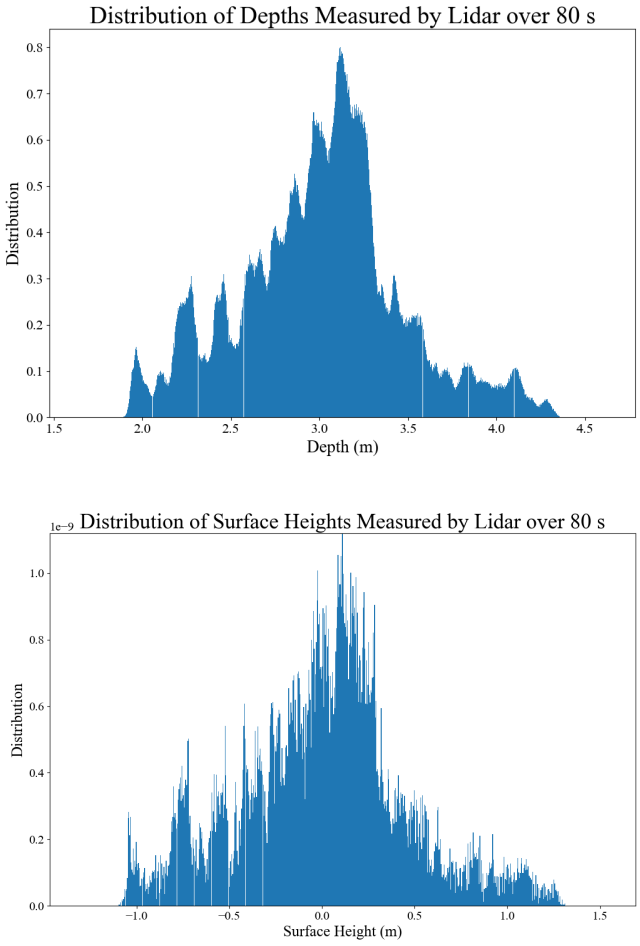

The discrepancy in variance could be attributed to several different factors. By tweaking JONSWAP parameters, a variance of .21 at a wind speed of 8 m/s can be easily obtained. Furthermore, due to the random nature of the spectral amplitudes for the simulated surface and error in the surface height variance due to the grid size selection shown in Fig. (2.5), the actual surface variance can differ from that expected by the JONSWAP spectrum by about 10 %. A measured variance of .21 for the given conditions is certainly reasonable. Additionally, the variance may be overstated in the simulated distribution due to the spikiness in the distribution caused by not using

enough lidar data. Considering the range of valid variance values, a variance of .21 as measured by the lidar is acceptable and shows the variance of the lidar data can be used to determine ocean surface variance.

As can be seen from comparing the surface height and depth response, the depth is highly dependent on the surface distribution. The effect of the single-shot distribution is dwarfed by sea surface distribution and is barely noticeable. Due to the close relationship between the surface height distribution for multiple shots and the depth distribution for multiple shots, significant discrepancies between that two can be used to detect surface floor elevation changes. For the model described in this research, the sea floor is assumed perfectly flat so this effect is not observed. It is nonetheless an interesting characteristic which could possibly be utilized with an ALB system.

3.2 Wind Speed Variation

It is likely that the most significant input to the ocean model is the wind speed. The wind speed governs the amplitude, speed, length, and shape of the simulated ocean waves. Since the sea state is so heavily dependent on wind speed, it is important to investigate how different wind speeds and different sea states affect the lidar measurements and the lidar distributions introduced in the previous section. For this analysis, the wind speed is varied between 0 m/s and 14 m/s in increments of 2 m/s. The wind is set to be blowing in the x-direction and the lidar off-nadir angle is set as 0 degrees. First, the single shot statistics are analyzed. The average single shot standard deviation and the offset between the distribution mean and true height/depth are plotted. Additionally, the minimum and maximum for these quantities is shown to demonstrate the possible range of behavior for the single-shot distribution at each wind speed. The horizontal error statistics are also presented. For the centroid error, the mean deviation and max deviation of the beam centroid from the nominal center are plotted. For the beam spread error, the mean x, y, and total standard deviations for the refracted beam spot are plotted along with max of the total standard deviation. This shows how different wind speeds affect the horizontal error for the average situation and for the worst case situation. For the multiple shot distributions, the variance and mean are calculated

for each wind speed to better understand how wind speed affects the lidar's ability to measure quantities such as ocean height variance, mean sea level, and mean depth.

The target questions for this section are, can statistics be applied to the lidar returns such that wind speed can calculated? Also, how do varied sea surface conditions affect ALB data and limit the technique?

3.2.1 Wind Speed Variation for Single-Shot

The single-shot distribution was obtained by simulating lidar surface height and depth measurements over 50 seconds. At each simulated time, a single-shot distribution was created and the variance and mean were saved. The offset in the mean of the distribution with respect to the true surface height or water depth was then determined to study any biases in the single-shot distributions. The mean of both the single-shot variance and offset was taken for all 50 seconds worth of distributions to determine the average single shot response as a function of wind speed. Although these distributions vary greatly on a per-shot basis, by averaging their characteristics some general trends can be observed. The range of different behavior exhibited by these distributions on a per shot basis can also be seen by looking at the minimum and maximum variance and offset at each wind speed. For these plots, the variance was converted to standard deviation since standard deviation better relates to uncertainty. These results are shown below in Fig. (3.10).

For the standard deviation plot, it can be seen that, unsurprisingly, the uncertainty of the distributions increases with wind speed. For all wind speeds, the uncertainty associated with a single surface height or water depth measurement is typically on the order of a couple centimeters. The change in the standard deviation of the single shot distribution starts at zero, as is expected, and then quickly grows. After the wind speed reaches about 6 m/s, this growth begins to level off. Between 6 m/s and 14 m/s only about a centimeter of standard deviation is added for the average distribution. Fig. (3.10) therefore implies that for wind speeds greater than 6 m/s, the uncertainty on the average single measurement does not change greatly. The minimum and maximum standard deviations also follow this general trend. However, it can be seen from Fig. (3.10) that as wind

Figure 3.10: Average distribution parameters for the single-shot distributions plotted against wind speed.

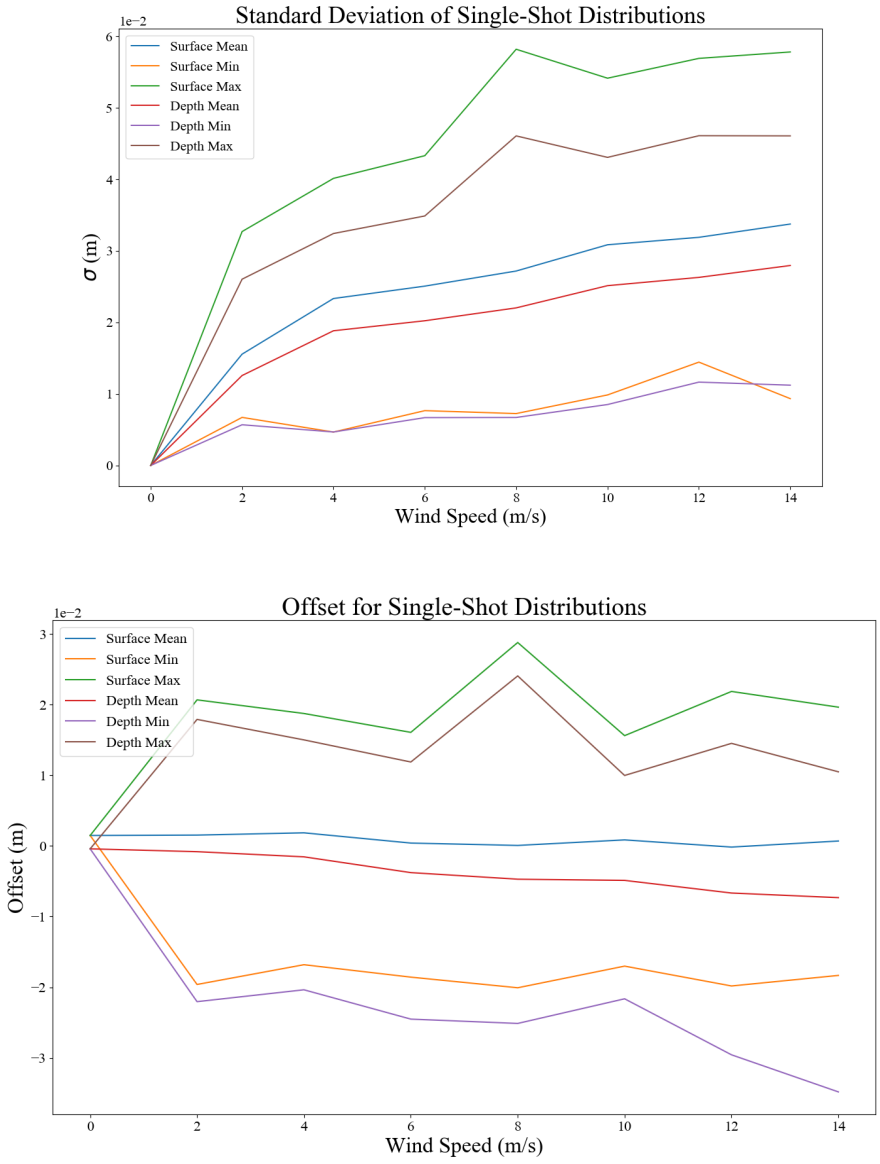

speed increases, the range in possible behavior for these distributions increases significantly.

At high wind speeds, the standard deviation on a single measurement could be as large as 6 cm for the surface measurement and 5 cm for the depth measurement. On the other hand, these standard deviations could be as low as a single centimeter. Depending on the lidar, these

uncertainties will affect the quality of the lidar data with varying severeness. For example, the ranging uncertainty for the INPHAMIS system is 1 cm in a laboratory setting. For wind conditions above about 2 m/s, Fig. (3.10) indicates that on average the ocean surface will add a comparable amount of uncertainty. The ability of the lidar to resolve different depths will therefore depend on both the uncertainty inherent to the lidar measurement and on the surface conditions. In a worst case scenario, the uncertainty is completely dominated by ocean surface effects. The uncertainty associated with an ALB measurement is generally much greater than the uncertainty of the lidar since uncertainties in the aircraft position and orientation must be considered. This added uncertainty, typically on the order of 10 cm, only applies to the surface height measurement. The depth is unaffected since these errors will affect the surface and floor range measurements equally and as such, cancel out. For a surface height measurement, the ocean surface will contribute significantly to the total uncertainty only for the case of maximum standard deviation and will not significantly affect uncertainty in the height measurement on average. For a depth measurement, the ocean surface will dominate the uncertainty for the worst case of maximum standard deviation and will contribute comparably to the lidar uncertainty on average.

An unintuitive result of Fig (3.10) is that the depth uncertainty is less than the surface uncertainty. Since depth measurements depends on the surface measurement, it would seem as if the surface uncertainty would be added into the depth uncertainty making the depth uncertainty greater. In actuality, the correlation in Eq. (3.9) has the effect of producing a better defined, more narrow depth distribution. This effect stems from the fact that the floor response and the surface height response are not independent variables but instead correlated. Subtraction of the surface and floor detection times and conversion to depth actually can have the effect of improving the measurement. For ALB, it is important to have a small depth uncertainty so that subsurface features can be resolved. This correlation is an unintended effect which is beneficial for ALB.

The mean offset error describes the position of the distribution with respect to the "true" value. In this case, the true value is the depth or surface height that corresponds to the center of the lidar beam. The mean offset for the surface response is centered around 0 and therefore negligible.

This is not surprising since it is unlikely for there to be wave features that would consistently weight the surface response in any one direction. The floor response does exhibit a consistent bias. This makes physical sense since refraction and beam spreading will generally result in an increased ray path. The magnitude of this offset is small, being less than a centimeter however it is consistent throughout all wind speeds. Additionally, Fig. (3.10) was generated for normal incidence. From Fig. (3.5), it can be imagined that this offset would increase for a non-nadir pointing angle.

The minimum and maximum offsets for the surface height and depth measurements tell a different story. Although on average these distributions are typically centered on the expected value, for any single measurement it is possible for them to be centered between $\pm$ 2 cm off. The magnitude of this offset range is mostly independent of wind speed. This means that, for any wave conditions, the mean of a distribution of ALB measurements taken over a sufficiently short time interval could be off by a couple centimeters. This fluctuation is important to consider for surface or subsurface mapping when many points are quickly detected. Within a short time interval, a distribution with a width given by Fig. (3.10) will appear however the mean of this distribution will not necessarily be indicative of the actual height or depth.

3.2.2 Horizontal Errors

Horizontal uncertainties from beam spread and from beam deflection were also examined for varying wind conditions. For the beam centroid, the mean deviation from the nominal beam center and the max deviation are shown. The nominal beam center is defined as the location the center ray of the beam lands when the ocean surface is assumed flat. For the beam spread, the x, y, total, and maximum standard deviation are shown. These quantities show how widely around the beam centroid the power in the beam is spread. The combination of these two results determines the spatial resolution of the lidar.

The errors associated with the beam spot size and energy spread are generally greater than with the centroid deviation. However, these two representations of horizontal error shouldn't necessarily be compared as they represent different effects. The beam spread uncertainty is indicative

Figure 3.11: Wind effects on horizontal errors associated with a lidar bathymetry measurement. The deviation from center of the centroid and the spread of the beam are shown.

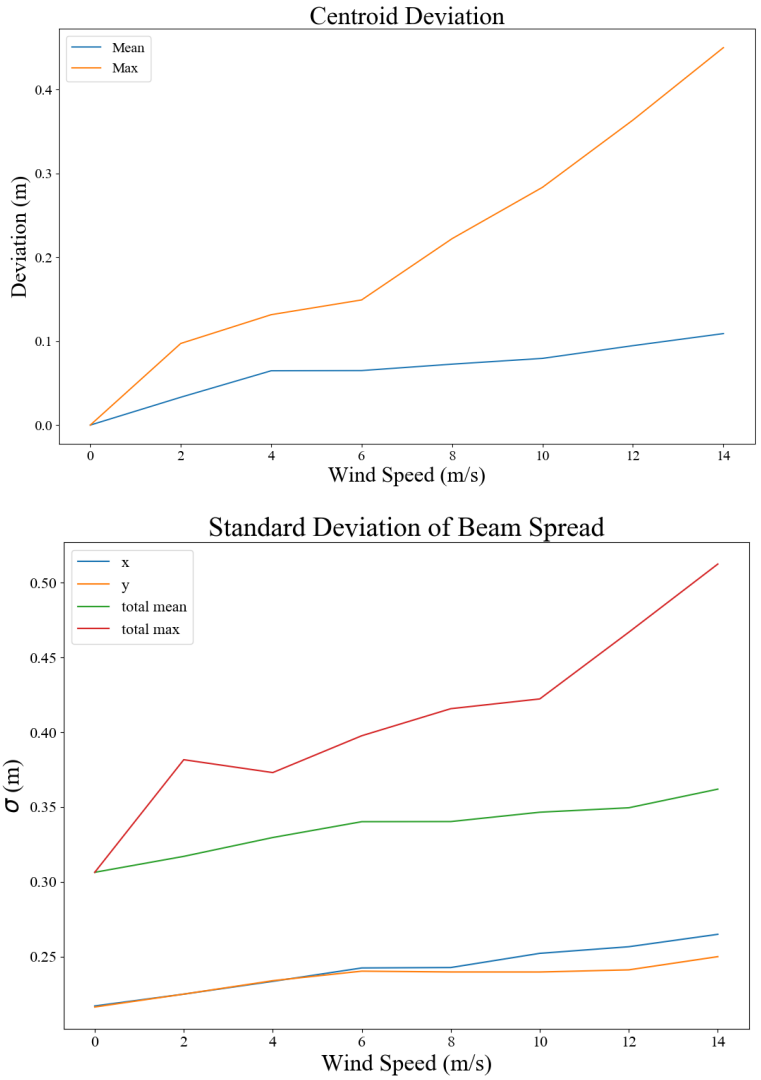

of the size of the lidar spot on the ocean floor. The size of this spot does relate to the horizontal error in that a detection can come from any point in the lidar spot. This spread directly relates to the spatial resolution of the system. The effect of the waves does seem to have an influence on this seeing as the total standard deviation of the beam width begins at a value which corresponds to the lidar beam radius and increases with increasing wind speed. This implies that the ocean waves on average spread the beam. On average, the standard deviation only increases by 5 cm however

the maximum standard deviation grows greatly for increasing wind speed. The maximum standard deviation at high wind speeds is over 50 % greater than the spread for a flat ocean surface.

Movement of the center of the lidar beam is best understood by looking at errors related to the beam centroid position. As opposed to the beam spread which affects the spatial resolution of the instrument, centroid errors have the effect of distorting and biasing the results. In the case of spread, detections will be obtained from a wide range of locations. Errors on the beam centroid can have the effect of redirecting the beam to an unpredictable location. Instead of obtaining detections evenly from locations in the beam spot, the measurement may be biased towards a single location. Fig. (3.11) implies that centroid errors are significant for the case of ALB. As the wind speed is increased, the center of energy for the beam grows from 0 cm to 10 cm. The maximum deviation is much greater and more worrisome than the average. For large wind speeds, the maximum deviation is nearly a half meter or about the same size as the lidar beam spot. This means for a worst case scenario of centroid deviation, the beam center is possibly outside the original beam footprint. This could result in distorted or biased subsurface maps. Since the waves move the beam centroid, this could also result in distorted measurements where the movement of waves through the lidar beam makes it appear as if the floor topography is changing. Unlike with horizontal uncertainty from spread, the deflection of the centroid could be corrected if the slope of the surface were known. This has been demonstrated to be possible by fitting a surface to the lidar point cloud and was shown to improve the uncertainty of the bathymetry data.

The combination of the beam spread uncertainty and the centroid deviation results in the uncertainty in the transverse coordinate for a measured point. Fig. (3.11) shows that the combination of these effects results in greatly increased horizontal uncertainty for increasing wind speeds. Between the two, at wind speeds greater than 8 m/s, about 15 cm of standard deviation is added on average, with double that as a worst case. For a flat ocean, the average horizontal standard deviation is about 30 cm for the INPHAMIS system so this added uncertainty is certainly significant. For even larger wind speeds, the added uncertainty on average does not change significantly however the worst case standard deviation can reach as large as a meter.

The ability of a bathymetric lidar to resolve different subsurface features is significantly dependent on the ocean waves. The uncertainty incurred here has arguably a more significant impact on ALB measurements than the single-shot depth and height uncertainties. This is sensible since from Fig. (3.5), small changes in r_2 due to refraction result in large changes in h.

3.2.3 Wind Speed Variation for Multiple Shots

The distribution over many shots was obtained for wind speeds between 0 and 14 m/s by simulating lidar surface height and depth measurements over 50 seconds. Unfortunately, the time resolution for these measurements is worse than that used in the generation of Fig. (3.9) since numerous simulations had to be run. Therefore the accuracy of these distributions suffers at the fastest wind speeds. At these wind speeds, the ocean waves are long in wavelength and large in magnitude. In order to obtained a correct distribution under these conditions, the lidar must record data for a longer amount of time so that more wave cycles can be captures. A solution to this problem for a real lidar would be to take measurements from a moving platform so that multiple wave cycles can be obtained in less time. The simulated variance of the lidar data in addition to the integrated theoretical surface variance is shown below in Fig. (3.12).

At lower wind speeds, the variance curves for the lidar data match the expected curve with near perfection. The error seen at large wind speeds is likely caused by model limitations. The blame for this rests on a combination of not simulating a sufficiently long lidar time series, and not using a large enough ocean grid. At wind speeds greater than 10 m/s these inaccuracies become significant for the multi-shot distribution. Nonetheless, it is clear the shape of the variance curve still adheres to the theoretical relationship between variance and wind speed for the JONSWAP spectrum. For wind speeds below 10 m/s, the model works with negligible error and Fig. (3.12) indicates that lidar systems are capable of measuring surface height variance.

Fig. (3.12) also demonstrates the relationship between the variance of the surface height and the depth measurement. This figure shows these two quantities are essentially completely correlated when viewed over many shots. This is not a surprising result seeing as the magnitude of ocean

Figure 3.12: Variance for the simulated multi-shot lidar measurements as a function of wind speed. Also shown is the variance that can be expected from theory according to integration of the JONSWAP spectrum.

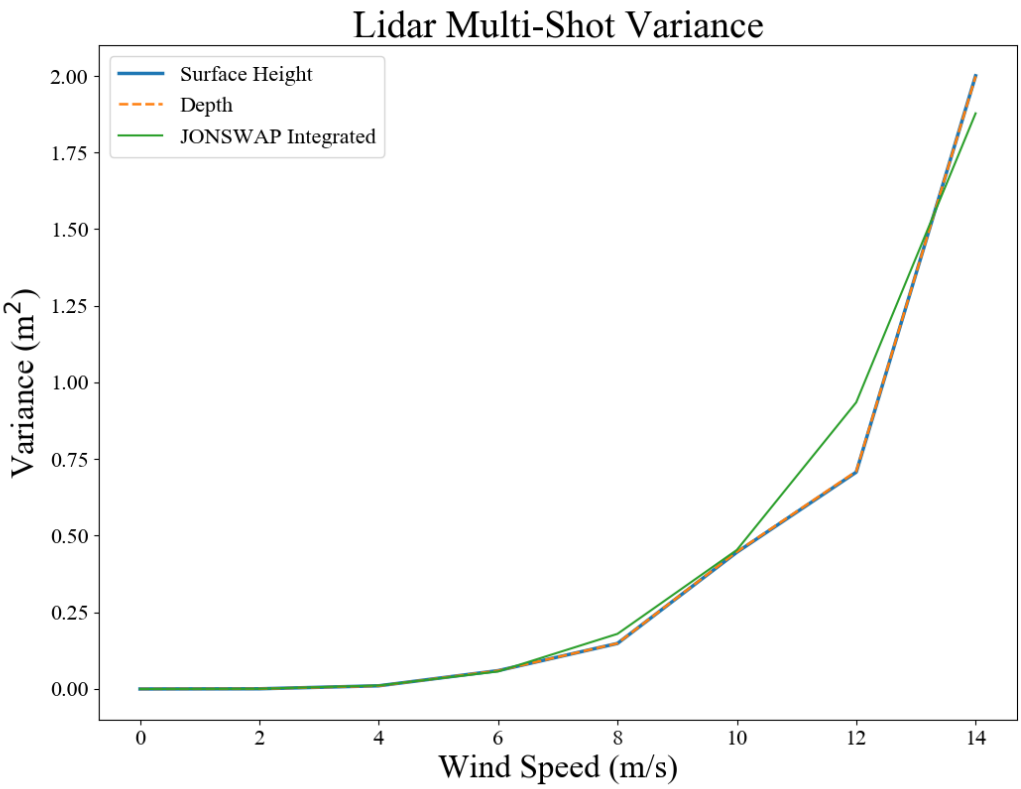

surface waves generally dwarfs any uncertainties or variance associated with the lidar single-shot distributions. For the multi-shot distributions, the mean was also calculated to determine if wave effects limit the estimation of average depth or mean sea level. Once again, model inaccuracies at large wind speeds can be seen. At smaller wind speeds, these figures indicate that the mean depth and mean surface height can be estimated with sub-centimeter precision.

Figure 3.13: Mean of lidar multi-shot distributions plotted as a function of wind speed. These quantities estimate the mean sea surface height and the mean water depth.

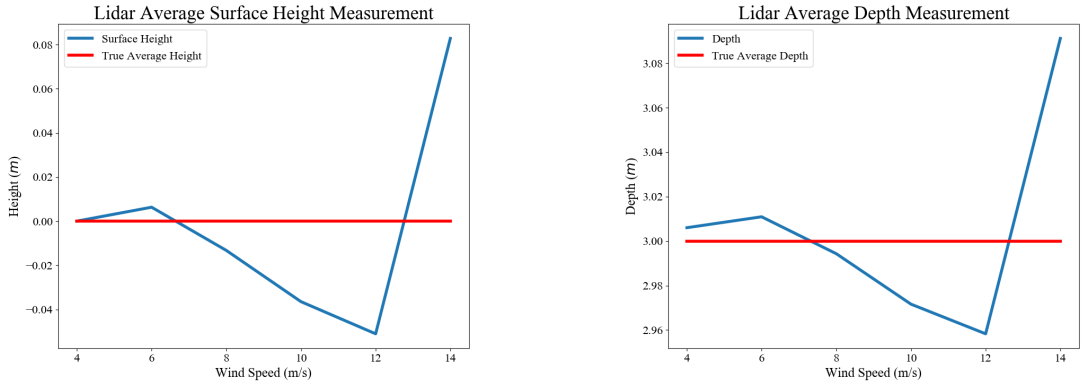

3.3 Off-Nadir Angle Variation

Often times, ALB measurements are taken with the instrument aimed at an angle to the water plane. The cause of this off-nadir angle could be intentional, like with a scanning lidar, or unintentional and due to aircraft orientation. As the lidar is tilted off-nadir, refractive effects begin to be significant even for a perfectly flat ocean surface. An attempt at correcting for these effects can be made since the lidar off-nadir angle is known. In the presence of waves however, refraction from a non-nadir lidar pointing direction and refraction from waves are coupled. This section studies how the distributions and instrument effects described above change for off-nadir lidar measurements in the presence of a wavy ocean surface. These simulations were run over 50 seconds with a wind speed of 8 m/s. The lidar pointing angle is changed from 0 to 20 degrees in increments of 5 degrees. The wind is blowing in the same direction that the lidar is pointing.

3.3.1 Off-Nadir Variation for Single-Shot

First the single shot statistics are presented. These figures are identical in form to those in section 3.2.1.

The standard deviation plot shows that as the lidar off-nadir angle is increased, the single-

Figure 3.14: Average distribution parameters for the single-shot distributions plotted against the lidar pitch angle.

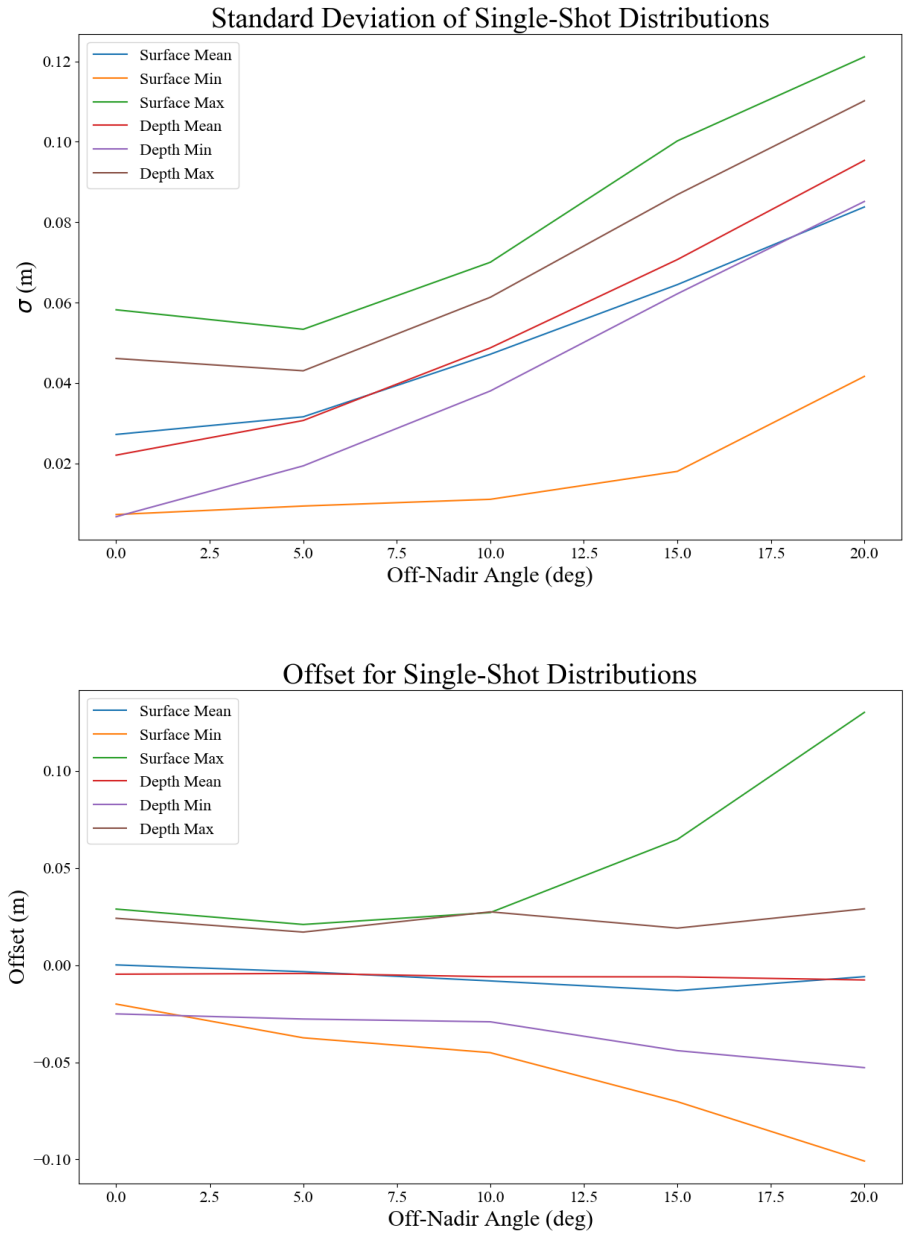

shot distribution also increases in width. This increase appears to be mostly linear with respect to off-nadir angle. It is only nonlinear between normal incidence and 5 degrees. In this region, it appears that the single-shot distribution is independent of lidar off-nadir angle. Additionally, as

off-nadir angle increases, the standard deviation of the depth overtakes that of the surface height. This implies that as the lidar beam incidence is increased, refractive effects become stronger and the floor returns are less correlated with the surface returns. The uncertainty in the floor returns likely increases as well. Increasing the off-nadir angle clearly has a significant affect on the uncertainty for a single lidar surface height or depth measurement. At higher wind speeds, the average standard deviation is easily greater than 5 cm. The maximum standard deviation exceeds 10 cm. These single measurement uncertainties would dominate the total uncertainty in the lidar measurement for INPHAMIS 1 if the aircraft uncertainty isn't included. If the aircraft uncertainty is included, these uncertainties will be of comparable magnitude and will still significantly contribute to the total uncertainty on these measurements. Fig. (3.14) therefore indicates that, for wavy ocean conditions, the lidar scan angle can be a limiting factor for ALB. This result applies to a system similar to INPHAMIS 1. For a different lidar with a different beam divergence and spot size, the off-nadir angle may impose a different limit on the total uncertainty.

The offset from the expected value for the single-shot distribution is also shown as a function of lidar pointing angle. From this plot it can be seen that the mean offset for both the surface height and depth measurement are approximately zero for all lidar pitch angles. The bias towards a larger depth seen in Fig. (3.10) exists only for the nadir case. This make sense seeing as for the nadir case, refraction can only lengthen the ray path resulting in an overestimated depth. For the non-nadir case, refraction could direction the beam towards a shorter path. Up until about 10 degrees, the maximum offset and minimum offset appear to be constant and equal for the surface height and the depth. Past 10 degrees, the surface height offset max and min quickly grow. A possible explanation for this is that the beam is now interacting with more wave features.

Between the increasing standard deviation and the increasing range of possible offsets, the lidar off nadir angle clearly limits both the accuracy and precision of ALB in the presence of ocean waves. These effects become especially significant for off-nadir angles greater than 10 degrees where the added uncertainty can exceed the total ALB uncertainty prior to wave consideration.

3.3.2 Off-Nadir Horizontal Errors

As with the wind speed variation, the transverse coordinate errors are also examined. The simulation setup is the same as with the single-shot distribution results shown above. The off-nadir horizontal errors are shown in Fig. (3.15).

Figure 3.15: Lidar pointing angle effects on horizontal errors associated with a lidar bathymetry measurement. The deviation from center of the centroid and the spread of the beam are shown.

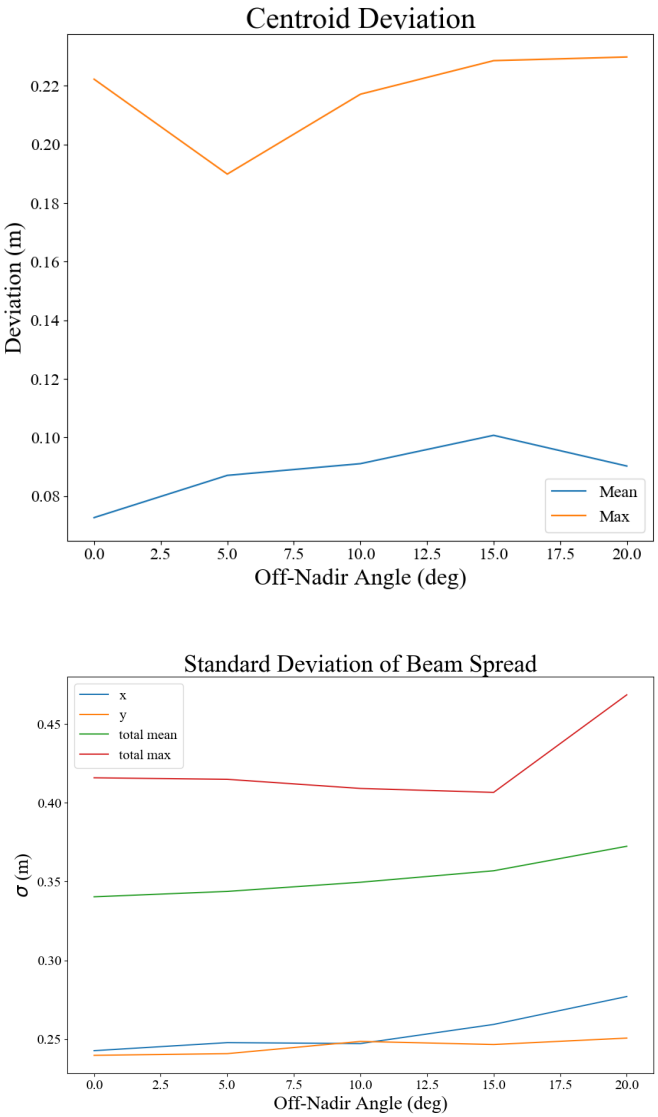

Somewhat surprisingly, the effect of a changing off-nadir angle on the beam spread and centroid deviation is quite small. This is due to the fact that refraction due to a non-nadir angle of incidence is included in determination of the nominal beam center. For a non-nadir lidar pointing angle, refraction can be considered however the ocean must be assumed as flat. As a result, the transverse coordinate errors only minimally increase with respect to the lidar pointing angle. Generally, the horizontal coordinate error and spatial resolution for ALB is based off the wind speed/wave conditions.

3.3.3 Off-Nadir Angle Variation for Multiple Shots

In order to see if a off-nadir lidar angle has any affect on the distribution of surface height and depth measurements taken over a long time, the multiple shot distribution was also generated.

Figure 3.16: Variance for the simulated multi-shot lidar measurements as a function of off-nadir angle. Also shown is the variance that can be expected from theory according to integration of the JONSWAP spectrum.

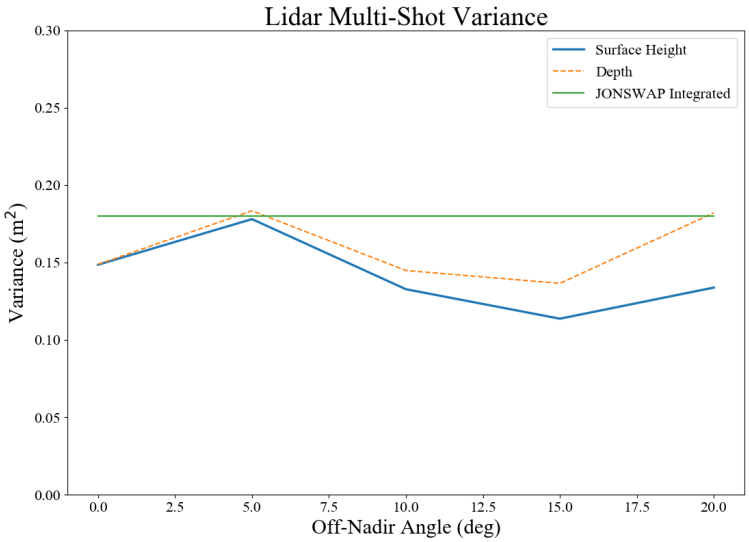

It is clear from this figure that there is some error between the expected and modeled variances. However, it is more than possible that this error is due to the model as discussed in section

3.2.3. This is supported by the fact that the error for the normal incidence case is similar to that seen for the other cases. Additionally, there is no clear trend to the curves in Fig. (3.16). All in all, no strong claim can be made about the effect the off-nadir angle has on the surface height and depth variance over many lidar samples. The simulated variances shown in Fig. (3.16) do still appear to be close to the expected value. If these variances were matched to their corresponding theoretical wind speeds, the results would still yield a wind speed near 8 m/s.

On a different note, the depth and surface height curves can be seen beginning to separate at larger off-nadir angles. This is quite different than the behavior seen in Fig. (3.12) where these two curves are identical. This illustrates how the depth and surface height begin to decorrelate as the off-nadir angle increases.

Shown below are the means for both the multi-shot surface height and water depth measurements. As with Fig. (3.16), there is no clear trend exhibited by these plots. Possibly, these plots show a bias on the order of about a centimeter towards a larger height and water depth. This could be a result of the lidar being more likely to capture a wave peak than trough. For both cases the mean is within 2 centimeters.

Figure 3.17: Mean of lidar multi-shot distributions plotted as a function of off-nadir angle. These quantities estimate the mean sea surface height and the mean water depth.

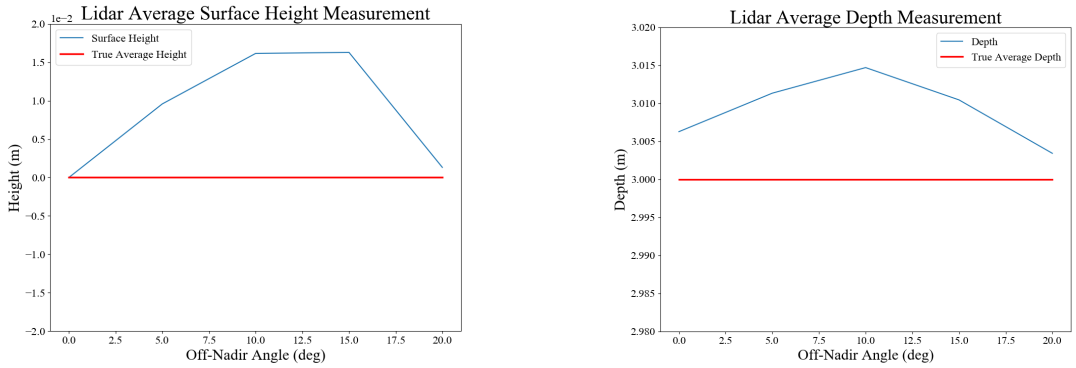

3.4 Polarization

Although many lidars do not rely on polarization, the INPHAMIS 1 lidar for which this work was based off is highly sensitive to polarization. The INPHAMIS 1 system has two polarization sensitive channels which allows it to separate and differentiate between photons returning from the water surface and photons returning from the sea floor. Transmission through the water surface can affect the polarization of the received light resulting in possible contamination between the polarization channels. For lidar-wave model results shown in the previous sections the polarization of the returning rays calculated along with the timing distributions. For each lidar measurement, the Stokes vector for each ray is determined and then averaged together to obtain the polarization state of the returning light. This is only done for the signal returning from the floor since the simulation assumes the signal reflected off the surface maintains its original polarization. With the wind speed set as 8 m/s and the off-nadir angle set as 0, the following distributions are obtained for the Stokes components S1 and S2 over the course of a 50 second simulation. S3 isn't shown as it is always zero for these simulations since the transmitted Stokes vector is simplified as perfectly linearly polarized light.

Figure 3.18: Received distribution of Stokes parameters over course of simulation.

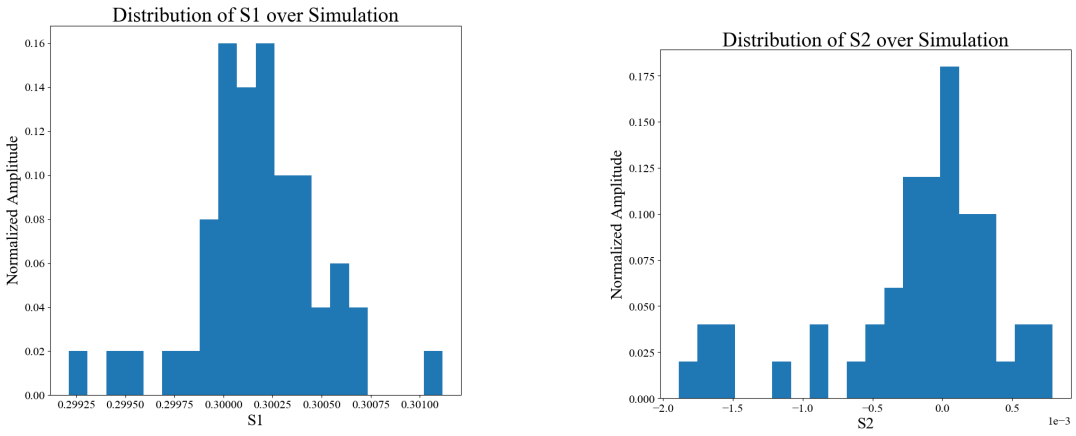

As seen in Fig (3.18), the width of these distributions is quite small. For S1, the distribution

is centered near 0.3. The cause of this can be traced back to the polarization properties of the ocean floor. As mentioned in section 2.3.3, the ocean floor is chosen to be partially depolarizing with d=0.7 in Eq. (2.102). This results in a strong linearly polarized component for the received light. In order to investigate the effects of the ocean surface independent of the polarization properties of the ocean floor, the floor is set to be completely depolarizing. This is a simplified way of viewing this problem since in reality the subsurface object detected by the lidar can exhibit a wide range of different polarization properties and depending on these polarization properties, the ocean surface may have different effects.

With a completely depolarizing subsurface, the resultant Stokes components are shown in Fig. (3.19).

Figure 3.19: Received distribution of Stokes parameters over course of simulation.

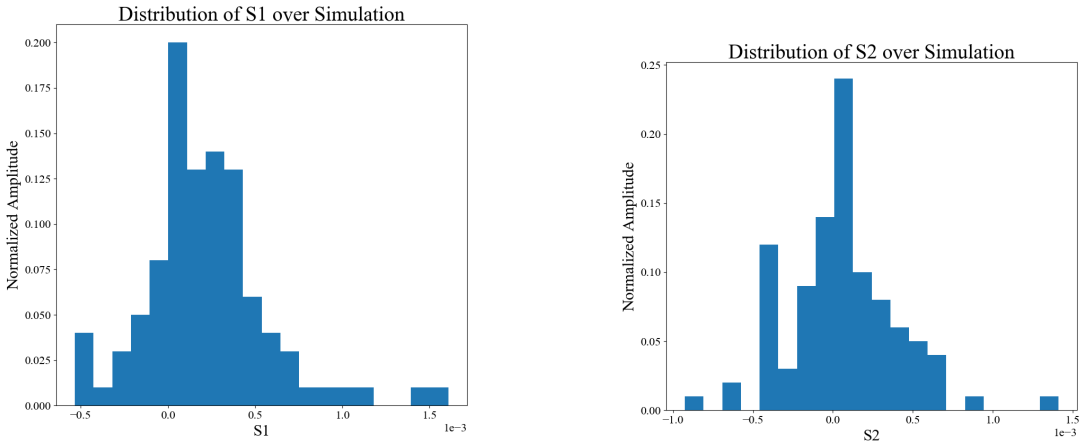

As these plots show, the received light is very weakly polarized for this case. This demonstrates how the polarization properties of the subsurface scatterer are generally much more influential in determining the received Stokes vector. Nonetheless, even extremely weakly polarized light can have an effect on the system. Generally, the results shown in Fig. (3.19) should not have too great an affect on INPHAMIS 1 measurements since very little of the received light from the ocean floor will be polarized and incorrectly characterized as a surface return.

As with the previous sections, the relationship between the received polarization and surface conditions is examined along with the polarization dependence on off-nadir angle. It is expected that variations in the off-nadir angle will have the largest effect. These results are shown below. The mean, max, and min of both the S1 and S2 component over the 50 second simulation are shown along with the standard deviation.

Figure 3.20: Relationship between the received Stokes parameters and wind speed.

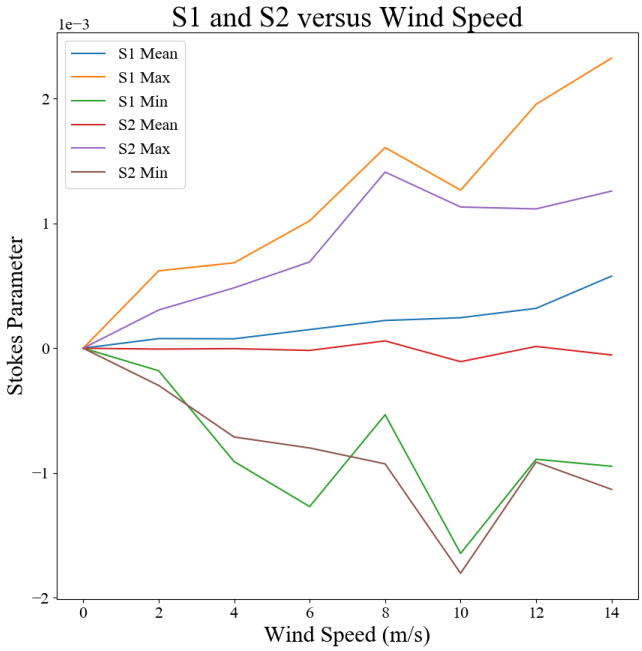

For wind speed variation, while the average value for S1 and S2 barely change, their variance over the course of the simulation increases greatly. Additionally, S1 begins to show a consistent mean value. The received light is becoming increasingly polarized, although by a very small amount. Furthermore, the polarization is the same as the transmitted light meaning there could be some extremely minimal contamination between polarization channels. The increasing standard deviation of the Stokes parameters indicates that as the wind increases, the polarization state of the received light becomes more and more unpredictable. At high wind speeds, any contamination

Figure 3.21: Variation of the received Stokes parameters with regards to wind speed.

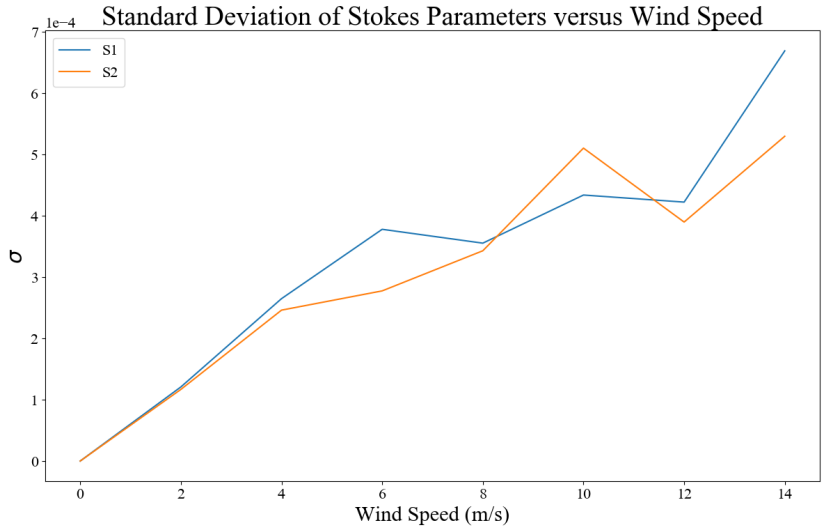

Figure 3.22: The received Stokes parameters and their relation to lidar off-nadir angle.

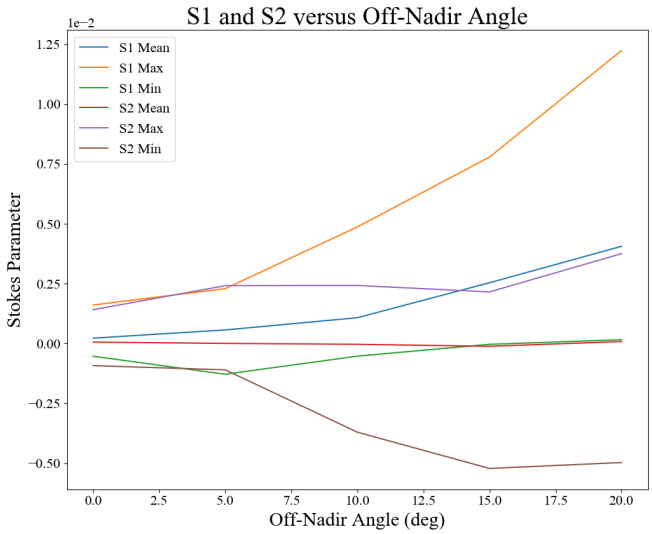

between the polarization dependent detectors for INPHAMIS 1 will become more erratic and polarization dependent filtering of the floor returns will become less dependable. Floor returns may accidentally be detected by the surface channel or discarded from the floor channel. However, for

Figure 3.23: Standard deviation of the received Stokes parameters for different lidar angles.

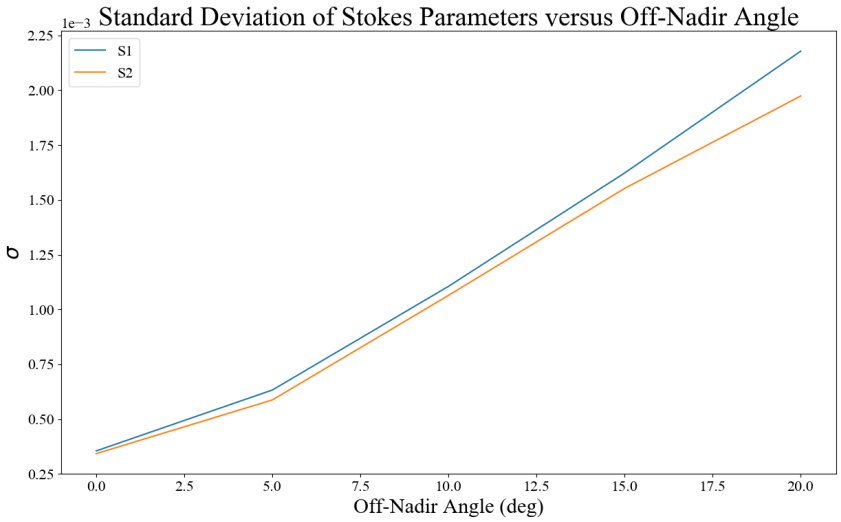

this to happen, the returning light must be more strongly polarized than that shown in Fig. (3.20). This may occur for a floor that is not completely depolarizing. However, for the current case, any contamination between channels is likely negligible.

Variation of the lidar off-nadir angle has a noticeably larger affect on the polarization of the received light. As Fig. (3.22) shows, variation of the off-nadir angle can result in changes an order of magnitude larger than changes in the ocean surface conditions. This plot shows that for lidar pointing angles greater than 5 degrees, the S1 component grows to nearly a half percent of S0. The maximum for S1 is over a percent of S0. The S1 component appears to become biased towards linear horizontal polarization whereas the S2 component does not seem to have any clear bias. The standard deviation for these components over the course of the simulation grows linearly. Although still not large enough to cause significant concern, the floor returns at large off-nadir angles are possibly large enough to be see by the system. It is still unlikely that polarization effects from the ocean surface would significantly corrupt polarization dependent ALB data.

3.5 Summary

Using the lidar-ocean wave model described in chapter 2, the distributions of lidar detections have been simulated for a robust range of scenarios. Using the simulated received signals, parameters such as the surface height and water depth are modeled. The results of this model indicate that, for a single lidar measurement, the ocean surface can cause a wide range of behavior. The distributions can be differently shaped depending on the wave conditions in the lidar footprint and the width and center of these distributions varies significantly.

The uncertainty added by these distributions to the total ALB uncertainty is dependent on wind speed and lidar off-nadir angle. Changing wind speeds generally add standard deviation on the order of a centimeter whereas the off-nadir angle can add standard deviation on the order of 10 cm. Both of these effects can impose a limit on the accuracy and precision of ALB measurements although the off-nadir angle is the domineering effect.

The horizontal coordinate error is also considered. Due to a combination of beam spread effects and beam centroid errors due to refraction, the spatial resolution of the lidar is worsened. It is shown that wind speed has the greatest effect on the horizontal uncertainty whereas the effect of the off-nadir angle is mostly trivial. Different wind conditions can, at worst, double the uncertainty in the transverse location detected by the lidar.

Lidar distributions obtained over a longer time period are also simulated. From these distributions, the ability to determine the average water depth, mean surface height, and surface variance is shown. Although numerical errors associated with the model have an affect on these distributions, in general it is clear that they follow the expected behavior. The relationship between the variance of these distributions and the surface variance shown in Fig. (3.12) shows that there is, in theory, a relationship between the wind speed and the variance of the multi-shot lidar distribution.

Polarization effects are considered last. The simulation shows a significant dependence on the polarization properties of the ocean floor. For a completely depolarizing floor, the surface does affect the polarization of the received light however this effect is very weak and should not

significantly impact polarization dependent lidar detections.

Chapter 4

Real ALB Data and Georeferencing

Over the course of the past several years, the INPHAMIS 1 system has been involved in several flight campaigns. In the latest mission, ARISTO, the system was installed on a Gulf Stream 5 aircraft and data was taken for several days at variety of locations around the United States. Most interesting to this research was a flight done over the ocean off the coast of California. On this flight, the aircraft descended to an altitude of less than 200 meters at which point the surface could be detected. It is important to note that the INPHAMIS 1 system is an ongoing project and the resultant data is not of perfect quality. Namely, the time to digital converter used for recording photon detections was not behaving properly for this flight campaign and there are numerous sections of data with erroneous photon count rates. Fortunately, for the period of data where the ocean surface was visible this was not an issue, however, there is an issue with large data gaps due to latency in the time to digital converter. Analysis of portions of the lidar time series where these gaps are present is difficult due to the jagged behavior they introduce. Although wave structures can clearly be seen in the data, the gaps make it so the full surface cannot be resolved.

In this section, the lidar data obtained from this campaign will be analyzed in context of the ocean surface simulation.

4.1 Georeferencing

4.1.1 Reference Frame Conversions

By itself, the lidar only records range. In order to extract useful information such as height and position about targets sensed from an aircraft, the lidar range data must be converted to a point cloud. Additionally, the point cloud should be referenced to something, which in this case will be the Earth's surface. This process is called georeferencing and involves converting the lidar range between several different reference frames[28]. To start, the lidar range is described as a vector in the lidar frame. This lidar frame is the same as that described in section 2.3.4. This is a simple formulation since in this frame, the lidar range vector aligns with the z-axis. Next, the lidar vector is converted into the aircraft frame as described in section 2.3.4. However, with real airborne lidar data the lidar origin cannot be assumed to be equivalent to the aircraft position. The georeferencing process requires the additional step of adding a vector in the aircraft frame which references the lidar source to the on-board GPS receiver. At this point, we have a vector in the aircraft frame from the aircraft GPS to the target detected by the lidar.

The next step is to convert the lidar vector into a global frame where it can be referenced to a representation of the Earth's surface. First, conversion from the aircraft frame into the local, North-East-Down frame, is done using the aircraft Euler angles. From here, the lidar vector is then converted into a global, Earth-Centered Earth-Fixed frame using a transformation matrix. The ECEF frame used is that of the WGS84 datum. It is the standard frame for use with GPS and is useful as a global frame in which the various position vectors encountered in the georeferencing process can be combined. The center of the WGS84 frame is the Earth's estimated center of mass. The uncertainty in the position of this origin is believed to be less than 2 cm. The x-axis is defined to be in the plane perpendicular to Earth's pole or rotational axis. Additionally, the x-axis is aligned with the zero longitude line which, for the WGS84 frame, is the BIH zero meridian. The z-axis is the IERS reference pole which closely represents the Earth's axis of rotation. At last, the y-axis is defined to complete a right handed coordinate system with the x and z axes. Furthermore,

the longitude along the y-axis is 90 degrees. The transformation matrix which converts coordinates between ECEF and NED is[43]:

$$\boldsymbol{T}_{ECEF}^{NED}(\phi,\lambda) = \begin{bmatrix} -sin(\phi)cos(\lambda) & -sin(\phi)sin(\lambda) & cos(\phi) \\ -sin(\lambda) & cos(\lambda) & 0 \\ -cos(\phi)cos(\lambda) & -cos(\phi)sin(\lambda) & -sin(\phi) \end{bmatrix} \tag{4.1}$$

In order to convert from NED to ECEF, the inverse of this matrix should be taken. The position vector for the aircraft can also be found in this coordinate frame by converting the GPS geodetic latitude, longitude, and height above the WGS84 reference ellipsoid into ECEF coordinates. This can be done provided that one knows the reference ellipsoid parameters. For the WGS84 ellipsoid, the semi-major axis, a, is 6378137 meters and b, the semi-minor axis, is 6356752.31424518 meters. The aircraft position can then be found using the following equations.

$$e = \sqrt{\frac{a^2-b^2}{a^2}} \tag{4.2}$$

$$N = \frac{a}{\sqrt{1-e^2\sin^2(lat)}}$$

$$X = (N+alt)\cos(lat)\cos(lon)$$

$$Y = (N+alt)\cos(lat)\sin(lon)$$

$$Z = (N(1-e^2)+alt)\sin(lat)$$

In the ECEF frame, the aircraft position and lidar range vector can now be added resulting in a vector that points from the center of the Earth to the target measured by the lidar. It is important to be able to convert this point back to the form of latitude, longitude, and altitude so that later, the height of the lidar point above some reference surface can be determined. This backward conversion was implemented in python based off the matlab function ecef2lla. It works according to fixed point iteration and Bowring's formula[44]. A visualization of the different reference frames encountered in the georeferencing process is shown below.

Figure 4.1: Some of the different vectors and reference frames encountered in the georeferencing process for airborne lidar data.

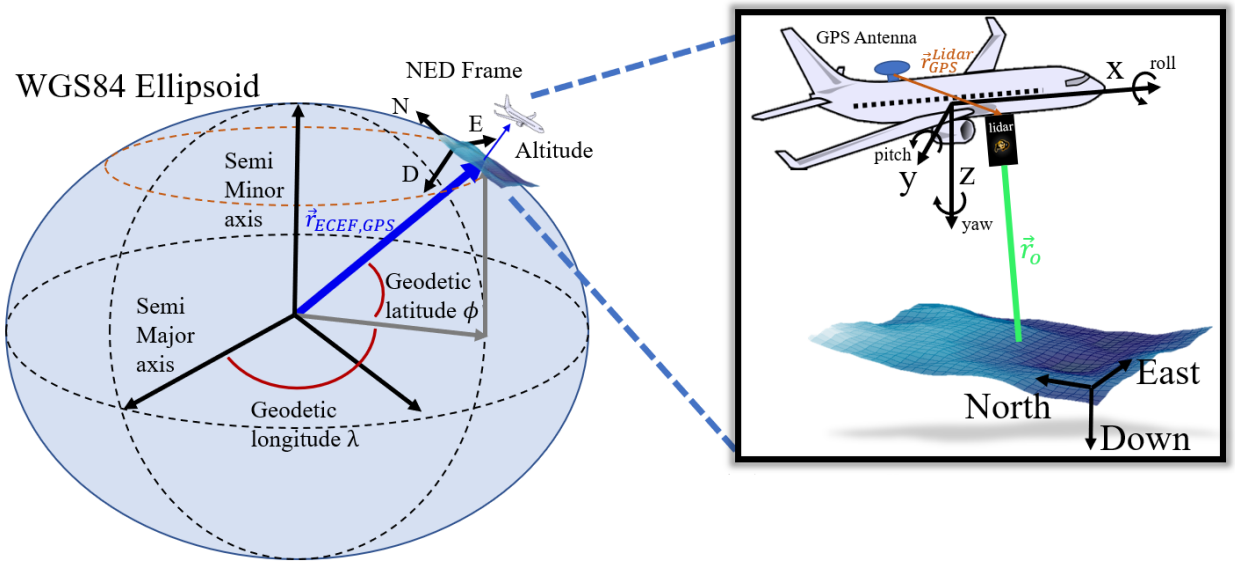

As a whole, the process of georeferencing is given by [28]

$$\vec{r} = \vec{r}_{ECEF,GPS} + \left(\boldsymbol{T}_{ECEF}^{NED}(\phi,\lambda)\right)^{-1} \boldsymbol{T}_{B}^{NED}(\psi,\theta,\Phi) \left(\boldsymbol{T}_{L}^{B} \begin{pmatrix} 0 \\ 0 \\ r_o \end{pmatrix} + \vec{r}_{GPS}^{L} \right) \tag{4.3}$$

where ECEF, NED, B, and L signify the inertial, WGS84 reference frame, the North-Earth-Down frame, the aircraft body frame, and the lidar frame respectively.

4.1.2 Earth Surface Reference

The mathematical description of Earth is not necessarily straight forward. There are many ways of varying complexity with which one can describe the shape of Earths surface. Furthermore, these Earth surface approximations have varying properties that make them suitable for certain applications but spurious for others. For example, the WGS84 ellipsoid is often used as a most basic representation of the Earth's surface. Not surprisingly, an ellipsoid does a poor job of capturing the complex shape of Earth's surface and the error between the ellipsoid height and the true surface

height can be on the order of hundreds of meters when over open ocean. On land, where elevation changes are more rapid, these errors can be significantly greater. A step up in complexity and accuracy can be obtained by using a geoid. Geoids are mathematically defined using a summation of many spherical harmonics and are meant to represent the Earth as an equipotential surface. This has drawbacks when it comes to describing the sea surface since changes in underwater topography can significantly affect the geoid shape at the sea surface. There are several WGS84 geoids which are commonly used such as the EGM96 and EGM2008 geoids.

Due to the fact that the geoids described above are not ideal choices for representing the sea-surface, it is necessary to find a different reference. There are many choices for what surface the lidar data should be referenced to but the one used in this analysis is the Mean Sea Surface (MSS). The MSS is meant to represent the ocean surface averaged over a long time scale. This removes variations related to seasonal and daily behavior among other things. The MSS can be obtained as a gridded dataset, processed by SSALTO/DUACS and distributed by AVISO+ (https://www.aviso.altimetry.fr) with support from CNES. This product was computed using 20 years of satellite altimetry data from missions such as TOPEX/Poseidon and Jason-1 and 2. The Mean Sea Surface in context with some of the other previously described surfaces is depicted below in Fig. (4.2)[45].

Although not included in the sea surface reference estimation, also shown in Fig. (4.2) is the Sea Level Anomaly (SLA). The SLA is the difference between the average sea level on a short time scale and the MSS. SLA is another AVISO satellite altimetry product and can be obtained as a grid of heights in the region of where the lidar data was taken and at the date of when the lidar data was taken. SLA captures behavior such as el Nino. In the region where the lidar data to be processed was taken, the SLA is on the scale of centimeters so it is not included in the algorithm. Inclusion of SLA would involve interpolating the SLA grid and adding the SLA value at the desired latitude and longitude to the interpolated MSS height.

A drawback associated with using the MSS reference is that the MSS height data is referenced to a different ellipsoid than the WGS84 ellipsoid used for the rest of the georeferencing

Figure 4.2: The Mean Sea Surface among other related references. Figure taken from "A New Version of Ssalto/Duacs Products Available in April 2014".

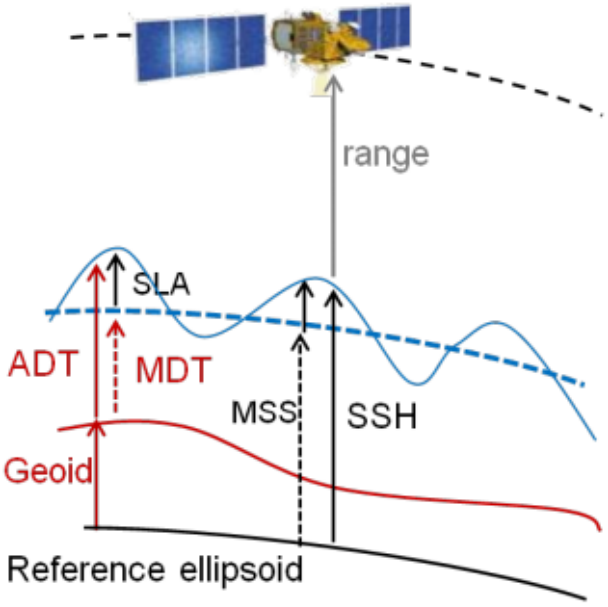

process. This different ellipsoid, called the TOPEX/Poseidon ellipsoid has a semi-major axis length of 6378136.3 meters and a flattening coefficient (f) of 1/298.257. This results in a semi-minor axis of 6356751.600562938 meters. In general this ellipsoid is a meter below the ellipsoid used in the WGS84 datum. In order to reference the MSS data to the WGS84 ellipsoid, the TOPEX/Poseidon ellipsoid height in relation to the WGS84 ellipsoid must be determined for any latitude and longitude. This is done by using Eqs. (4.2) with the altitude set to zero and with TOPEX/Poseidon ellipsoid parameters. This gives a location on the TOPEX/Poseidon ellipsoid in ECEF coordinates. This location is then converted back into latitude, longitude, and altitude using the ecef2lla algorithm. This algorithm, is based off the WGS84 ellipsoid so the output altitude is the height of the TOPEX/Poseidon ellipsoid in reference to the WGS84 ellipsoid. This height can then be added to the MSS height in order to reference the MSS data to the WGS84 ellipsoid.

We now have a representation of the Earth surface as a height field referenced to the WGS84 ellipsoid as a function of latitude and longitude. The measured lidar point can be easily related to

this surface if expressed in terms of latitude, longitude, and altitude. After using Eq. (4.3) to find the position vector of the lidar points, this can be done by way of the ecef2lla algorithm. With both the reference sea surface and the lidar point now located in the same frame, the altitudes can be subtracted to find the ocean surface height measured by the lidar.

4.2 Lidar Wave Data

Before analyzing and processing the georeferenced lidar point cloud, it is necessary to extract the lidar measurements that correspond to the ocean surface. Since the INPHAMIS lidar is sensitive to single photons, the detections made by the lidar are often from noise. An example of unprocessed INPHAMIS 1 data is shown below.

Figure 4.3: Unprocessed INPHAMIS 1 data. The surface can be seen as an area of more frequent photon detections. Atmospheric detections occur before the surface and everything after is either dark counts or solar detections.

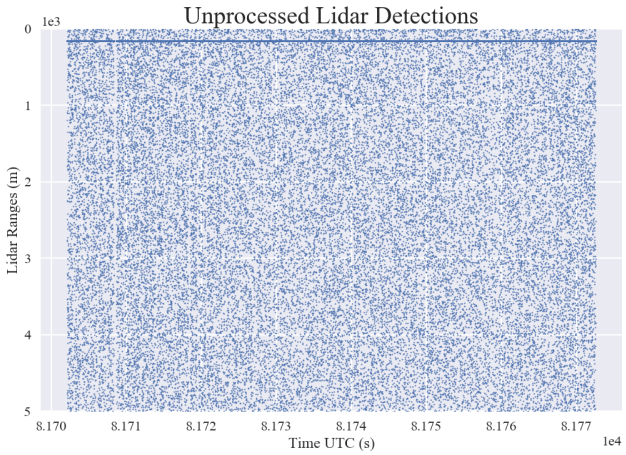

A surface finding algorithm has been developed in order to sift through this point cloud and discard photons not associated with surface detections[38]. This algorithm works by binning the lidar detections into coarse range bins. This binning occurs over intervals of time which can be thought of as time bins. The range bin with the highest amount of detections is assumed to be that which corresponds to the sea surface. Next, a slab is created around the location in the surface

range bin where the most detections occur. All points outside this slab are discarded and all photon detections that land within it are assumed to be from the surface. The width of the slab should be selected based off the single shot uncertainty for the current surface conditions.

After applying this algorithm to the lidar point cloud, the ocean surface can be clearly seen provided that the lidar returns from surface glint are strong enough. As mentioned earlier, the data gaps in the INPHAMIS files are an issue with the ARISTO data. These gaps make it impossible to measure the ocean surface for significant portions of time. This causes issues when performing statistics or spectral analysis on the ocean surface time series. An example of these data gaps is shown in Fig (4.4).

It should be noted that a full analysis of surface finding and the surface returns for photon counting systems is much more involved[46]. Effects related to system dead times and single photon counting electronics can have surprising and significant effects on the biases associated with surface detection and the probability of detecting the surface.

Figure 4.4: Lidar ocean wave data taken with the INPHAMIS 1 system on the ARISTO flight campaign. Data gaps that impacted the quality of the data can be clearly seen.

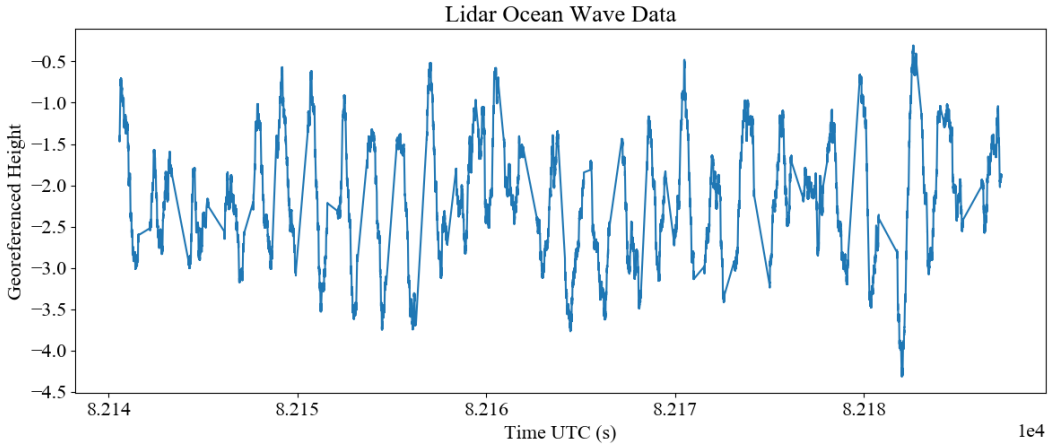

Although these gaps make it impossible to use the full lidar ocean time series, a portion of the data that is not significantly plagued by these gaps can be utilized. One of the best portions of lidar wave data and the one that will be used for analysis and model validation going forward is

shown below in Fig. (4.5). Data gaps still exist in this section however they are much smaller and do not cause the same jagged jumps as in Fig. (4.4).

Figure 4.5: High quality period of ocean wave data taken with the INPHAMIS 1 system on the ARISTO flight campaign. This segment of the lidar data is what will be used for the rest of this study.

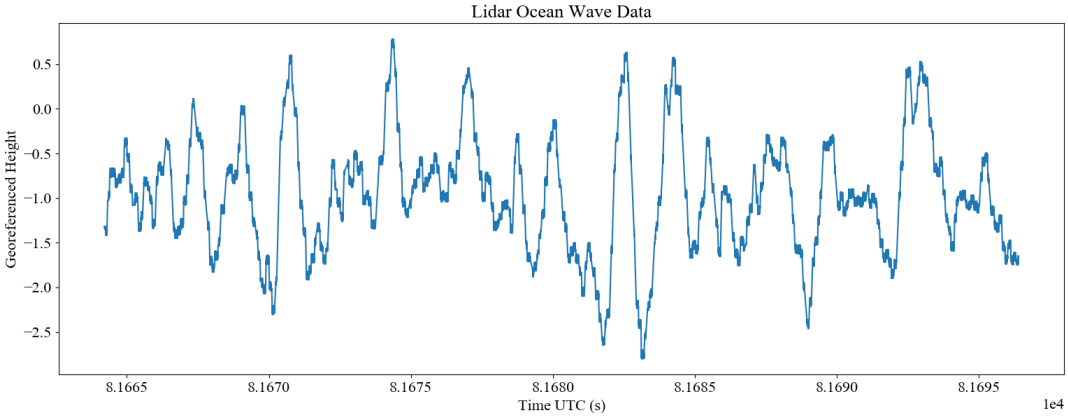

This data was obtained off the coast of California on March 2nd 2017. The plane was travelling South to North in the period of time where lidar ocean data was collected. The data in Fig. (4.5) was obtained for about 30 seconds at a longitude of 128.06 degrees West and a geodetic latitude of 39.9 degrees North[38].

Since the wave size for this section of data is much larger than the lidar beam spot, the variance of the lidar measurements is representative of the variance of the ocean surface. The variance is maybe the most important quantity which can be determined from lidar ocean data as it provides a means of estimating the wind speed and determining the significant wave height, a commonly used parameter for describing the wave conditions on the ocean. The significant wave height, as a function of the surface variance is[17]

$$H_{\frac{1}{3}} = 4\sqrt{\langle \zeta^2 \rangle} \tag{4.4}$$

where $H_{\frac{1}{3}}$ is the significant wave height and $\langle \zeta^2 \rangle$ is the variance. Using the lidar data displayed in Fig. (4.5), the variance is calculated to be 0.4325 meters resulting in a significant wave height

Figure 4.6: Flight track for the ARISTO flight on the day of March 2nd 2017. The descent to the ocean surface where lidar sea surface detections were made is shown in green.

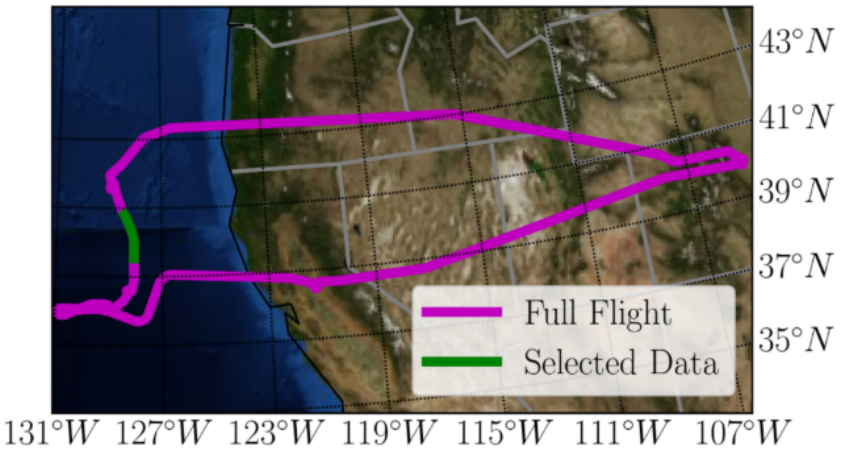

of 2.63. By varying the wind speed in the lidar ocean model, the wind speed that results in a surface variance of 0.4325 meters can be determined. This estimated wind speed comes out to approximately 9.9 m/s.

The validation of these values can be determined from publicly available satellite data products. These were obtained from AVISO however they are available from several different sources. For the time and location which correspond to the lidar wave data, there is no direct satellite overpass. The AVISO data used for comparison here makes up for this by processing and interpolating data from multiple satellites. The result is a significant wave height and wind speed product available twice daily. The lidar data shown in Fig. (4.6) was obtained near the end of March 2nd in UTC time. AVISO significant wave height and wind speed data is released each day 00:00:00 UTC meaning that two days of significant wave height data and wind speed data are applicable. The data files used are March 3rd 00:00:00, which contains information from all of March 2nd, and March 4th 00:00:00, which contains information from all of March 3rd. Plots of these datasets are shown below in Fig. (4.7).

It is clear from these plots that, around the time of the ARISTO flight, significant changes in the surface conditions were occurring. Unfortunately, this type of behavior is not ideal for model

Figure 4.7: Wind speed data for the applicable time frame in the region of the ARISTO flight. These plots were obtained using the AVISO Live Access Server. On the left is data from the day of March 2nd. On the right is data from the day of March 3rd. This product was processed by SSALTO/DUACS and distributed by AVISO+ (https://www.aviso.altimetry.fr) with support from CNES.

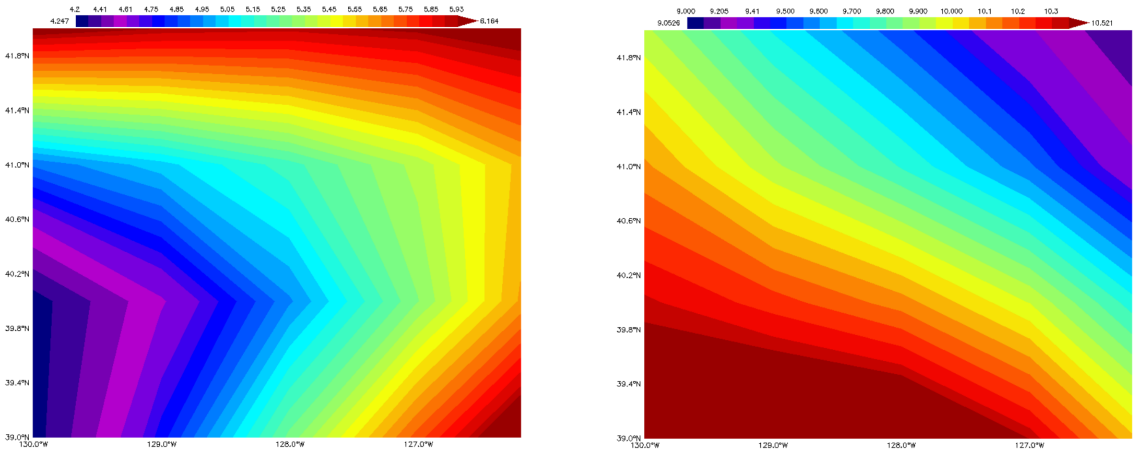

Figure 4.8: Significant wave height data for the applicable time frame in the region of the ARISTO flight. These plots were obtained using the AVISO Live Access Server. On the left is data from the day of March 2nd. On the right is data from the day of March 3rd. This product was processed by SSALTO/DUACS and distributed by AVISO+ (https://www.aviso.altimetry.fr) with support from CNES.

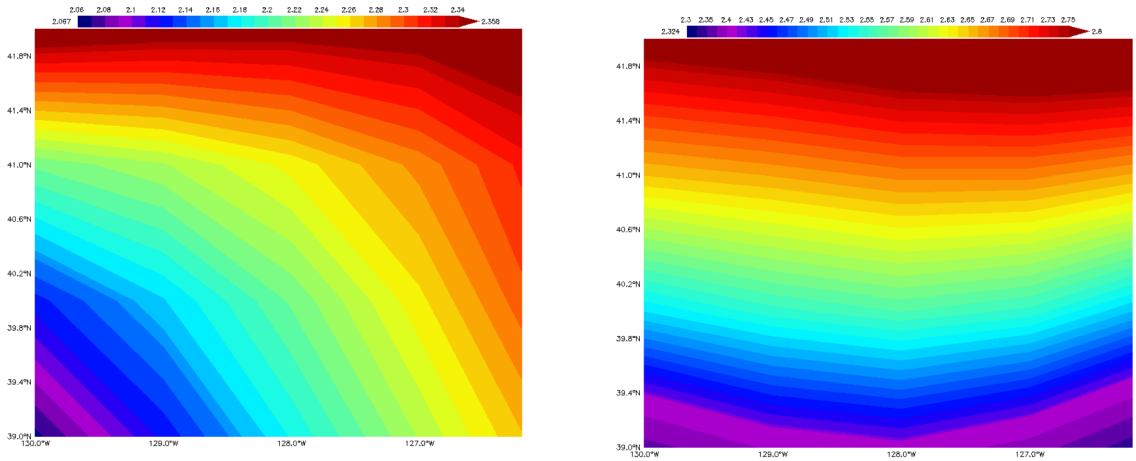

validation since the lidar-ocean assumes a fully developed sea surface state. Nonetheless, the wind speed given by the model for the calculated lidar time series variance is quite close to that seen the day of March 3rd for a latitude and longitude of 39.9 N and 128.06 W respectively. The significant wave height determined from the INPHAMIS 1 data is also close to that seen on March 3rd. This is possibly a more significant result than the wind speed as it demonstrates lidar can be used to extract information about the ocean surface. Radar sensing from a satellite is still clearly the superior form of ocean surface sensing due to it's coverage, accuracy, and proven use. However, lidar's superior spatial resolution and ability to map the surface and measure small wave structures may find use for some applications as we continue to find new ways to extract ocean information.

4.3 Spectral Analysis and Comparison

It is encouraging for model validation that the AVISO data shown in Fig. (4.7) is in agreeance with the wind speed predicted by the model for the surface variance conditions seen in the INPHAMIS 1 data. However, simply having a modeled surface variance that is reasonable for a given wind speed does not ensure the model is working properly or is representative of ocean wave conditions seen in nature. Further model validation can be obtained by analyzing the spectral content of the lidar time series. In theory, the directional spectral density obtained by combining the JONSWAP spectral density and the directional spreading function, should manifest in the lidar time series. The transformation from the directional spectral density used in the ocean model to the spectral density of the lidar wave data is complicated by the fact that the lidar data is obtained from a travelling reference frame. Ocean waves travelling in the same direction as the aircraft will experience a significant frequency shift due to this effect while waves propagating orthogonal to the aircraft track experience no effect. In the following sections, the frequency spectrum seen in a time series from the aircraft perspective will be derived.

While not a focus for this thesis, it is possible that the frequency content of the lidar ocean-wave time series could be useful for purposes besides model validation. Although lidar is capable of producing wave information such as height, information regarding the shape of the waves, their

speed, and their direction of travel is lost for a fixed beam system. Some of this information may be recovered by further examining the lidar time series, specifically with frequency analysis[47]. The frequency spectrum of the lidar data could also possibly be compared to the predicted spectrum to allow for detection of unexpected behavior. This may mean detecting unexpected surface wave structures caused by effects other than wind. This comparison could also yield information about how the actual ocean power spectrum differs from the theoretical ocean power spectral density model for the given wind conditions. At last, this comparison may allow for detection and removal of erroneous range effects in the ALB process. For example, if the lidar is mounted to a plane which is experiencing oscillatory motion, those frequencies may reappear in the lidar time series and cause spurious ocean surface results.

4.3.1 Moving Reference Frame Effects

When viewed from a moving reference frame such as an aircraft, the waves' observed frequency is distorted by their movement. As it turns out, there is a defined relationship between the speed of the waves and the frequency of the waves. This relationship is derived from the dispersion relation for ocean surface wave (Eq. (2.25)).

$$\omega^2 = gk \tag{4.5}$$

For travelling waves such as those in Eq. (2.37), the phase speed of the waves is given by equation 4.6.

$$v_p = \frac{\omega}{k} = \frac{g}{\omega} \tag{4.6}$$

The implications of Eq. (4.6) are interesting; the faster a wave oscillates in time, the slower it travels. When viewed from a moving reference frame, the shift in the apparent frequency of the waves is dependent on the direction of the waves and the speed of the waves. Since the speed of the waves is governed by Eq. (4.6), the relationship between the actual frequency of the waves

and the observed frequency in a moving reference frame is nonlinear and somewhat complicated. In order to understand how the frequency of the ocean waves is shifted, a moving reference frame will be defined. The movement of this frame will be simplified to represent an aircraft moving in a straight line at a constant speed. The lidar will be assumed to be pointed directly down so that the lidar measures the sea surface elevation at the same x-y location as the center of the moving reference frame. Aerial motions such as acceleration, attitude changes, or turning, will be ignored. In general, these simplifications have negligible effects when it comes to representing ALB since lidar data is typically taken with a plane moving in a straight line at a mostly constant velocity. Going forward, the movement of this reference frame will be defined using the vector $\vec{V}$.

With the motion of the lidar reference frame now defined, the lidar's position can be formulated as a function of time, $\vec{x} = \vec{V}$t. This gives us the ability to determine the ocean surface height measured by the lidar for any time t. To do this, Eq. (2.37) is rewritten.

$$h(t) = \sum_{\vec{k}} A(\vec{k}) cos((\omega - \vec{k} \cdot \vec{V})t + \phi) \tag{4.7}$$

From equation 4.7 it can be seen that there is no longer spatial dependence and what used to be spatial dependence manifests as a modified angular frequency. This new angular frequency is defined below in Eq. (4.8). The dot product between the wavenumber and the aircraft velocity is also shown as a product of magnitudes where α is the angle from the aircraft velocity vector to the wavenumber vector.

$$\omega' = \omega - \vec{k} \cdot \vec{V} = \omega + |\vec{k}||\vec{V}| cos(\alpha) \tag{4.8}$$

To be useful, ω' must be further reduced such that it is dependent solely on physical parameters and the wave's original frequencies. To do this, the dispersion relation will be employed.

$$\omega' = \omega\Big(1 - \frac{\omega|\vec{V}|cos(\alpha)}{g}\Big) \tag{4.9}$$

This equation governs how the frequency of the waves that comprise the ocean surface are

transformed when viewed from a moving reference. Although we now have an expression for how the frequency of these waves shifts, in order to understand how the frequency spectrum of the wind driven ocean waves translates into the frequency spectrum seen in the predicted lidar data, Eq. (4.9) must be applied to the theoretical ocean power spectrum.

4.3.2 Power Spectrum Transformation

As previously mentioned, several theoretical power spectral densities have been developed to predict the frequency properties of the ocean surface. These spectra are specifically designed for waves caused by wind, the main source of typical ocean waves. The purpose of this section is to show how to convert a theoretical frequency spectrum defined in ω and θ into the coordinates ω' and α as seen in E. (4.9). This will be done by looking at the energy content of a theoretical spectrum, S(ω,θ), as an integral. In order to properly convert between S(ω,θ) and S(ω',α), the energy in these integrals must be conserved. Once the ocean power spectral density has been converted to the moving lidar frame as S(ω',α), the frequency content of the lidar time series can be derived by removing α. This will be done by integrating S(ω',α) over all α to account for the contribution of waves from all directions.

$$\iint_A S(\omega,\theta)d\omega d\theta = \iint_B S(\omega',\alpha)d\omega' d\alpha \tag{4.10}$$

To convert between these two integrals, ω and θ must be defined as functions of ω' and α. An expression for the relation between ω and ω' already exists through equation 4.9. The difference between α and θ is fortunately much more simple: θ is the angle from the wind direction to the wave direction, and α is the angle from the aircraft velocity vector to the wave direction. The relationship between θ and α can then defined as seen in equation 4.11. In this equation, ψ is the angle from the wind to the aircraft velocity vector.

$$\alpha = \theta - \psi \tag{4.11}$$

A visualization of these different angles and coordinates is shown below in Fig. (4.9).

Figure 4.9: Example orientation of direction vectors and angles important to the moving reference transformation. The plane direction vector, wind direction vector, and a randomly orientated wave are shown.

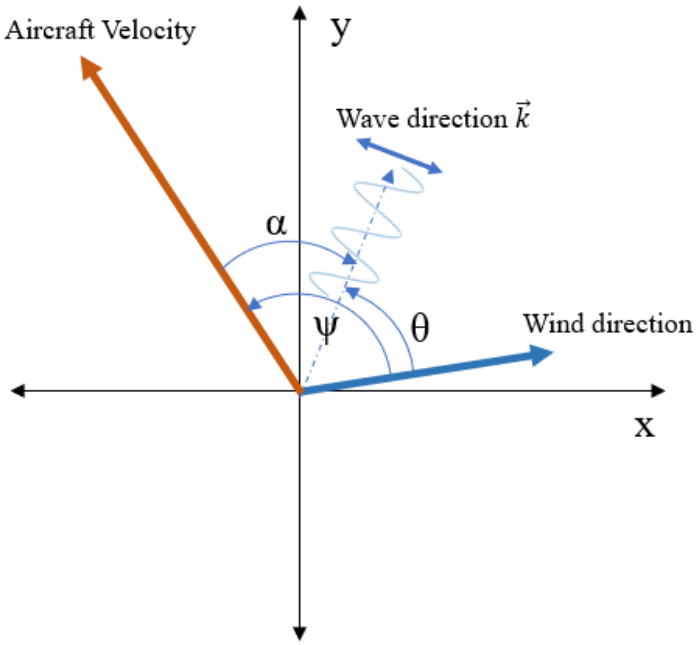

Before delving into the transformation of power spectra, it is necessary to give further thought to the dependence of ω' on ω and α. Although ω' should really be formulated in terms of θ for the conversion in Eq. (4.10), it is easier to visualize when described with α and the conversion between α and θ is trivial regardless. In this form, ω' can be charted in ω, α space. This space is similar to polar coordinates however the range of ω is restricted to $\omega \geq 0$. By doing this, some interesting effects become apparent. Firstly, it is clear from Eq. (4.9) that the relationship between ω and ω' is quadratic in nature. The shape and behavior of this quadratic is heavily dependent on α. For $\cos(\alpha) > 0$, the quadratic is inverted and has a local peak and two zeros. For $\cos(\alpha) < 0$, the quadratic is positive, only has a zero at $\omega = 0$, and has no local max or min in it's range. For $\cos(\alpha) = 0$, all quadratic behavior is lost and ω' is simply equal to ω. Another complication arises from the fact that ω' should always be greater than zero since all frequencies seen in the lidar time

series will be positive. This means that a negative should be added to Eq. (4.9) when ω' is less than zero in the region of $\cos(\alpha) > 0$. When converting $S(\omega,\theta)$ to $S(\omega',\alpha)$, all ω, α locations with energy must be accounted for. The quadratic nature of Eq. (4.9) makes it so every ω',α pair is mapped to several different ω, θ pairs. In other words, ocean waves with different frequencies can contribute to the same frequency when viewed from the moving aircraft reference. This means the right side of Eq. (4.10) must be broken into several integrals to be correct. A visualization of some of the interesting features of this transform in ω, α space are shown below.

Figure 4.10: Features of the ω to ω' transform in ω, α space. Four important regions, A1, A2, A3, and A4 are shown. Additionally, lines along which local maxima exist and zeros exist are shown.

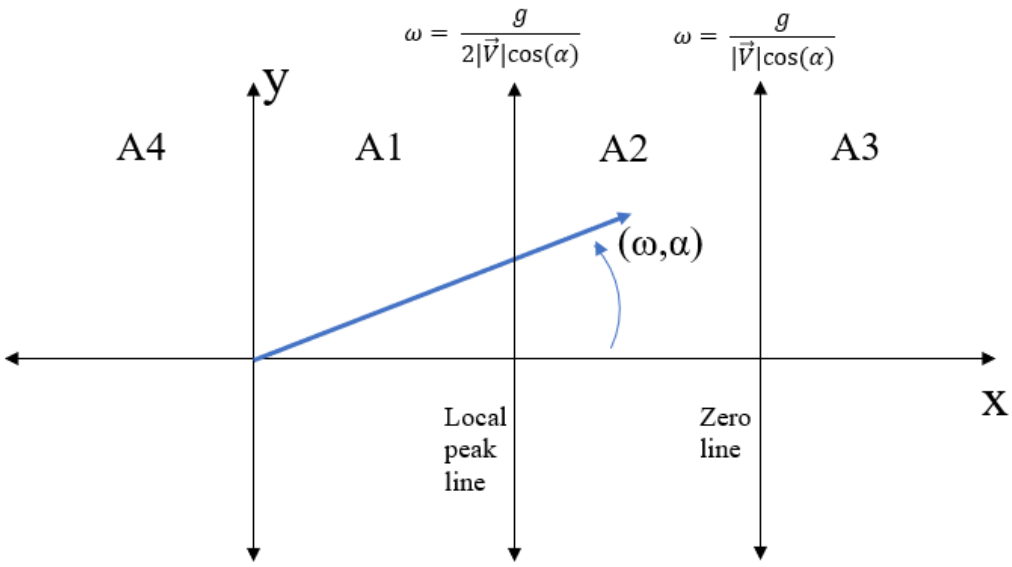

The four different regions (A1, A2, A3, A4) shown in this figure are important to consider when evaluating integrals for $S(\omega',\alpha)$. In each region, the transformation between ω and ω' has slightly different properties. These regions will be discussed in more depth later when it becomes time to remove the dependency of $S(\omega',\alpha)$ on α.

With a better understanding of the relationship between ω, θ, ω', and α coordinates, we can now go back to transforming the theoretical ocean power spectrum, $S(\omega,\theta)$. The relationship

between S(ω,θ) and S(ω',α) is given by the integrals in Eq. (4.10). To express S(ω',α) in terms of S(ω,θ), the differentials for each integral must be equated. To do this, a Jacobian must be used. Typically for this process, ω and θ must be written as functions of ω' and α. These expressions are much more complicated than what we have currently, which are ω' and α as functions of ω, θ. Writing ω as a function of ω' and α is actually one of the main reasons why the different regions A1-A4 are necessary. Although the treatment of these different regions is unavoidable, some of this problem can be simplified by evaluating the Jacobian using ω'(ω,θ), α(ω,θ).

$$\frac{\partial(\omega', \alpha)}{\partial(\omega, \theta)} = \begin{vmatrix} \frac{\partial\omega'}{\partial\omega} & \frac{\partial\omega'}{\partial\theta} \\ \\ \frac{\partial\alpha}{\partial\omega} & \frac{\partial\alpha}{\partial\theta} \end{vmatrix} \tag{4.12}$$

When evaluated, this becomes:

$$\frac{d\omega' d\alpha}{d\omega d\theta} = \begin{vmatrix} 1 - \frac{2\omega|\vec{V}|}{g} cos(\theta - \psi) & \frac{|\vec{V}|\omega^2}{g} sin(\theta - \psi) \\ \\ 0 & 1 \end{vmatrix} = 1 - \frac{2\omega|\vec{V}|}{g} cos(\theta - \psi) \tag{4.13}$$

The conversion between $d\omega' d\alpha$ and $d\omega d\theta$ is the last needed factor for converting between ω, θ, and ω', α coordinates. Eq. (4.10) can now be rewritten such that there is equivalency between S(ω,θ) and S(ω',α).

$$\iint\limits_A S(\omega, \theta) d\omega d\theta = \iint\limits_B S\big(\omega(\omega', \alpha), \theta(\omega', \alpha)\big) \left(\frac{g}{g - 2\omega(\omega', \alpha)|\vec{V}| cos(\alpha)} \right) d\omega' d\alpha \tag{4.14}$$

The integrand on the right hand side is S(ω',α) and therefore the conversion between S(ω,θ) and S(ω',α) is complete. However, for this equation to be useful, one must be able to determine ω based off ω' and α. This conversion is complicated due to the fact that ω is technically not a function of ω' and α (a single ω', α pair may map to multiple different values of ω). Additionally, S(ω',α) is not directly useful to our cause since there is still dependence on α. To model the

frequency spectra seen by the lidar, S(ω',α) must be integrated with respect to α. This analysis will be covered in the next section.

$$S(\omega', \alpha) = S\big(\omega(\omega', \alpha), \theta(\omega', \alpha)\big)\left(\frac{g}{g - 2\omega(\omega', \alpha)|\vec{V}|cos(\alpha)}\right) \tag{4.15}$$

4.3.3 Lidar Time Series Frequency Spectrum

So far, the theoretical ocean power spectral density has been converted into a representation correspondent to a moving reference frame. The end goal of this analysis is to determine what the spectral content of a lidar series should look like when ocean waves are measured from a moving aircraft. To do this, the directional power spectral density of the wind driven ocean waves must be reduced to a power spectral density solely dependent on ω. Since waves of all directions contribute to the oscillations seen in time, the non-directional power spectral density can be obtained from the directional form simply by integrating the directional form over all directions. This idea is shown below in equation 4.16.

$$P(\omega) = \int_0^{2\pi} S(\omega, \theta) d\theta \tag{4.16}$$

Given the analysis done up to this point in this paper, the theoretical frequency spectrum that should be observed by the lidar can be determined using Eq. (4.16) and Eq. (4.15). The integral will now be in terms of α however this change is insignificant since there is a 1:1 relationship between θ and α. Additionally, the bounds of [0,2π] are maintained for α.

$$P(\omega') = \int_0^{2\pi} S\big(\omega(\omega', \alpha), \theta(\omega', \alpha)\big)\left(\frac{g}{g - 2\omega(\omega', \alpha)|\vec{V}|cos(\alpha)}\right) d\alpha \tag{4.17}$$

In practice, evaluating Eq. (4.17) is somewhat tricky. This is where the importance of the previously discussed regions A1-A4 come into play. The definitions of these regions are given below.

$$A1: \quad 0 \leq \omega \leq \frac{g}{2|\vec{V}|cos(\alpha)}, \qquad cos(\alpha) > 0 \tag{4.18}$$

$$A2: \quad \frac{g}{2|\vec{V}|cos(\alpha)} < \omega \leq \frac{g}{|\vec{V}|cos(\alpha)}, \qquad cos(\alpha) > 0$$

$$A3: \quad \omega > \frac{g}{|\vec{V}|cos(\alpha)}, \qquad cos(\alpha) > 0$$

$$A4: \quad \omega > 0, \qquad cos(\alpha) < 0$$

The map relating ω, α to ω' is shown in figure 4.11 as a contour plot.

Figure 4.11: The ω to ω' transform in ω, α space. The features discussed in Fig. (4.10) can be seen.

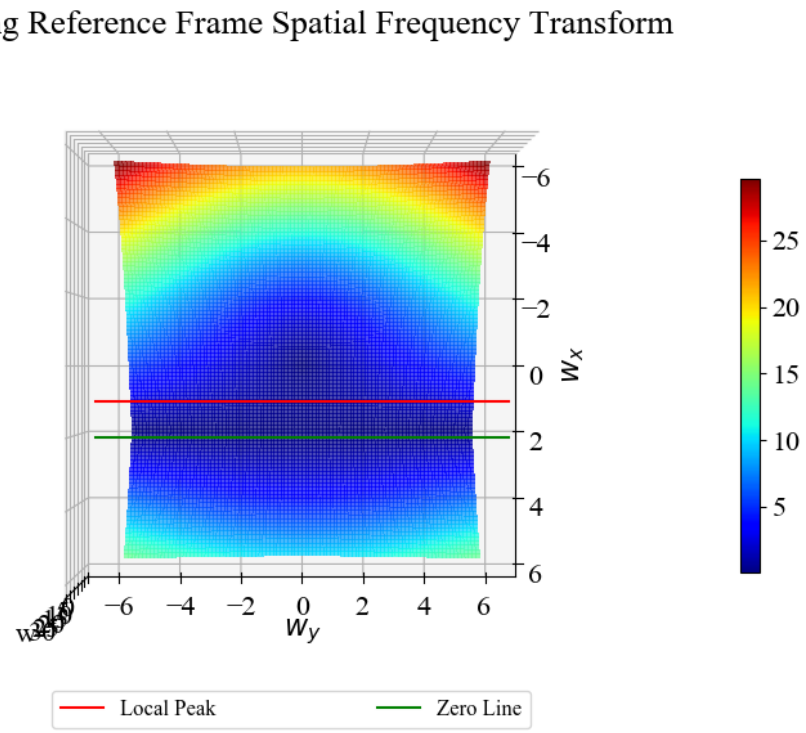

The parabolic growth expected from Eq. (4.9) can be seen clearly. In addition, the line of local maxima and the zero line can be seen along with their effects on the transform. It should be noted that this transform is for a slow moving object. For anything moving near aircraft speed, the zero line and the line of local maxima pass very close to the origin.

The integral in Eq. (4.17) must be reformulated as a sum of integrals over these regions. The total frequency seen from the lidar is then given according to Eq. (4.19), where each $P_i(\omega')$ is Eq. (4.17) evaluated over the region A_i.

$$P(\omega') = P_1(\omega') + P_2(\omega') + P_3(\omega') + P_4(\omega') \tag{4.19}$$

The first region, A1 is the portion of ω, α space on the right side (positive x in Cartesian coordinates) bound between the Cartesian y-axis and the line of local maxima. When discussing these different regions and their differences, it is often useful to use Cartesian coordinates in addition to ω,α coordinates. Although the integrals and the power spectra are expressed in ω, α space, these regions are somewhat related to Cartesian space. With this in mind, on the positive x side of this space, ω' takes the form of an inverted parabola. The peak of this parabola always occurs on this line for a given α. The height of this peak is dependent on α and takes the form of a hyperbola with respect to the Cartesian y value. As α nears $\pi/2$ or -$\pi/2$, the peak of the parabola which describes ω' goes towards infinity and the shape of the transform approaches the $\omega = \omega$'. Within region A1, the expression for $\omega(\omega',\alpha)$ can be obtained using the quadratic formula and Eq. (4.9). The result is shown below.

$$\omega_1(\omega', \alpha) = \frac{g - \sqrt{g^2 - 4\omega' g|\vec{V}|cos(\alpha)}}{2|\vec{V}|cos(\alpha)} \tag{4.20}$$

The region of α over which S(ω',α) is to be integrated for A1 is not always simply cos(α) > 0. This region will be defined as Ω going forward. The complicated nature of this region is due to the fact that for a large enough ω', there is not always a valid ω value in A1 for the full range of α. This is due to the line of local maxima. The minimum ω' value along this line occurs at $\alpha = 0$. If ω' is greater than this minimum, then there will be a range of α in A1 which cannot map to the input ω'. The value of ω' at which this starts to happen is $\omega' \geq g/(4|\vec{V}|)$. It should be noted that for any ω' value, there will always be some range of α in A1 which contribute. The region, Ω, over

which α should be integrated over for A1 is therefore given by the following equation.

$$\Omega_1 = \begin{cases} \alpha = \left[0, \frac{\pi}{2}\right) \bigcup \left(\frac{3\pi}{2}, 2\pi\right) & \text{for } \omega' \leq \frac{g}{4|\vec{V}|} \\ \\ \alpha = \left[cos^{-1}\left(\frac{g}{4|\vec{V}|\omega'}\right), \frac{\pi}{2}\right) \bigcup \left(\frac{3\pi}{2}, 2\pi - cos^{-1}\left(\frac{g}{4|\vec{V}|\omega'}\right)\right] & \text{for } \omega' > \frac{g}{4|\vec{V}|} \end{cases} \tag{4.21}$$

It may be tempting to ignore the unions in Eq. (4.21) and use symmetry to simplify the integration. Unfortunately this cannot be done. Although symmetry does exist on either side of the x-axis in the ω, ω' transform, it is not necessarily preserved in terms of the theoretical power spectrum. Due to the offset between θ and α, the theoretical ocean power spectrum shown in Fig. (2.2) may be orientated in any arbitrary direction, and the energy on either side of A1 may not be equal.

With the region over which to integrate defined in Eq. (4.21), the function $\omega(\omega',\alpha)$ defined in Eq. (4.20), and the integrand defined in Eq. (4.15), the contribution to the lidar time series frequency spectrum from A1 can now be determined. It is worth noting that the function $\theta(\omega',\alpha)$ can be derived from Eq. (4.11) and is simply $\theta(\omega',\alpha) = \alpha + \psi$.

$$P_1(\omega') = \int_{\Omega_1} S\big(\omega_1(\omega',\alpha), \theta(\omega',\alpha)\big)\left(\frac{g}{g - 2\omega_1(\omega',\alpha)|\vec{V}|cos(\alpha)}\right)d\alpha \tag{4.22}$$

The second region, A2 exhibits many of the same properties as region A1. This region, like A1, is on the right side of ω, α space, and is bound between the line of local maxima and the zero line. The zero line is parallel to the line of local maxima but located twice as far from the y-axis. At any point along this line, the value of ω' is zero.

The main difference between regions A1 and A2 is in the equation for $\omega(\omega',\alpha)$. Once again, $\omega(\omega',\alpha)$ for region A2 is determined using Eq. (4.9) and the quadratic formula. However, this time the $\pm$ in the quadratic formula is reversed. This gives the other side of the parabola in Eq. (4.9). The same issues experienced when determining Ω for A1 also exist in this region. Fortunately, the

effects are identical and the range Ω from A1 can be reused.

$$\omega_2(\omega', \alpha) = \frac{g + \sqrt{g^2 - 4\omega' g|\vec{V}|cos(\alpha)}}{2|\vec{V}|cos(\alpha)} \tag{4.23}$$

$$\Omega_2 = \Omega_1 \tag{4.24}$$

The only other difference between A1 and A2 has to do with the sign of the integrand. Earlier, a Jacobian was calculated to reference dωdθ to dω'dα. This Jacobian shows how changes in ω effect ω'. For region A2, changes positive changes in ω result in a decrease in ω'. Therefore, when the power is integrated over this region with respect to ω, the direction of integration with respect to ω' is reversed. To account for this, a negative sign should be added to the integrand for A2. Without this negative, the integrated power in this region will be negative which is physically impossible. The resultant expression for the frequency contributions from A2 is therefore given by Eq. (4.31).

$$P_2(\omega') = \int_{\Omega_2} S\big(\omega_2(\omega', \alpha), \theta(\omega', \alpha)\big)\left(\frac{g}{2\omega_2(\omega', \alpha)|\vec{V}|cos(\alpha) - g}\right)d\alpha \tag{4.25}$$

The next region, A3, comprises the remainder of the right side of ω, α space. This region corresponds to the section of the parabola in Eq. (4.9) that is below zero. Since we are only interested in positive frequencies and any negative ω' values should reappear in the lidar frequency spectrum as positive, Eq. (4.9) should be multiplied by a negative for this region. This changes the expression for ω(ω',α) obtained with the quadratic formula and flips the sign of the Jacobian. Fortunately, the complications that exist when defining Ω for regions A1 and A2 do not apply to A3. For any value of ω', α is valid for any cos(α) > 0. The contribution from A3 can then be found using the equations below.

$$\omega_3(\omega', \alpha) = \frac{g + \sqrt{g^2 + 4\omega' g|\vec{V}|cos(\alpha)}}{2|\vec{V}|cos(\alpha)} \tag{4.26}$$

$$\Omega_3 = \left[0, \frac{\pi}{2}\right) \bigcup \left(\frac{3\pi}{2}, 2\pi\right) \tag{4.27}$$

$$P_3(\omega') = \int_{\Omega_3} S\big(\omega_3(\omega', \alpha), \theta(\omega', \alpha)\big) \left(\frac{g}{2\omega_3(\omega', \alpha)|\vec{V}|cos(\alpha) - g}\right) d\alpha \tag{4.28}$$

The final region, A4 consists of the entire left side of ω,α space. In this region cos(α) ¡ 0. Since cos(α) is less than zero in this region, the parabola in Eq. (4.9) flips. The properties of this region are identical to those of A1 besides the definition of Ω. The main reason for separating A1 and A4 is due to the fact that ω(ω',α) is not continuous for these regions across $\alpha = \pm\pi/2$. The equations needed for evaluating A4 are given below.

$$\omega_4(\omega', \alpha) = \frac{g - \sqrt{g^2 - 4\omega' g|\vec{V}|cos(\alpha)}}{2|\vec{V}|cos(\alpha)} \tag{4.29}$$

$$\Omega_4 = \left(\frac{\pi}{2}, \frac{3\pi}{2}\right) \tag{4.30}$$

$$P_4(\omega') = \int_{\Omega_4} S\big(\omega_4(\omega', \alpha), \theta(\omega', \alpha)\big) \left(\frac{g}{g - 2\omega_4(\omega', \alpha)|\vec{V}|cos(\alpha)}\right) d\alpha \tag{4.31}$$

With P(ω') now defined for each region, the expected frequency spectrum for the lidar time series can be calculated. Due to the complicated nature of each of these integrals and the complicated formula for the JONSWAP theoretical power spectral density, these integrals were evaluated using a numerical integrator in python. For an input wind vector and aircraft velocity vector, this program calculates the expected lidar power spectrum for an array of ω'. For each ω', the program numerically evaluates the integrals for each region A, using the JONSWAP spectrum function to determine the integrand.

4.3.4 Lidar Frequency Content Results

Before delving into the results of the model, it is useful to think about some of the quantitative behavior one would expect to see in the lidar frequency spectrum. For one, if the aircraft velocity

vector is set to zero, one would expect to recover the original JONSWAP spectrum. Secondly, for a fast travelling aircraft, it is expected that the frequency content in the lidar time series would be spread out in comparison to the original JONSWAP power spectral density. This is because the quadratic behavior in Eq. (4.9) will dominate and small changes in ω will result in large changes in ω'. When looking at the map of ω' in ω, α space for this situation, the line of local maxima and the line of zero will be near the origin and the fast growing behavior seen in regions A4 and A3 will dominate. One last trait that one would expect the lidar frequency spectrum to exhibit, is a large DC component when the line of zero is near the original JONSWAP peak. Related to this is the expected behavior for when the wind vector and aircraft velocity vector are perpendicular. In this case, the line of zero is guaranteed to pass near the peak of the theoretical power spectral density. This results in a significant DC component for this situation as well.

To start, the ω' transform in ω, α space is shown for an aircraft travelling at a typical speed (200 m/s).

Figure 4.12: The ω to ω' transform in ω, α space for a fast moving reference frame.

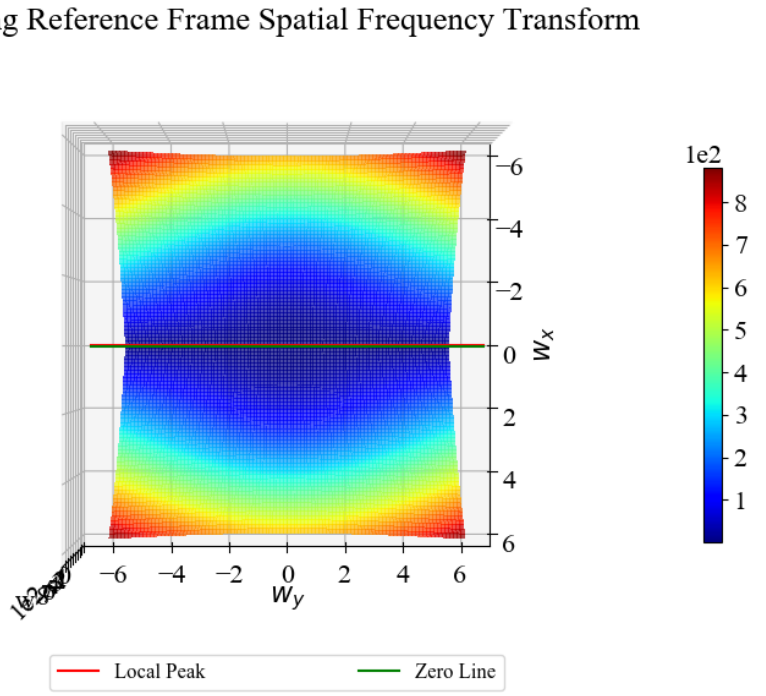

It can be seen from this figure how the observed frequency of the waves grows extremely quickly for most regions of ω, α space. The one exception to this is for waves travelling perpendicular to the aircraft velocity. These waves (depicted along the y-axis) do not change in frequency. The local peak line and the local zero line have also been affected by the increased aircraft speed. They are now nearly on top of each other and both of them pass very close to the origin. The effect of this on the modeled spectrum is heavily dependent on the angle between the aircraft movement and the wind. For an aircraft travelling parallel to the wind, the majority of the ocean spectral power (Fig. (2.2)), will be concentrated outside the influence of these two lines. In this region, the transform between ω' and ω is mainly paraboloidal. The behavior seen in this region is more straightforward than the region near the lines. The shape of the predicted spectrum for this case therefore is more smooth. On the other hand, when spectral power is located in regions A1 and A2, the shape of the transformed spectrum is expected to be more complex.

The first theoretical spectrum generated using this model was for a stationary aircraft frame. In theory, the original JONSWAP spectrum should be recovered. The resultant spectrum generated from this test is shown below in Fig. (4.13).

Figure 4.13: The expected frequency spectrum for the lidar time series for a still frame of reference. Also shown is the original JONSWAP spectrum.

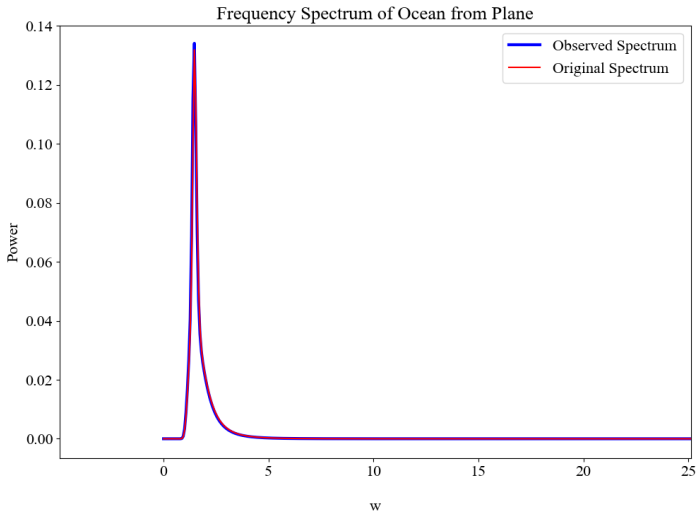

As expected, this spectrum is nearly identical to the original JONSWAP spectrum. This is an encouraging sign for confirming the validity of this model. This result is also a positive sign for ensuring that the implementation of the model is correct. For this case, the numerical integration of the directional power spectral density clearly provides accurate results.

For an aircraft moving at a typical flight speed, in the same direction as the wind, the following spectrum was generated (Fig. (4.14)).

Figure 4.14: The expected frequency spectrum for the lidar time series for a reference frame moving at typical flight speeds. Also shown is the original JONSWAP spectrum.

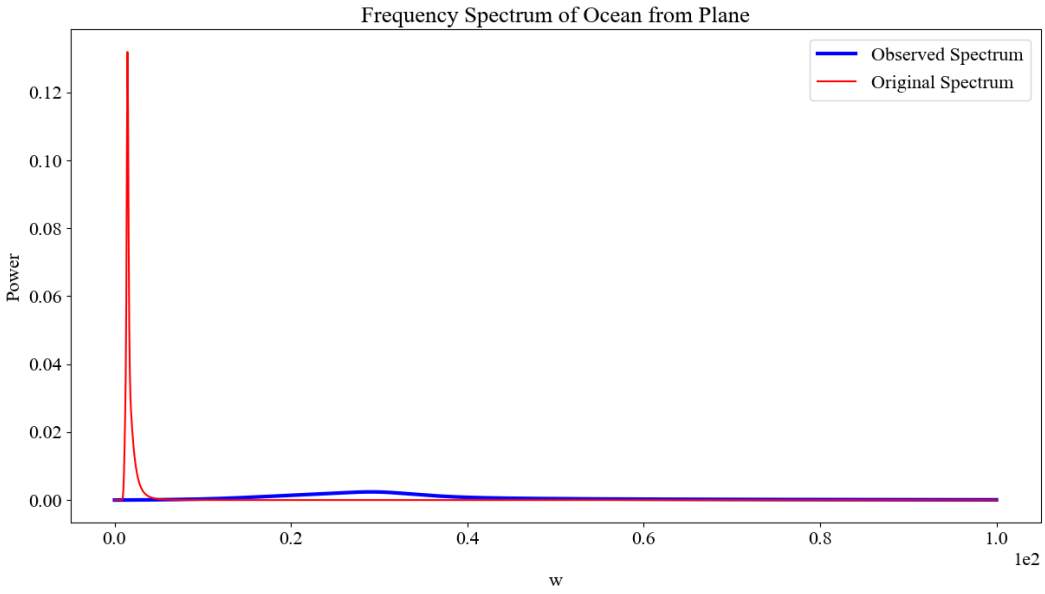

This simulated spectrum generally exhibits the behavior that can be expected for this case. The energy in the predicted spectrum is much more spread out. Additionally, the peak of the transformed spectrum is at a much larger frequency. This makes physical sense as one would expect ocean waves to be quickly traversed at an aircraft's speed. Fig. (4.14) indicates that, for typical ALB scenarios, the lidar time series should contain a large range of oscillatory behavior.

The final plot that will be shown is the expected spectrum for perpendicular aircraft velocity and wind vectors. The speed of the aircraft is reduced (possibly closer towards a typical helicopter speed) so that the expected DC behavior can be better seen.

Figure 4.15: The expected frequency spectrum for the lidar time series for a reference frame moving perpendicular to the wind direction.

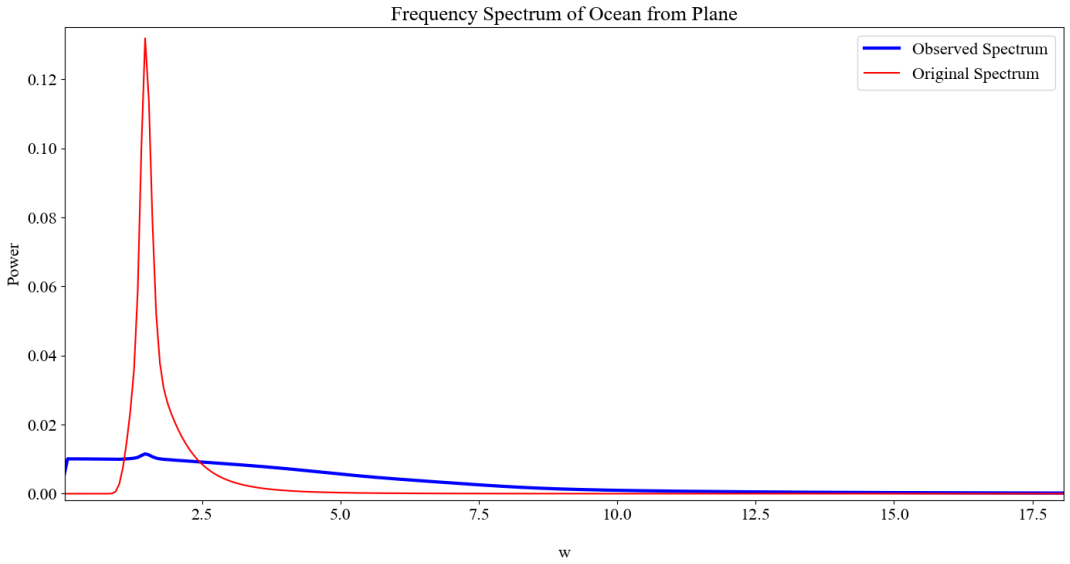

There are several notable features present in this plot. As expected, a large amount of the energy in this spectrum is located around $\omega = 0$. The speed of the aircraft still causes a decent amount of spread in the signal however the spread no longer reaches out to as high of frequencies. An interesting feature of this spectrum is a slight bump at the JONSWAP spectrum peak. This is due to the fact that waves travelling perpendicular to the aircraft velocity do not shift in frequency (this can be seen from Eq. (4.9)). The shape of this spectrum could be described as a combination of the original spectrum and a spread of energy starting at $\omega = 0$.

A final encouraging result from this model is the fact that the energy of the transformed spectrum seems to be conserved. For all of the situations simulated above, the integrated energy in the theoretical JONSWAP spectrum closely matches that from the simulated lidar frequency spectrum. The comparison of energy between these two spectra is nearly always less than 5 percent error. With increased frequency resolution and range, the comparison of energy further improves to under 1 percent error. This comes at the cost of computational time.

4.3.5 Comparison to ARISTO Data

It is easy to forget, after all that math, that the original goal of this analysis was to validate the ocean model by comparison of frequency spectra. To do this, three different frequency distributions will be looked at. The first is the theoretical spectrum derived in the previous sections.

The second is obtained from the ocean lidar model by changing the position of the lidar source to simulate aircraft motion. This spectrum is obtained using a Fast Fourier Transform since the sampling rate can be controlled. The simulated ocean surface is created based off the wind speed obtained from the variance of the real lidar data. The plane speed can be approximated by calculating the change in position of the aircraft over the time frame shown in Fig. (4.5). Fortunately, the aircraft motion is linear for this period of time. For more complicated aircraft maneuvers, estimation of the predicted frequency content of the lidar time series is significantly more difficult. The wind direction can be obtained from sensors on board the aircraft. The wind speed obtained from these sensors is less useful, unfortunately, due to the fact that they record wind speed at the aircraft altitude. It is assumed that there is little variation in the direction of the wind between the aircraft altitude and the ocean surface. Furthermore, it can be seen after comparing frequency spectra that the wind speed obtained from the aircraft sensors yields a correctly shaped lidar frequency distribution.

The final spectrum used for comparison is the frequency spectrum of the lidar time series. Calculation of this spectrum is less trivial due to the irregular sampling inherent with photon counting. A Fast Fourier Transform algorithm cannot be used. Furthermore, the data gaps make interpolation difficult and susceptible to large, spurious, frequency peaks. Although not a perfect solution, a Lomb-Scargle algorithm is used to obtain the frequency distribution for the real data. This method of power spectral density calculation is designed for irregular sampling. Lomb-Scargle is commonly used in the field of astrophysics and combines ideas related to Fourier methods, Bayesian probability theory, and least squares methods. Nonetheless, it is still susceptible to errors caused by highly irregular sampling. For example, the spectral density of a signal with regularly

spaced data gaps (like Fig. (4.4)) will have a false peak at the frequency with which those gaps appear. The source of this false peak is related to the window used on the data. Spurious effects related to windowing are lessened for more regular data and for equi-spaced data, the Lomb-Scargle algorithm perfectly mirrors the results of a FFT.

The three spectral densities to be compared are shown below. The Lomb-Scargle result has been normalized for comparison with the other spectra.

Figure 4.16: A comparison of lidar frequency spectra for wave detection from a moving aircraft. The red, "simulated" spectrum corresponds to that obtained with the lidar-ocean model. The blue, "theoretical" spectrum corresponds to the moving reference analysis in the previous sections. The black, "real" spectrum correspond to the goereferenced INPHAMIS 1 data.

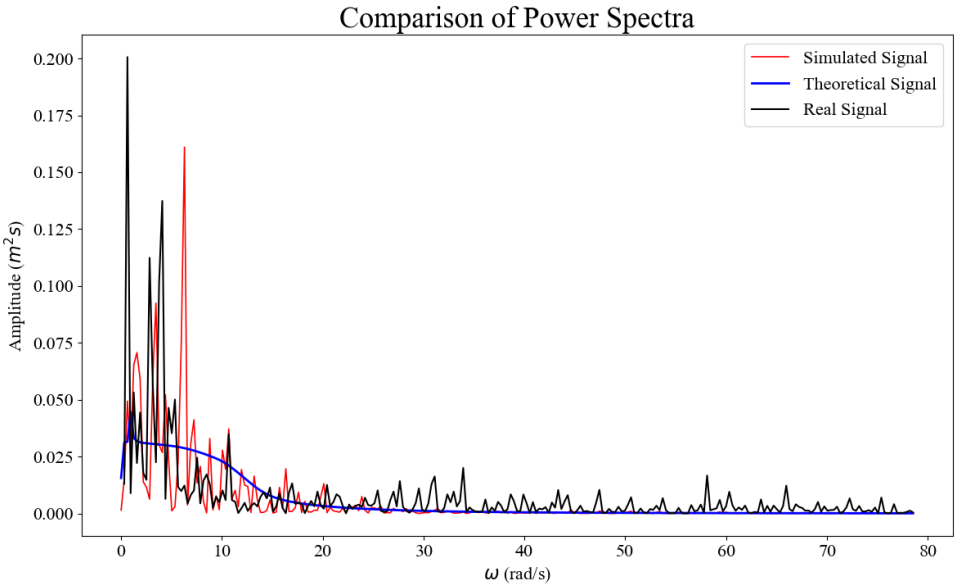

Both the ocean-lidar model times series and the time series obtained from INPHAMIS 1 data exhibit extremely spiky behavior. This is to be expected, due to the random nature of the wave amplitudes discussed in section 2.2.4. The theoretical spectral density is simply a representation of the expectation of the spectral density for a given frequency. Additionally, the ocean surface used to generate the simulated signal was created according to a summation of discrete frequencies.

When the spread seen in Fig. 4.12 occurs, these discrete frequencies become separated and appear as deltas when manifested in the signal transform. The energy seen at higher frequencies in the spectrum of the real data is a consequence of the Lomb-Scargle algorithm[48]. Even though the lidar time series used for this analysis lacks data gaps for the most part, the sampling is still highly irregular and therefore the window is noisy. The main discrepancy that can be seen between the frequency distribution of the real data and that of the models is at low frequencies. The young, quickly changing sea state seen in Figs. (4.7 and 4.8) is a possible explanation for this. The energy in waves travelling in a different direction than the wind is related to interactions between waves in a mature sea. In a young sea, waves that travel parallel to the wind are in the process of being generated and there has not yet been enough time for inter-wave interactions to distribute energy into different directions. Since the plane is travelling orthogonal to the wind, the line of zero passes close to the peak of the directional spectrum. If more energy is concentrated around this peak rather than spread into different directions, low frequencies will be magnified. In general, these spectra all exhibit very similar shapes and follow the behavior predicted by the analysis in the previous sections. This indicates that the wind vector was likely orthogonal to the plane motion. This result means it may be possible to extract wind direction from the frequency content of fixed beam lidar ocean wave data. The comparison of spectra also implies that the spectral density used in the ocean wave model is realistic. Ocean surface behavior is complicated and although the directional spectral distribution used in this paper may not be perfect for all circumstances, it does produce a verifiably realistic ocean surface.

Chapter 5

Future Work

The work presented here is a good step towards building a comprehensive understanding of how ocean conditions affect airborne lidar bathymetry. With the combination of ocean modelling and lidar modelling described in this thesis, it has been shown that a wavy ocean surface can significantly add to the uncertainty in ALB measurements. Futhermore, the ocean surface effects can clearly be seen in the distribution of lidar measurements taken over a wavy ocean surface. This allows for estimation of the surface variance and extraction of physical information such as significant wave height and wind speed. An ALB system's ability to do this is promising as demonstrated with the INPHAMIS 1 data from the ARISTO campaign. There are several promising ways in which the work presented here can be furthered. These are: expanded use of the lidar-ocean model, further study of the spectral content of a lidar ocean wave time series, and further analysis of real INPHAMIS 1 data.

5.1 Continued Use of Lidar-Ocean Model

The first way in which this work could be extended is with the lidar-ocean model. This model is capable of handling many more conditions than those investigated in this thesis. Many different lidar parameters or ocean environment conditions that were kept fixed at a nominal value for the simulations presented here could be varied. The interaction of a wavy ocean surface with a lidar is complicated and it is likely that there are many other significant effects besides wind speed and off-nadir angle. For example, the representation of the ocean floor is extremely simplified for

this analysis. The effects of a rough ocean floor or an ocean floor with some input shape would be of interest. The polarization properties of the ocean floor should also be examined with more detail. The ocean surface and floor combine to determine the polarization state of the light received from the ocean floor. If the ocean floor is partially polarizing, as is typical in reality, the ocean surface may exhibit new effects not captured in the simulations described in this paper. Water column effects such as multiple scattering have also been shown to have a significant effect on beam spread and polarization, especially in deeper waters[8][49][15]. The ocean surface could also be modeled with higher fidelity. Given more computational resources and time, extremely high resolution ocean surfaces could be generated. This would improve the accuracy of simulations at high wind speeds. Additionally, small scale wave behavior will be better represented. This may be necessary depending on the lidar to be modelled. For a lidar with a small beam spot on the ocean surface, the correlation length of small waves will be similar in size to the lidar beam. In this case, capillary waves may refract or focus the entire beam as opposed to spreading it[21][49].

On the lidar side of the simulation, parameters such as beam divergence and polarization can be further studied. By varying lidar parameters, the uncertainties discussed in chapter 3 may be improved or worsened. This could lead to a lidar design analysis where the effect of ocean waves could be minimized.

5.2 Spectral Analysis

The spectral analysis for a lidar ocean wave time series obtained from a moving platform is intriguing however more work must be done to fully validate this analysis and determine how it can be used. This theoretical spectral distribution is compared to actual ocean wave lidar data in this thesis to show how the directional JONSWAP spectral density used in forming the ocean surface is appropriate. Additionally, this shows that the oscillations seen in the INPHAMIS 1 data are due to ocean waves. More lidar ocean wave data at different aircraft speeds, wind speeds, and directions should be obtained to better characterize the validity of the spectral analysis presented in section 4.3.

The spectral analysis presented in section 4.3 may also find use for purposes besides model validation. One hope for this analysis would be to create a method for determining a predicted ocean power spectral density given lidar wave data. Another possible use could lie in comparing the frequency spectra of predicted lidar data with that of real ALB data to detect unexpected behavior. This may mean detecting unexpected surface wave structure caused by effects other than wind. This comparison may also yield information about how the actual ocean power spectrum differs from the theoretical ocean power spectral density model for the given wind conditions. At last, this comparison may allow for detection and removal of erroneous range effects in the ALB process. For example, if the lidar is mounted to a plane which is experiencing oscillatory motion, those frequencies may reappear in the lidar time series and cause spurious ocean surface results.

5.3 Real ALB Data

At last, the work presented in this thesis can continue to find use as more ALB data is obtained for the INPHAMIS 1 system. As the instrument is improved and future missions are conducted, this research can be used to characterize the uncertainty in the ALB measurements and to provide a guideline for how ocean wave parameters can be extracted. Additionally, using ALB data from future missions, it may be possible to validate the distributions predicted in chapter 3.

The correction of ALB errors due to the ocean surface is also possible to some extent[50]. This can be done by fitting a surface to ALB point cloud and then calculating the surface slope at each lidar point. This can lead to full reconstruction of the ocean surface. This reconstructed surface can be entered into the lidar-ocean model and lidar measurements that directly mirror the conditions present for real data can be simulated. This could lead to a greatly improved surface finding algorithm. It may also allow for improved measurement uncertainties and resolution, resulting in a general improvement in the quality of the ALB data.

Bibliography

[1] G. C. Guenther, M. W. Brooks, and P. E. LaRocque, "New capabilities of the shoals airborne lidar bathymeter," Remote Sensing of Environment, vol. 73, no. 2, pp. 247–255, 2000.

[2] C. A. Hostetler, M. J. Behrenfeld, Y. Hu, J. W. Hair, and J. A. Schulien, "Spaceborne Lidar in the Study of Marine Systems," Annual Review of Marine Science, vol. 10, no. 1, pp. 121–147, 2018.

[3] P. Westfeld, H.-G. Maas, K. Richter, and R. Weiß, "Analysis and correction of ocean wave pattern induced systematic coordinate errors in airborne lidar bathymetry," ISPRS Journal of Photogrammetry and Remote Sensing, no. 128, pp. 314–325, 2017.

[4] E. National Academies of Sciences, Medicine, et al., "Thriving on our changing planet: A decadal strategy for earth observation from space," Washington, DC: The National Academies Press., https://doi. org, vol. 10, p. 24938, 2018.

[5] A. G. Cunningham, W. Lillycrop, G. C. Guenther, and M. W. Brooks, "Shallow water laser bathymetry: accomplishments and applications," tech. rep., US Army Corps of Engineers Mobile United States, 2016.

[6] G. C. Guenther, A. G. Cunningham, P. E. LaRocque, and D. J. Reid, "Meeting the accuracy challenge in airborne bathymetry," tech. rep., NATIONAL OCEANIC ATMOSPHERIC ADMINISTRATION/NESDIS SILVER SPRING MD, 2000.

[7] D. Enabnit, L. Goodman, G. Young, and W. Shaughnessy, "The cost effectiveness of airborne laser hydrography," 1978.

[8] G. C. Guenther, "Airborne lidar bathymetry," Digital elevation model technologies and applications: the DEM users manual, vol. 2, pp. 253–320, 2007.

[9] G. C. Guenther, "Wind and nadir angle effects on airborne lidar water" surface" returns," in Ocean Optics VIII, vol. 637, pp. 277–287, International Society for Optics and Photonics, 1986.

[10] J. L. Irish and W. J. Lillycrop, "Scanning laser mapping of the coastal zone: the shoals system," ISPRS Journal of Photogrammetry and Remote Sensing, vol. 54, no. 2-3, pp. 123–129, 1999.

[11] V. Ramnath, P. Friess, H. Duong, V. Feygels, and Y. Kopilevich, "Total propagated uncertainty for coastal zone mapping and imaging lidar (czmil)," in Laser Radar Technology and Applications XXIII, vol. 10636, p. 106360N, International Society for Optics and Photonics, 2018.

[12] N. G. D. Center et al., "Bathymetry of lake ontario poster," 2006.

[13] J. P. Thayer, S. Mitchell, and M. Hayman, "Remote measurement of shallow depths in semi-transparent media," Oct. 25 2016. US Patent 9,476,980.

[14] S. E. Mitchell and J. P. Thayer, "Ranging through shallow semitransparent media with polarization lidar," Journal of Atmospheric and Oceanic Technology, vol. 31, no. 3, pp. 681–697, 2014.

[15] G. W. Kattawar, "Genesis and evolution of polarization of light in the ocean [invited].," Applied optics, vol. 52, pp. 940–8, 2013.

[16] B. M. Tsai and C. S. Gardner, "Remote sensing of sea state using laser altimeters," Applied Optics, vol. 21, no. 21, pp. 3932–3940, 1982.

[17] C. Mobley, E. Boss, and C. Roesler, "Ocean optics web book," 2010.

[18] Y. I. Kopilevich and A. G. Surkov, "Mathematical modeling of the input signals of oceanological lidars," Journal of Optical Technology, vol. 75, no. 5, p. 321, 2008.

[19] M. Birkebak, F. Eren, S. Peeri, and N. Weston, "The effect of surface waves on airborne lidar bathymetry (alb) measurement uncertainties," Remote Sensing, vol. 10, no. 3, p. 453, 2018.

[20] J. W. McLean, "Modeling of ocean wave effects for LIDAR remote sensing," SPIE Vol. 1302, 1991.

[21] J. W. McLean and J. D. Freeman, "Effects of ocean waves on airborne lidar imaging," Applied optics, vol. 35, no. 18, pp. 3261–3269, 1996.

[22] N. Forfinski and C. Parrish, "ICESat-2 bathymetry: an empirical feasibility assessment using MABEL," vol. 999904, no. October 2016, p. 999904, 2016.

[23] N. Foster and R. Fedkiw, "Practical animation of liquids," in Proceedings of the 28th annual conference on Computer graphics and interactive techniques, pp. 23–30, ACM, 2001.

[24] S. Premžoe, T. Tasdizen, J. Bigler, A. Lefohn, and R. T. Whitaker, "Particle-based simulation of fluids," in Computer Graphics Forum, vol. 22, pp. 401–410, Wiley Online Library, 2003.

[25] R. Winchenbach, H. Hochstetter, and A. Kolb, "Constrained neighbor lists for sph-based fluid simulations.," in Symposium on Computer Animation, pp. 49–56, 2016.

[26] J. Tessendorf et al., "Simulating ocean water," Simulating nature: realistic and interactive techniques. SIGGRAPH, vol. 1, no. 2, p. 5, 2001.

[27] M. Hayman and J. P. Thayer, "General description of polarization in lidar using Stokes vectors and polar decomposition of Mueller matrices.," Journal of the Optical Society of America. A, Optics, image science, and vision, vol. 29, no. 4, pp. 400–9, 2012.

[28] C. R. Vaughn, J. L. Bufton, W. B. Krabill, and D. Rabine, "Georeferencing of airborne laser altimeter measurements," 1995.

[29] B. Kinsman, Wind waves: their generation and propagation on the ocean surface. Courier Corporation, 1984.

[30] K. Hasselmann, T. Barnett, E. Bouws, H. Carlson, D. Cartwright, K. Enke, J. Ewing, H. Gienapp, D. Hasselmann, P. Kruseman, et al., "Measurements of wind-wave growth and swell decay during the joint north sea wave project (jonswap)," Ergänzungsheft 8-12, 1973.

[31] Q. Guo and Z. Xu, "Simulation of deep-water waves based on jonswap spectrum and realization by matlab," in Geoinformatics, 2011 19th International Conference on, pp. 1–4, IEEE, 2011.

[32] W. J. Plant, "The ocean wave height variance spectrum: Wavenumber peak versus frequency peak," Journal of Physical Oceanography, vol. 39, no. 9, pp. 2382–2383, 2009.

[33] C. Cox and W. Munk, "Measurement of the roughness of the sea surface from photographs of the suns glitter," Josa, vol. 44, no. 11, pp. 838–850, 1954.

[34] Y. Liu, M.-Y. Su, X.-H. Yan, and W. T. Liu, "The mean-square slope of ocean surface waves and its effects on radar backscatter," Journal of atmospheric and oceanic technology, vol. 17, no. 8, pp. 1092–1105, 2000.

[35] Y. Liu, X. Yan, W. Liu, and P. Hwang, "The probability density function of ocean surface slopes and its effects on radar backscatter," Journal of physical oceanography, vol. 27, no. 5, pp. 782–797, 1997.

[36] J. Battjes, T. Zitman, and L. Holthuusen, "A reanalysis of the spectra observed in jonswap," Journal of physical oceanography, vol. 17, no. 8, pp. 1288–1295, 1987.

[37] O. Svelto and D. C. Hanna, Principles of lasers, vol. 4. Springer, 1998.

[38] R. Barton-Grimley and D. Beatty, "Personal correspondence."

[39] G. W. Kattawar and C. N. Adams, "Stokes vector calculations of the submarine light field in an atmosphere-ocean with scattering according to a Rayleigh phase matrix: Effect of interface refractive index on radiance and polarization," Limnology and Oceanography, vol. 34, no. 8, pp. 1453–1472, 1989.

[40] C. D. Mobley, Light and water: radiative transfer in natural waters. Academic press, 1994.

[41] M. Mishchenko and J. Hovenier, "Depolarization of light backscattered by randomly oriented nonspherical particles," Optics Letters, vol. 20, no. 12, pp. 1356–1358, 1995.

[42] J. A. Gubner, Probability and random processes for electrical and computer engineers. Cambridge University Press, 2006.

[43] P. H. Zipfel, Modeling and simulation of aerospace vehicle dynamics. American Institute of Aeronautics and Astronautics, 2007.

[44] P. R. Wolf, B. A. Dewitt, and B. E. Wilkinson, Elements of Photogrammetry: with applications in GIS, vol. 3. McGraw-Hill New York, 2000.

[45] Duacs/AVISO, "A new version of ssalto/duacs products available in april 2014, version 1.1, cnes," 2014.

[46] R. A. Barton-Grimley, R. A. Stillwell, and J. P. Thayer, "High resolution photon time-tagging lidar for atmospheric point cloud generation," Optics express, vol. 26, no. 20, pp. 26030–26044, 2018.

[47] J. L. Irish, J. M. Wozencraft, and A. G. Cunningham, "Lidar sensor for measuring directional-spectral characteristics of water waves," tech. rep., CORP OF ENGINEERS MOBILE AL JOINT AIRBORNE LIDAR BATHYMETRY TECHNICAL CENTER , 2000.

[48] J. T. VanderPlas, "Understanding the lomb–scargle periodogram," The Astrophysical Journal Supplement Series, vol. 236, no. 1, p. 16, 2018.

[49] J. H. Churnside, "Polarization effects on oceanographic lidar," vol. 16, no. 2, pp. 1196–1207, 2008.

[50] F. Yang, D. Su, Y. Ma, C. Feng, A. Yang, and M. Wang, "Refraction Correction of Airborne LiDAR Bathymetry Based on Sea Surface Profile and Ray Tracing," IEEE Transactions on Geoscience and Remote Sensing, pp. 1–9, 2017.